SEARCH FOR UNIVERSAL EXTRA DIMENSIONS IN THE TWO PHOTON
AND MISSING TRANSVERSE ENERGY FINAL STATE WITH THE
ATLAS DETECTOR

by

Baharak Fatholahzadeh

A thesis submitted in conformity with the requirements
for the degree of Doctor of Philosophy
Graduate Department of Physics
University of Toronto

Abstract

Search For Universal Extra Dimensions in the Two Photon and Missing Transverse
Energy Final State With The ATLAS Detector

Baharak Fatholahzadeh

Doctor of Philosophy

Graduate Department of Physics

University of Toronto

2012

A search for diphoton events with large missing transverse energy is conducted using
3.1 pb^{-1} of integrated luminosity of proton-proton collisions at center of mass energy
$\sqrt{s} = 7$ TeV. The data were collected with the ATLAS detector at the CERN Large
Hadron Collider during the period from March 30, 2010 until August 30, 2010. No
excess of such events is observed above the Standard Model background prediction. This
result is interpreted in the context of a gravity mediated One Universal Extra Dimension
model with $\Lambda R = 20$, $N = 6$ and $M_D = 5$ TeV, where Λ is the cutoff scale, N is the
number of large extra dimensions and M_D is the Planck scale in the higher dimensional
theory. The compactification radius of the Universal Extra Dimension, R, is excluded for
values of $1/R < 728$ GeV at 95% CL, providing the most stringent limit on this model
at the time of publication.

Contents

List of Tables

List of Figures

Chapter 1

Foreword

My work with ATLAS began in the Summer of 2007. At this time the LHC had not produced any collisions. My service work consisted of looking at the effect of problematic cells on the performance of missing transverse energy using cosmic ray data. Once the first proton-proton collisions took place in the Fall of 2009, I continued my service work by studying pulse shape qualities in the Forward Calorimeters. In parallel, I started my physics studies in universal extra dimensions with gravity mediated decays.

My contribution to the analysis presented in this dissertation started by using Monte Carlo data to determine the feasibility of discovery for these universal extra dimension models. Once it was determined that this study had the potential to surpass previous limits with very early data, I moved my focus to determining the selection criterion for this search. In the Spring of 2010, 7 TeV collision data became available. At that time, I compared data versus Monte Carlo distributions for variables of interest and determined methods for obtaining the systematic uncertainties associated with the selection requirement of missing transverse energy. A paper describing the results in this dissertation has been published in the journal of Physical Review Letters [35]. In this dissertation I have added some Monte Carlo studies to further elucidate the data driven method used to determine the Standard Model background for this search.

After the publication of the paper described above, I continued working on this search with ten times more data. The follow-up search included limits on supersymmetric models as well and was published in the European Physics Journal C [31]. My contribution to this analysis consisted of looking at efficiencies related to the universal extra dimension signal and determining the systematic uncertainties of the missing transverse energy cut required in the selection criterion.

Chapter 2

Introduction

The Standard Model of Particle Physics describes three of the four fundamental forces of nature and has been developed over the past 50 years. Despite its many successes a few questions still remain unanswered. Models beyond the Standard Model attempt to address some of these shortcomings and make predictions that can be experimentally tested. Chapter 2 of this thesis summarizes some of the basic features of the Standard Model and ends with an overview of its shortcomings. Beyond the Standard Model scenarios which introduce extra dimensions are discussed in Chapter 3 with a focus on the particular models relevant for this thesis.

This thesis summarizes the search for particular extra dimension models in diphoton events with large missing transverse energy produced in proton-proton collisions at a center-of-mass energy of 7 TeV. The data were collected with the ATLAS detector at the CERN Large Hadron Collider during the period from March 30, 2010 until August 30, 2010 and corresponds to 3.1 pb^{-1} of integrated luminosity. An overview of the Large Hadron Collider and the ATLAS detector is given in Chapters 4 and 5 respectively. Limits are derived for a beyond the Standard Model scenario involving universal extra dimensions with gravity mediated decays. Universal extra dimensions are dimensions into which all Standard Model particles can propagate.

The Standard Model event rates for diphoton events with large missing transverse energy are small. Most of the contribution to the background for this search was from events faking this signature. These fake events arise from Standard Model processes in which mismeasurements lead to the desired signature. One of the main experimental challenges was to predict the Standard Model background to diphoton events with large missing transverse energy and to establish a set of appropriate selection criterion. This analysis used data to predict the background and understand some of the uncertainties associated with the selection criterion. Since this search was conducted with early data, novel approaches had to be adopted to fulfill these tasks. Chapter 6 provides an overview of the variables used to identify various final state particles and missing transverse energy. Chapter 7 describes the data samples used and the methodology for establishing the selection criterion for the search region. Chapters 8 and 9 describe the Standard Model Background prediction method and the systematic uncertainties attributed to the selection criterion respectively.

The methodology of this search was approved by the ATLAS collaboration in December of 2010 and was subsequently published in [35]. The search results are presented in Chapter 10, followed by conclusions in Chapter 11.

Chapter 3

Standard Model

Particle physics is the branch of physics that studies the fundamental constituents of matter and their interactions. The current theoretical framework for this endeavour is referred to as the Standard Model (SM) of elementary particle physics. This theory describes the electromagnetic, weak and strong interactions of the known subatomic particles, but also postulates the existence of a massive scalar particle, known as the Higgs boson, which may have recently been observed [37]. The success of this theory is based on the excellent agreement between its theoretical predictions and the ensuing experimental observations.

This chapter provides a brief summary of the basic constituents and principles of the Standard Model. This discussion is followed by a sample list of some of its shortcomings.

3.1 Basic Constituents of the Standard Model

The basic constituents of the Standard Model are shown in figure 3.1. The matter content consists of 12 elementary spin-$\frac{1}{2}$ fermions and their corresponding antiparticles. The fermions are classified according to their interaction properties. The quarks possess a color charge and interact via the strong force, whereas the leptons do not interact strongly. Pairs of each classification, quarks or leptons, are grouped into a generation.

There are 3 generations altogether. Each charged member of a generation has a greater mass than the previous one. The first generation of the leptons consists of the electron, e, and the electron neutrino, ν_e. The electron has an electric charge of -1 and can interact both electromagnetically and weakly, whereas the ν_e which is assumed to be massless in the Standard Model, has no electric charge and can only interact via the weak force. This pattern is repeated in the second and third generation with the muon, μ , and tau, τ, leptons and their corresponding neutrinos. The quarks can not only interact strongly, but also electromagnetically and weakly. The first generation of the quarks consists of the up and down quarks, the second generation contains the charm and strange quarks and the third generation contains the top and bottom quarks. The electromagnetic charge of the members of each quark generation differs by one unit of the electric charge, but they carry a fractional charge of $\frac{2}{3}$ for the up-type quarks and $-\frac{1}{3}$ for the down-type quarks. No free quarks have ever been detected, because they are confined by the strong force to form color neutral composite particles known as hadrons (eg. protons, neutrons and pions).

In the Standard Model, matter particles interact with each other through the exchange of other particles, known as gauge bosons or force carriers. The force carriers are all spin-1 bosons. The gauge boson associated with the electromagnetic interaction is the massless photon. The three massive $W^{\pm}$ and Z bosons are the mediators of the weak interactions. The $W^{\pm}$ are charged and only act on left-handed particles or right-handed antiparticles. The photon along with the $W^{\pm}$ and Z mediate the electroweak interactions. The 8 colored massless gluons mediate the strong interactions between the quarks. As mentioned before, the Higgs particle is included in the Standard Model and may have recently been observed experimentally. The mass of the new particle that has been observed by the ATLAS experiment was measured to be 126.0±0.4(stat)±0.4(syst) GeV. Its SM conception is that of a spin-0 boson which carries no electromagnetic or color charge.

Figure 3.1: *The constituents of the SM excluding the Higgs boson. The matter content consists of three generations of spin-$\frac{1}{2}$ fermions. Forces are mediated by spin-1 bosons.*

3.2 Basic Principles of the Standard Model

3.2.1 Free Fields and Gauge Interactions

The Standard Model is a relativistic quantum field theory formulated on a (3+1) dimensional Minkowski space. Quantum excitations of these fields are interpreted as point-like particles. Relativistic invariance requires the Lagrangian of the theory to be invariant under Poincaré transformations. This implies invariance of the Lagrangian under translations through time, translations through space, and the Lorentz transformations; ie. rotations or boosts to a different frame of reference. The basic constituents of the Standard Model are the quarks and leptons which are spin 1/2 fermions, the force carriers which are spin 1 bosons and the Higgs boson which is a spin 0, or scalar, particle. The spin of a particle determines how the fields representing them will transform under Lorentz boosts and rotations.

Poincaré invariance is an example of a global symmetry. The Lorentz invariant La-

grangian density for a free spin-$\frac{1}{2}$ fermionic field, $\psi(x)$, of mass m is given by:

$$\mathscr{L}_f = \bar{\psi}(x)(i\gamma^\mu\partial_\mu - m)\psi(x) \tag{3.1}$$

where $\bar{\psi} = \psi^\dagger\gamma^0$ and γ^μ are 4×4 Dirac matrices which are given by:

$$\gamma^\mu = \begin{pmatrix} 0 & \sigma^\mu \\ \bar{\sigma}^\mu & 0 \end{pmatrix} \tag{3.2}$$

Above, $\sigma^\mu = (I, \sigma^1, \sigma^2, \sigma^3)$ and $\bar{\sigma}^\mu = (I, -\sigma^1, -\sigma^2, -\sigma^3)$. This representation is called the Weyl representation. The matrix I is just the 2×2 identity matrix and σ^i are the Pauli spin matrices.

One way to introduce interactions to fermionic fields is through the principle of gauge invariance. Gauge transformations are transformations that vary independently at every point in spacetime. The principle of gauge invariance requires that the Lagrangian be invariant under these transformations up to a total derivative. A simple example of this principle can be illustrated by stipulating that our theory should be invariant under local $U(1)$ transformations of a Dirac field $\psi(x)$,

$$\psi(x) \rightarrow U_1(x)\psi(x) = e^{i\alpha(x)}\psi(x) \tag{3.3}$$

The mass term in the Dirac Lagrangian density, $m\bar{\psi}\psi$, remains invariant under such a transformation. However, the kinetic term in the Lagrangian will not be invariant,

$$i\bar{\psi}(x)\gamma^\mu\partial_\mu\psi(x) \rightarrow i\bar{\psi}(x)\gamma^\mu\partial_\mu\psi(x) - \bar{\psi}(x)\gamma^\mu\left[\partial_\mu\alpha(x)\right]\psi(x) \tag{3.4}$$

To achieve invariance of the Lagrangian density, the derivative ∂_μ is replaced by the covariant derivative D_μ:

$$\partial_\mu \rightarrow D_\mu = \partial_\mu + igA_\mu(x) \tag{3.5}$$

Under the same local U(1) transformations, the vector field A_μ in the covariant derivative transforms as follows:

$$A_\mu(x) \rightarrow A_\mu(x) - \frac{1}{g}\partial_\mu\alpha(x) \tag{3.6}$$

The term $i\bar{\psi}(x)\gamma^{\mu}D_{\mu}\psi(x)$ is now invariant and the new Lagrangian density has the following form:

$$\mathscr{L}'_f = i\bar{\psi}(x)\gamma^{\mu}\partial_{\mu}\psi(x) - g\bar{\psi}(x)\gamma^{\mu}A_{\mu}(x)\psi(x) - m\bar{\psi}(x)\psi(x) \tag{3.7}$$

The extra term that has been added $-g\bar{\psi}(x)\gamma^{\mu}A_{\mu}(x)\psi(x)$ looks like the interaction term in Quantum Electrodynamics between an electron with charge $g = e$ with an external electromagnetic potential $A_{\mu}(x)$. Therefore, the demand for local gauge invariance has generated interactions for the fermionic fields. The external potential $A_{\mu}(x)$ is treated as a free vector field by adding a kinetic term to the Lagrangian density which is in itself gauge and Lorentz invariant. The Lagrangian density for a free U(1) gauge field is given by:

$$\mathscr{L}_A = -\frac{1}{4}F^{\mu\nu}F_{\mu\nu} \tag{3.8}$$

where $F_{\mu\nu} = \partial_{\mu}A_{\nu} - \partial_{\nu}A_{\mu}$. The demand for gauge invariance implies new gauge fields and introduces interaction terms. A mass term for a gauge field $mA^{\mu}A_{\mu}$ will not be invariant under these transformations. Using the principle of gauge invariance cannot by itself describe the interaction of fermions with the massive $W^{\pm}$ and Z bosons. This principle will need to be supplemented with a mechanism that breaks the underlying gauge symmetry and generates masses for the gauge bosons of the weak sector. In section 3.3.1, this mechanism is reviewed along with its connection to the Higgs sector.

3.2.2 Chiral Fermions

One of the important consequences of spin considerations is the reducibility of massless fermionic fields into two different helicity states or chiralities. The left-handed helicity refers to a spin direction antiparallel to the momentum and the right-handed helicity refers to a spin direction parallel to the momentum. The Standard Model is a chiral theory because it treats these two helicity states differently in the electroweak sector. This treatment follows from the experimental observation that only left-handed neutrinos

and right-handed anti-neutrinos interact through the weak force. This is possible because the two helicity states of a spin-$\frac{1}{2}$ fermion can have different transformation properties under a given symmetry group or different quantum charges.

In order to see how these two helicity states appear in the Standard Model Lagrangian we can begin by considering the Lagrangian density in equation 3.1. The spinor fields are reducible, since the upper components of a spinor field don't mix with the lower components under Poincaré transformations. A spinor field can, therefore be written as:

$$\psi = \begin{pmatrix} \psi_L \\ \psi_R \end{pmatrix} \tag{3.9}$$

where,

$$\psi_L = \frac{1}{2}(1+\gamma^5)\psi; \quad \psi_R = \frac{1}{2}(1-\gamma^5)\psi \tag{3.10}$$

and,

$$\gamma^5 = \begin{pmatrix} I & 0 \\ 0 & -I \end{pmatrix} \left(= -i\gamma^0\gamma^1\gamma^2\gamma^3\right) \tag{3.11}$$

Therefore, equation 3.1 can also be written in the following form:

$$\mathscr{L}_f = i\psi_R^*\sigma^\mu\partial_\mu\psi_R + i\psi_L^*\bar{\sigma}^\mu\partial_\mu\psi_L - m(\psi_R^*\psi_L + \psi_L^*\psi_R) \tag{3.12}$$

The kinetic energy term for Dirac fermions splits into two separate expressions for left-handed and right-handed fields. When a fermion is coupled to a gauge field, then ψ_L and ψ_R can have different charges or different transformation properties under the gauge group. This is indeed what happens in the electroweak sector of the Standard Model. The mass term in equation 3.12 mixes the right and left handed helicities and would not be invariant under the gauge transformations if ψ_L and ψ_R have different charges. This is why the fermions in the Standard Model Lagrangian actually do not have explicit mass terms. The masses of the particles arise from their interaction with the Higgs field and will be discussed in section 3.3.1.

3.3 Gauge Groups of the Standard Model

The SM Lagrangian is invariant under transformations corresponding to the $SU(3)_C \times SU(2)_L \times U(1)_Y$ gauge group. In section 3.2.1, it was shown that gauge symmetries lead to interaction terms. The invariance of the SM Lagrangian under $SU(2)_L \times U(1)_Y$ is used to describe electroweak interactions and is summarized in section 3.3.1. The strong interactions are described by local $SU(3)_C$ symmetries and are briefly discussed in section 3.3.2.

3.3.1 Electroweak Interactions - $\mathbf{SU(2)}_L \times \mathbf{U(1)}_Y$

In 1961, Sheldon Glashow proposed a model to combine electromagnetic and weak interactions [61]. The interaction between fermions and the gauge fields associated with this symmetry group arises from the covariant derivative:

$$D_\mu = \partial_\mu - igW_\mu^a(x)T^a - ig'YB_\mu \tag{3.13}$$

where the label a runs from 1-3. The three gauge fields, W_μ^a, are associated with the symmetry group $SU(2)_L$ and B_μ is the field associated to the group $U(1)_Y$. The generators of the symmetry groups $U(1)_Y$ and $SU(2)_L$ are the weak hypercharge Y and the weak isospin matrices $T^a = \frac{\sigma^a}{2}$. The free field Lagrangian density for B_μ and W_μ^a is given by,

$$\mathscr{L}_{B,W} = -\frac{1}{4}B^{\mu\nu}B_{\mu\nu} - \frac{1}{4}W^{a\mu\nu}W_{\mu\nu}^a \tag{3.14}$$

where $B_{\mu\nu} = \partial_\mu B_\nu - \partial_\nu B_\mu$ and $W_{\mu\nu}^a = \partial_\mu W_\nu^a - \partial_\nu W_\mu^a - gf^{abc}W_\mu^b W_\nu^c$. The constants f^{abc} are the structure constants of $SU(2)_L$ satisfying $[T^a, T^b] = if^{abc}T^c$. The gauge fields B_μ and W_μ^a are not the physical fields of the theory. They can however mix to form the physical fields associated with the photon (A_μ), the Z boson and $W^\pm$ (W bosons):

$$W_\mu^\pm = \frac{1}{\sqrt{2}}\left(W_\mu^1 \mp iW_\mu^2\right)$$

$$A_\mu = W_\mu^3 sin\theta_w + B_\mu cos\theta_w \tag{3.15}$$

$$Z_\mu = W_\mu^3 cos\theta_w - B_\mu sin\theta_w$$

The mixing angle θ_w is an experimentally determined parameter, which relates the electric charge e to the coupling strengths g and g':

$$e = g sin\theta_w = g' cos\theta_w \tag{3.16}$$

The covariant derivative in equation 3.13 can be rewritten in terms of the physical fields:

$$D_\mu = \partial_\mu - i\frac{g}{\sqrt{2}}\left(W_\mu^+(x)T^+ + W_\mu^-(x)T^-\right) - i\frac{g}{cos\theta_w}Z_\mu\left(T^3 - sin^2\theta_w Q\right) - ieA_\mu Q \tag{3.17}$$

where $T^\pm = (T^1 \pm iT^2)$ and Q is the electric charge quantum number and is defined by $Q = T^3 + Y$. In this model the left-handed fermion fields are assigned to the doublets of $SU(2)_L$. For the first generation left-handed lepton and quark doublets,

$$E_L = \begin{pmatrix} \nu_e \\ e^- \end{pmatrix}_L \quad ; \quad Q_L = \begin{pmatrix} u \\ d \end{pmatrix}_L \tag{3.18}$$

the respective assignment of hypercharge $Y = -1/2$ and $Y = +1/6$ combines with $T^3 = \pm 1/2$ to give the conventional electric charge. The right handed fields, on the other hand, are singlets of $SU(2)_L$ with $T^i = 0$. The value of the hypercharge for the right-handed fermions is chosen in order to obtain the desired electric charge. These quantum numbers are summarized in table 3.3.1.

Table 3.3.1 shows that the left-handed and right-handed fermions have different weak isospin and hypercharge quantum numbers. An explicit gauge invariant mass term is therefore not possible for these particles. As mentioned in section 3.2.1, a gauge invariant mass term is also not possible for the spin-1 bosons in this sector. However, we know that both fermions and the W and Z bosons need to acquire mass somehow. This is achieved in the Standard Model through the introduction of the Higgs field which spontaneously breaks the symmetry group $SU(2)_L \times U(1)_Y$ to $U(1)_{em}$. The same mechanism is also responsible for giving masses to the fermions.

In order to implement this hidden symmetry mechanism, a complex scalar field which is also a weak isospin doublet is introduced into the Standard Model. The external

Leptons			Spin	T^3	Y	Q
$\begin{pmatrix} \nu_e \\ e^- \end{pmatrix}_L$	$\begin{pmatrix} \nu_\mu \\ \mu^- \end{pmatrix}_L$	$\begin{pmatrix} \nu_\tau \\ \tau^- \end{pmatrix}_L$	$\frac{1}{2}$ $\frac{1}{2}$	$\frac{1}{2}$ $-\frac{1}{2}$	$-\frac{1}{2}$ $-\frac{1}{2}$	0 -1
e_R	μ_R	τ_R	$\frac{1}{2}$	0	-1	-1
Quarks			**Spin**	T^3	**Y**	**Q**
$\begin{pmatrix} u \\ d \end{pmatrix}_L$	$\begin{pmatrix} c \\ s \end{pmatrix}_L$	$\begin{pmatrix} t \\ b \end{pmatrix}_L$	$\frac{1}{2}$ $\frac{1}{2}$	$\frac{1}{2}$ $-\frac{1}{2}$	$\frac{1}{6}$ $\frac{1}{6}$	$\frac{2}{3}$ $-\frac{1}{3}$
u_R	c_R	t_R	$\frac{1}{2}$	0	$\frac{2}{3}$	$\frac{2}{3}$
d_R	s_R	b_R	$\frac{1}{2}$	0	$-\frac{1}{3}$	$-\frac{1}{3}$
Higgs			**Spin**	T^3	**Y**	**Q**
$\phi = \frac{1}{\sqrt{2}} \begin{pmatrix} \phi^+ \\ \phi^0 \end{pmatrix}$			0 0	$\frac{1}{2}$ $-\frac{1}{2}$	$\frac{1}{2}$ $\frac{1}{2}$	1 0

Table 3.1: *Fermion and scalar field content of the Standard Model. The quoted quantum numbers are spin, T^3 - the 3rd component of the weak isospin, Y - the weak hypercharge, and Q - the electric charge. These values are given for both the left-handed and right-handed fermions, distinguished by subscripts L and R respectively.*

potential energy of this field is chosen such that it acquires a non-vanishing minimum. This minimum value, $|\phi_0|$, can be gauge transformed to take on the following form,

$$|\phi_0(x)| = \sqrt{\frac{1}{2}} \begin{pmatrix} 0 \\ v \end{pmatrix} \qquad (3.19)$$

where v is the vacuum expectation value of the scalar field. Although the Lagrangian of the Standard Model is invariant under $SU(2)_L \times U(1)_Y$ gauge transformations, the ground state does not retain this symmetry due to the non-vanishing vacuum expectation value of the scalar field. The electrically neutral vacuum state does, however, preserve a $U(1)_{em}$ gauge symmetry which is identified with the electromagnetic sector. Perturbations of the two component complex scalar field about its ground state can be gauge transformed to the form, *v+h(x)*, where *h(x)* is a real scalar field. The quantum of the field *h(x)* is called the Higgs boson. Writing the kinetic energy term, $|D_\mu\phi|^2$, for the complex scalar field about this minimum gives rise to the following masses for the gauge bosons of the electroweak sector,

$$m_W = g\frac{v}{2}$$
$$m_Z = \sqrt{g^2 + g'^2}\frac{v}{2}$$
$$m_A = 0 \qquad (3.20)$$

The W and Z bosons obtain masses proportional to v and the photon remains massless. The relationship between the masses of the W and Z bosons, $m_W = m_Z cos\theta_w$, has been satisfied experimentally to better than 1% accuracy. Furthermore, from the measured masses of the W and Z bosons and the couplings g and g' the vacuum expectation value of the Higgs field has been determined to be $v = 246$ GeV. The particular choice for the parametrization of $|\phi_0|$ makes the physical content of the model more evident. Three of the four degrees of freedom of the complex scalar field ϕ can be associated with the longitudinal degrees of freedom of the W and Z bosons which appear massive in the ground state.

Mass terms for the leptons and quarks of the Standard Model are generated through their interactions with the field ϕ, also known as Yukawa interaction terms. The gauge invariant Yukawa interaction term involving e_L, e_R and ϕ is as follows:

$$\mathscr{L}_{Yukawa,e} = -\lambda_e \bar{E}_L.\phi e_R + h.c. \tag{3.21}$$

where E_L is the first generation lepton doublet defined in equation 3.18 and λ_e is a dimensionless parameter that is introduced for every mass term. The term in equation 3.21 is now a singlet of $SU(2)_L$ and has net hypercharge $Y = 0$. If ϕ is replaced by its vacuum expectation value then one obtains,

$$\mathscr{L}_{Yukawa,e} = -\frac{1}{\sqrt{2}}\lambda_e v \bar{e}_L e_R + h.c. + ... \tag{3.22}$$

which just gives a mass term for electrons of value,

$$m_e = \frac{1}{\sqrt{2}}\lambda_e v \tag{3.23}$$

The masses of quarks are generated via a very similar mechanism, but with some additional complexities. The complexities essentially arise from the fact that the quark basis that diagonalizes their Higgs couplings is not the same as that related to their gauge couplings. The two bases are however related by unitary transformations that would allow for transitions between quark generations through weak interactions. The masses of all the quarks, leptons and gauge bosons are proportional to the vacuum expectation value of the scalar field v. These masses can however differ by large orders of magnitude. The order of magnitude of differences in mass are not explained in the Standard Model but are introduced as inputs of the theory.

3.3.2   Strong Interactions - SU(3)$_C$

The theoretical framework in the Standard Model that describes the strong interaction of quarks and gluons is referred to as Quantum Chromodynamics (QCD). These interactions

are introduced by requiring the invariance of the Standard Model Lagrangian under $\mathrm{SU(3)}_C$ transformations. The quarks are assumed to carry an additional quantum number referred to as *color* which can take on three possible values. There are eight massless gauge fields in this sector that are referred to as gluons. Gluons are themselves charged under $\mathrm{SU(3)}_C$ and can therefore self-interact. The covariant derivative that leads to interactions between quarks and gluons is given by,

$$D_\mu = \partial_\mu - ig_s G_\mu^b(x)\frac{\lambda^b}{2} \tag{3.24}$$

where the label b runs from $1-8$. The eight gauge fields G_μ^b are associated with the gluons. The generators of the $\mathrm{SU(3)}_C$ symmetry group are $\frac{\lambda^b}{2}$, where λ^b are the 3×3 Gell-Mann matrices which are traceless, Hermitian matrices obeying the relation $Tr(\lambda^b\lambda^c) = 2\delta^{bc}$. The free field Lagrangian density for G_μ^b is given by,

$$\mathscr{L}_G = -\frac{1}{4}G^{b\mu\nu}G_{\mu\nu}^b \tag{3.25}$$

where $G_{\mu\nu}^b = \partial_\mu G_\nu^b - \partial_\nu G_\mu^b - g_s g^{abc}G_\mu^b G_\nu^c$. The constants g^{abc} are the structure constants of the group $\mathrm{SU(3)}_C$. An important feature of QCD is that quarks and gluons interact very weakly at high energies or short distance scales. This property is referred to as asymptotic freedom and depends on the particle content of the theory. It explains experimental observations which suggested that free point-like spin-$\frac{1}{2}$ particles, termed quarks, are confined within hadrons. QCD was the last major theoretical ingredient in the formation of the Standard Model.

3.4   Limitations of the Standard Model

The Standard Model of particle physics does not include gravitational interactions, it does not address the origins of dark energy or provide any dark matter candidates, it does not account for neutrino masses or provide an explanation for the prevalence of matter over antimatter in the universe. Furthermore, it contains 19 free parameters

which include an unexplained fermion mass hierarchy and disparate gauge groups. The mechanism for electroweak symmetry breaking involving the Higgs field, discussed in section 3.3.1, introduces a fine tuning problem commonly referred to as the hierarchy problem which will be summarized in this section.

All the fundamental couplings including mass terms in the Standard Model are subject to quantum corrections which makes the measurement of these parameters dependent on energy. The squared mass of the Higgs boson is highly sensitive to radiative corrections. The squared mass of the Higgs boson is proportional to the vacuum expectation value of the Higgs field which is at the electroweak scale and set the W and Z boson masses on the order of 100 GeV. The radiative corrections to the squared mass of the Higgs boson are quadratically divergent in terms of the scale of a more fundamental theory. If it is assumed that the scale of the fundamental theory is where gravitational interactions become strong, then one manifestation of the hierarchy problem is the question that asks why the weak force is 10^{32} times stronger than gravity.

Many "Beyond the Standard Model" scenarios have been proposed that attempt to address some of the limitations summarized above. In the following section models involving extra dimensions are introduced. Some of these models predict that the dynamics of a more complete theory including gravity may be revealed near the electroweak scale. Models of extra dimensions do not address all the shortcoming of the Standard Model, but they do introduce a rich set of theoretical predictions that can be experimentally tested.

Chapter 4

Universal Extra Dimensions

This chapter provides an outline of the universal extra dimension model considered in this analysis. Section 4.1 provides a brief summary of the motivation for introducing the notion of extra dimensions and an outline of a few of the ways, relevant to this analysis, in which this can be achieved. The limits on the parameters of these models are also described. In section 4.2, the particular model investigated in this search, ie. universal extra dimensions with gravity mediated decays, is described. Furthermore, the choice of parameters for this model are motivated throughout and the final state signature is stated.

4.1   Extra Dimensions

The notion of extra dimensions was first explored as a physical phenomenon in the beginning of the 20th century in order to unify the known forces of nature at the time, ie. gravity and electromagnetism. Finnish physicist Gunnar Nordström proposed a 5-dimensional(5D) theory describing electromagnetism and a scalar version of gravity in 1914 [76] [75], however, this theory was abandoned, in part, due to its inability to explain the deflection of light in a gravitational field which was observed during a solar eclipse in 1919. The next attempt at unifying the known forces using the paradigm of extra

dimensions, was made by Theodor Kaluza in 1921 [66] who proposed a unified theory based on a 5D version of Einstein's theory of General Relativity. The same theory was independently rediscovered by Oskar Klein in 1926 [68]. Kaluza and Klein showed that a 5D version of Einstein's theory of general relativity in which one spatial dimension is compactified on a circle has the potential to describe 4D gravity and electromagnetism. However, these early attempts were abandoned in favour of 4D quantum field theories, upon which, the Standard Model of elementary particles is based, and the experimental confirmations of its predictions.

The interest in higher dimensional theories was renewed in the late 70's and 80's with the development of string theories, which required the existence of extra dimensions for consistency. These extra dimensions were, however, considered to be extremely small, $O(M_{pl}^{-1} \approx 10^{-35}m)$, and beyond experimental reach. The potential phenomenological implications of such models became popular in the late 90's when they were proposed as a possible solution to the hierarchy problem. The phenomenology of extra dimensions has been an active area of research for the past 20 years and includes various proposed models inspired by string theory but not bound by it. These models vary in the number of extra dimensions they consider, their geometry, method of compactification, and the field content that can propagate into them. The commonality in all of these models is the notion that our ordinary 4D space is embedded in a higher dimensional 4+N dimensional space known as the "bulk". From this higher dimensional perspective, our world would appear as a 4D "brane" which can in itself either be infinitely thin or have some finite thickness. Some of the issues within the Standard Model which have been addressed employing extra dimensions are as follows [78]:

- Addressing the hierarchy problem [74] [77].

- Producing electroweak symmetry breaking without a Higgs boson [14].

- The generation of ordinary fermion and neutrino mass hierarchy [10].

- TeV scale grand unification or unification without SUSY while suppressing proton decay [25].

- New Dark Matter candidates and a new cosmological perspective [9] [20].

The above is, of course, a small selection of what has been addressed in this context and is not specific to any single model of extra dimensions. Two models that are relevant to this analysis are the large extra dimension scenarios of Arkani-Hamed, Dimopoulos and Dvali (ADD) [74] and Universal Extra Dimensions [9]. The basic concepts underlying these models will be briefly outlined in sections 4.1.1 and 4.1.2 respectively.

4.1.1 ADD Scenario

In the ADD scenario, all SM particles live on a 4D brane, however, gravity is allowed to propagate into a (4+n)D bulk. In the simplest scenario, the n dimensions are compactified on an n-torus, T^n. A general feature of these types of models is the existence of a tower of Kaluza-Klein graviton excitations. This concept will be covered in a bit more depth in section 4.1.2, but it can simply be explained as introducing a whole set of excited gravitons into the 4D space with mass splitting on the order of the compactification radius of the extra dimensions, $\Delta m \approx 1/R$. This scenario was originally proposed as a solution to the hierarchy problem. According to Gauss' law, the 4D scale of gravity is naturally weak because it is diluted by its propagation into the (4+n)D bulk according to the formula:

$$M_{pl}^2 = M_D^{n+2} V_n \tag{4.1}$$

where M_{pl} is the Planck scale in 4D ($\approx 10^{19}$ GeV), M_D is the fundamental scale of gravity or the Planck scale in (4+n)D and V_n is the volume of the compact extra dimensions and is proportional to R^n. Here, R is the compactification radius of the extra dimensions. In order for this scenario to provide a solution to the hierarchy problem, the fundamental

Planck scale in (4+n)D has to be on the same order as the electroweak scale O(TeV). This implies [19]:

- If n=1: The length scale of the compact dimensions are $\approx 10^{13}$ m. This scenario is obviously ruled out because no deviation from classical gravitation has been observed at this length scale.

- If n=2: The length scale of the compact dimensions are ≈ 1 mm. This was allowed in 1998 when the first ADD scenarios were being introduced, but current bounds coming from table-top experiments [67] [82] place an upper bound of O(1-10 μm) on the possible size of these dimensions.

- If n>3: The length scale of the compact dimensions are $< 10^{-2}\mu$m, O(MeV^{-1}- eV^{-1}). Such large compactification scales for extra dimensions have not yet been ruled out.

For such large extra dimensions, the mass splittings between the graviton excitations are very small and the mass spectrum can be viewed as nearly continuous. The couplings of these excited gravitons with the SM particles is as weak as that of the zero mode. However, because there is such a large density of states, they can collectively affect SM production cross sections once they are integrated over. The excited gravitons themselves interact weakly and are expected to not scatter or decay inside a detector and will, therefore, appear as missing energy or momentum. Direct searches performed during Run I [7] and Run II [27] at the TeVatron and even the most recent constraints from ATLAS [5] have not imposed severe restrictions on this set of parameters. Using 1fb^{-1} of integrated luminosity, ATLAS has set a lower bound of $M_D > 3.2(2)$ TeV for the n=2(6) scenarios. It should also be noted that most lower bounds placed on M_D, ie. using cosmological arguments, electroweak precision data, etc., severely constrain the low n scenario but yield significantly weaker bounds as n increases [64]. For example, the assumption that M_D is O(TeV) is not constrained for n= 6 scenarios. These experimental

constraints motivated the search for the modified n=6 models described in section 4.2. Naturally, the choice of n=6 or 7 is also favoured if one assumes that superstring theory is relevant to high energy physics. Perhaps the most compelling reason for considering higher n models comes from naturalness arguments. It has been argued that the ADD scenario does not eliminate the hierarchy problem, but merely hides it [77]. In other words, we can now ask why the compactification scale, $1/R$, of the extra dimensions is so much smaller than the weak scale? Since $RM_D \approx (M_{pl}^2/M_D^2)^{1/n}$, then for small values of n the hierarchy problem will be replaced by another large ratio, whereas for the large n scenarios this issue is not so severe.

4.1.2 Minimal Universal Extra Dimension Scenario

Universal extra dimensions are dimensions into which all SM particles can propagate. Such a scenario would predict a tower of excited states for every SM particle, whose masses would be of order $1/R$. Since no such particles have been observed experimentally, the lower bound on the compactification radius of these extra dimensions would have to be $\leq O(\text{TeV}^{-1})$. Such scales would not address the hierarchy problem discussed in section 4.1.1. As a side note, if only a few of the extra dimensions were small, but others were large and only accessible to gravity, then the fundamental scale M_D would still be lowered by a factor related to the volume of the large extra dimensions and this problem could be avoided. Prior to the introduction of universal extra dimensions, scenarios in which only a subset of SM particles were able to propagate into these additional dimensions were considered. These scenarios were of interest because they could address issues such as gauge coupling unification [25], provide new mechanisms for supersymmetry breaking [8], generation of fermion mass hierarchies [11] etc. However, the size of these extra dimensions were also severely constrained by precision electroweak data. For example, in a scenario in which the gauge bosons are allowed to propagate into one extra dimension, the experimental constraint on the size of this dimension is $1/R > 6.6$

TeV [22]. However, it was shown [9] that in the case of universal extra dimensions, this lower bound could be much weaker $O(10^2$ GeV). The main reason for this had to do with the emergence of Kaluza-Klein (KK) number conservation, which leads to the effect that there are no vertices involving only one non-zero KK mode. This restriction limits the impact of KK states to the loop level and suppresses their contribution to electroweak observables [9]. In addition, it renders the lightest Kaluza-Klein particle stable and introduces a potential dark matter candidate.

In order to elucidate how the introduction of a compact dimension can lead to a tower of KK particles with mass splittings of order $1/R$, assume a $4+\delta$ dimensional space, where the dimension δ is compactified on a circle. For simplicity, it is sufficient to just consider the $\delta = 1$ scenario. The coordinates of this space are denoted by $x^A = (x^\mu, y)$, where A runs from 0-5, $\mu = 0, 1, 2, 3$ and labels the coordinates of our ordinary 3+1 dimensional Minkowski space, and $y = x^5$ is the coordinate for the compact dimension. Compactification on a circle implies that points y and $y + 2\pi R$ are identified. If we consider just the simplest case of one real scalar field Φ with mass m_0 living in this world, then the action for this field in 5D is:

$$S = \int d^5x \left(\frac{1}{2}\partial_A\Phi(x^\mu, y)\partial^A\Phi(x^\mu, y) - \frac{1}{2}m_0^2\Phi^2(x^\mu, y) \right) \tag{4.2}$$

The compactification of the extra dimension, translates into a periodicity condition on the field in the y coordinate, such that $\Phi(x^\mu, y) = \Phi(x^\mu, y + 2\pi R)$. This allows us to Fourier decompose Φ in the y direction:

$$\Phi(x^\mu, y) = \frac{1}{\sqrt{2\pi R}} \sum_{n=-\infty}^{n=\infty} \phi^{(n)}(x^\mu)e^{i\frac{n}{R}y} \tag{4.3}$$

Plugging the Fourier series expansion of Φ into the the action gives:
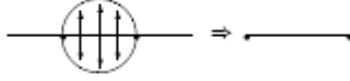
Figure 4.1: *The S^1/Z_2 orbifold [19].*

$$S = \int d^4 x \sum_{k,n} \left(\int_0^{2\pi R} dy \frac{1}{2\pi R} e^{i\frac{k+n}{R}y} \right) \frac{1}{2} \left[\partial^\mu \phi^{(k)}(x) \partial_\mu \phi^{(n)}(x) + \frac{kn}{R^2} \phi^{(k)}(x)\phi^{(n)}(x) - m_0^2 \phi^{(k)}(x)\phi^{(n)}(x) \right]$$

$$= \int d^4 x \frac{1}{2} \sum_n \left[\partial^\mu \phi^{(-n)}(x) \partial_\mu \phi^{(n)}(x) - \frac{n^2}{R^2} \phi^{(-n)}(x)\phi^{(n)}(x) - m_0^2 \phi^{(-n)}(x)\phi^{(n)}(x) \right] \qquad (4.4)$$

$$= \int d^4 x \frac{1}{2} \left\{ \partial^\mu \phi^{(0)}(x) \partial_\mu \phi^{(0)}(x) - m_0^2 \phi^{(0)}(x)\phi^{(0)}(x) + \sum_{n+1}^{\infty} \left[\partial^\mu \phi^{(n)\dagger}(x) \partial_\mu \phi^{(n)}(x) - (m_0^2 + \frac{n^2}{R^2})\phi^{(n)\dagger}(x)\phi^{(n)}(x) \right] \right\}$$

Above used the condition $\phi^{(-n)} = \phi^{(n)\dagger}$, which comes from the assumption that Φ is real. It can be seen that in the effective 4D theory, the zero mode of this expansion retains the same characteristics as the original scalar field, ie. there is a real scalar with mass m_0. However, there are now also an infinite tower of particles with masses given by $m_{(n)}^2 = m_0^2 + \frac{n^2}{R^2}$. These particles are what were referred to previously as Kaluza-Klein excitations. The mode number of the Fourier expansion, n, refers to the nth Kaluza-Klein excitation. At this point the masses of these particles are almost degenerate for any given KK level, however, radiative corrections lift this degeneracy. Another consequence of such a decomposition is that it introduces KK number conservation at any given vertex, which prohibits mixing between any given KK level and leads to the behaviour that KK particles can only be produced in sets of two or more. KK number conservation also renders the Lightest KK Particle (LKP) in any given level stable. A similar type of decomposition can be performed for other types of fields. However, these decompositions could lead to an effective 4D theory that is not necessarily compatible with the matter content of the SM. Some problems that arise have to do with the fact that the SM is a chiral theory, but it is not possible to have chiral fermions from such a scheme

if the number of universal extra dimensions is odd. Another example comes from the fact that a similar decomposition for gauge fields gives rise to an additional scalar field zero mode which has not been observed. The solution to these problems would be to compactify on an orbifold. An orbifold is a manifold with a discreet symmetry that identifies different points on the manifold [78]. An example of such an orbifold is S^1/Z_2, which is also relevant to the model considered in this analysis. In these scenarios, the compactification on S^1 is followed by identifying y with -y. Figure 4.1 shows a schematic view of this orbifolding condition. Starting with a circle S_1, the Z_2 symmetry leads to a line segment with fixed points at $y = 0$ and $y = \pi R$, called the boundaries. The field content is then assigned either an even or odd parity under the $Z_2(y \rightarrow -y)$ symmetry, which ensures the desired zero mode matter content consistent with the Standard Model. The Fourier decomposition of all the 5D fields (fermions, scalars and gauge bosons) can be re-written as follows [79]:

$$
\begin{aligned}
Q = {} & \frac{1}{\sqrt{\pi R}} Q_L^0 + \frac{2}{\sqrt{\pi R}} \sum_{n=1}^{\infty} \left[Q_L^n cos\left(\frac{ny}{R}\right) + Q_L^n sin\left(\frac{ny}{R}\right) \right] \\
& + \frac{1}{\sqrt{\pi R}} Q_R^0 + \frac{2}{\sqrt{\pi R}} \sum_{n=1}^{\infty} \left[Q_R^n cos\left(\frac{ny}{R}\right) + Q_R^n sin\left(\frac{ny}{R}\right) \right] \\
q = {} & \frac{1}{\sqrt{\pi R}} q_L^0 + \frac{2}{\sqrt{\pi R}} \sum_{n=1}^{\infty} \left[q_L^n cos\left(\frac{ny}{R}\right) + q_L^n sin\left(\frac{ny}{R}\right) \right] \\
& + \frac{1}{\sqrt{\pi R}} q_R^0 + \frac{2}{\sqrt{\pi R}} \sum_{n=1}^{\infty} \left[q_R^n cos\left(\frac{ny}{R}\right) + q_R^n sin\left(\frac{ny}{R}\right) \right]
\end{aligned}
$$
(4.5)
$$
(\Phi, B_A^b) = \frac{1}{\sqrt{\pi R}}(\Phi_0, B_{\mu,0}^b, B_{5,0}^b) + \frac{2}{\sqrt{\pi R}} \sum_{n=1}^{\infty} \left[(\Phi_n, B_{\mu,n}^b, B_{5,n}^b)cos\left(\frac{ny}{R}\right) + (\Phi_n, B_{\mu,n}^b, B_{5,n}^b)sin\left(\frac{ny}{R}\right) \right]
$$

Here $Q(q)$ are the 5D fermionic doublets(singlets) under SU(2), Φ is the scalar Higgs field, B_A^b are the gauge fields of the 5D theory which can be separated into their polarizations along the 4D brane, B_μ^b, and those along the compact dimension, B_5^b. The zero modes of B_μ^b correspond to the Standard Model gauge fields, however, the zero modes of B_5^b would correspond to massless scalar fields which do not appear in the Standard Model. The chiral projection operators that appear in the KK decomposition of fermionic fields are

just the 4 dimensional ones, $P_{L,R} = (1 \mp \gamma_5)/2$. As mentioned previously, the correct SM matter content is obtained in these scenarios by assigning a parity to the 5D fields under the $Z_2(y \to -y)$ symmetry. Assigning the following parities to the fields in equation 4.5 can achieve this objective:

Even under $Z_2(y \to -y)$	Odd under $Z_2(y \to -y)$
$Q_L(x,y) = Q_L(x,-y)$	$Q_R(x,y) = -Q_R(x,-y)$
$q_R(x,y) = -q_R(x,-y)$	$q_L(x,y) = -q_L(x,-y)$
$B_\mu^b(x,y) = B_\mu^b(x,-y)$	$B_5^b(x,y) = -B_5^b(x,-y)$

This assignment projects out the zero modes that correspond to fields that are odd under the $Z_2(y \to -y)$ symmetry. Therefore, the zero modes of the gauge fields polarized along the compact dimension which would lead to massless scalar fields in the 4D theory are removed. This scheme also provides the correct chiral content for the SM zero mode particles, as follows:

$$Q = \frac{1}{\sqrt{\pi R}} Q_L^0 + \frac{2}{\sqrt{\pi R}} \sum_{n=1}^{\infty} \left[Q_L^n cos \left(\frac{ny}{R} \right) + Q_R^n sin \left(\frac{ny}{R} \right) \right]$$

$$q = \frac{1}{\sqrt{\pi R}} q_R^0 + \frac{2}{\sqrt{\pi R}} \sum_{n=1}^{\infty} \left[q_R^n cos \left(\frac{ny}{R} \right) + q_L^n sin \left(\frac{ny}{R} \right) \right]$$

$$(4.6)$$

The KK excitations of the fermions are, however, not chiral which leads to a doubling of the fermion content for n>0 KK modes.

The orbifolding condition essentially breaks translational invariance at the boundaries (y= 0 and y= πR). The consequence of this is that radiative corrections generate terms localized on the boundaries which break KK number conservation [70]. KK number conservation then becomes only an approximate effect relevant to tree level processes. However, a remnant of this conserved quantity, known as KK parity, which labels odd KK levels as odd and even KK levels as even is still preserved. This implies that the

first level KK excitations have to be pair produced and that the lightest first level KK excitation is stable [19]. These terms introduce log divergences at the one loop level which can only be controlled if a cut off scale Λ is introduced at which the boundary terms vanish. These terms also lift the mass degeneracy at any given KK level, giving rise to a mass shift approximated by the following expression:

$$\frac{\delta m_n}{m_n} \propto g^2 ln(\frac{\Lambda^2}{\mu^2}) \tag{4.7}$$

where g represents any coupling relevant for the particle under consideration and μ is the scale being looked at; if we are interested in production of KK particles then $\mu = m_{KK}$ is an appropriate choice. Although there are no clear indications as to what this scale should be, some rough restrictions have been placed arising from unitarity bounds on heavy gluon scattering cross-sections which require Λ to not be much bigger than $1/R$ [23]. A choice of $\Lambda R = 20$ is commonly used and has also been used in this analysis. In section 4.2 the effect of varying this choice is presented. Furthermore, the cut-off dependence for the effective theory becomes more severe as the number of compact universal dimensions is increased, which motivates our initial focus on the 1 UED scenario.

Figure 4.2 shows the effect of the one-loop corrections on the masses of the first level KK particles. The excited gluons are the heaviest particles and get the largest radiative correction of 30%, followed by the excited quarks, W's and Z. The smallest corrections of 5% are associated with the excited leptons and the lightest particle, the excited photon γ^*, hardly receives any correction to its mass. The consequences of this for hadron colliders is that in most scenarios the excited gluons/quarks will be produced in pairs and cascade decay down to the LKP, emitting Standard Model particles along the way. Since the mass splittings are not too large by collider standards, the emitted SM particles are usually 50-100 GeV jets. The LKP is stable, therefore, it will not decay and will show up as missing energy. These UED signal signatures are extremely difficult to isolate from normal QCD backgrounds. Using electroweak precision data, the compactification radius has been estimated to be $1/R > 300$ GeV [9]. If the LKP is to be considered as a dark
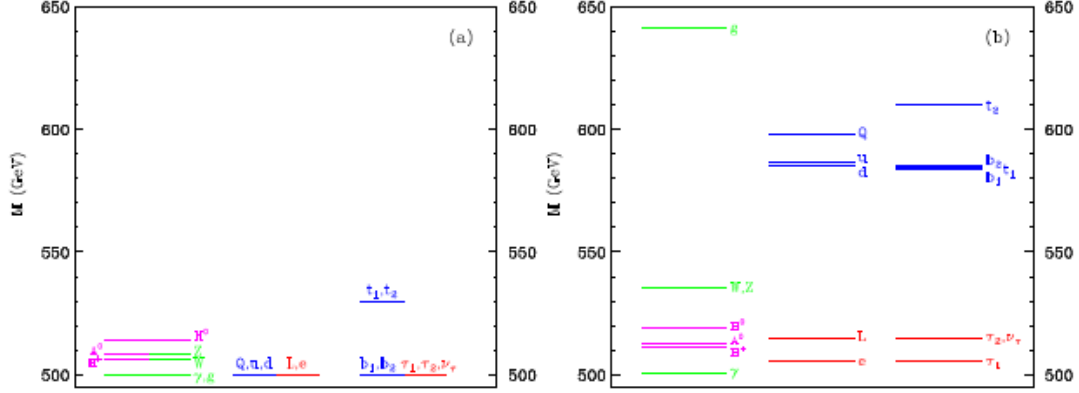
Figure 4.2: *The spectrum of the first KK level at tree level (left) and one-loop (right), for* $1/R$=*500 GeV*$/\bar{h}c$, $\Lambda R = 20$, $m_h = 120$ *and assuming vanishing boundary terms at the cut-off scale* Λ *[21].*

matter candidate, then its compactification radius has to satisfy $1/R < 1050$ GeV [18]. However, due to the difficulties associated with this signal mentioned previously, direct searches for these models often involve searching for multilepton channels that have a smaller branching ratio [18]. At the time of writing this thesis, the only direct search limit had been set by the CDF collaboration with $1/R > 280$ GeV [69]. However, this limit will most likely become much more stringent in the near future [73].

4.2 Universal Extra Dimensions With Gravity Mediated Decays

In this analysis a search for universal extra dimensions with gravity mediated decays has been conducted. The model can be considered as a combination of those described in sections 4.1.1 and 4.1.2, and is sometimes referred to as the 'fat brane scenario' [80] [72]. The model begins with a $(4+\delta+N)$ dimensional space. For us, $\delta = 1$, and refers to the dimension into which all SM particles can propagate, hence a universal extra dimension,

compactified on an S^1/Z_2 orbifold, and $N = 6$ refers to the number of large extra dimen-
sions with an eV^{-1} compactification radius (ADD scenario), into which only gravitons
can propagate. The theoretical motivation for these scenarios is that they combine the
benefits of both models. The ADD sector will address the hierarchy problem to some
extent and the UED sector is desirable because allowing SM particles to propagate into
extra dimensions has been shown to add a rich framework in which other issues with the
SM, such as electroweak symmetry breaking, can potentially also be addressed. How-
ever, the most interesting feature of these models is that they can lead to striking collider
signatures [72].

The introduction of large extra dimensions into which only gravity can propagate,
introduces gravity mediated KK parity violating interactions to the UED sector. The
cross-sections of these types of models can be O(10-100) times higher than those asso-
ciated with the minimal UED search scenarios involving multi-lepton final states and
described in section 4.1.2. It also means that the LKP, γ^*, will no longer be stable and
will decay to a photon and a KK graviton. In fact, all KK particles can now decay to
their SM counterparts and a KK graviton. However, if:

$$\Gamma(mass\ splitting) > \Gamma(gravity\ mediated) \tag{4.8}$$

then the KK excitations produced during collisions will first cascade decay to the LKP
as in the minimal UED scenario, but because of the gravitational interactions, the LKP
will no longer be stable and will decay via: $\gamma^* \to \gamma G_n$ [71]. The gravitational decay
width of the KK modes are proportional to:

$$\Gamma \propto \frac{1}{M_D^{N+2}} \tag{4.9}$$

Therefore, for the large $N = 6$ scenario and $M_D = 5$ TeV case considered in this analysis,
this decay width is very small. Also as long as $1/R < 1$ TeV the branching ratio for the
cascade decay down to the LKP with its subsequent decay into a graviton and photon
is close to unity [72]. For this analysis, we consider only the first level KK excitations.

(a)   (b)
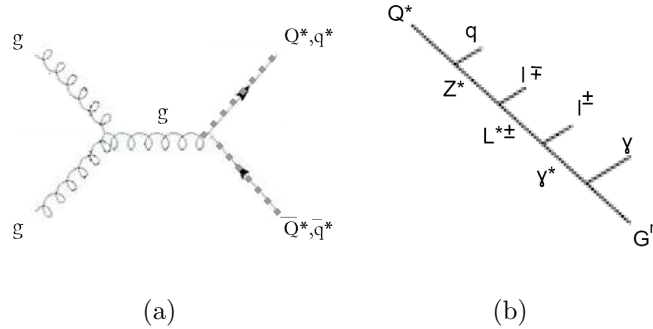
Figure 4.3: *(a) Production of a pair of KK-excited quarks (Q^*/q^*) via gluon gluon fusion and (b) a typical decay of a KK SU(2) doublet quark (Q^*) to the LKP (γ^*), which decays promptly via $\gamma^* \rightarrow \gamma G^n$ [53].*

The signal in this scenario will then be two hard photons plus large missing transverse energy. In proton-proton collisions, two first level KK partons (quarks and/or gluons) are pair produced due to KK parity conservation and each will subsequently cascade decay down to a γ^*'s. Each of the two γ^*'s will then decay to a photon and an excited graviton which will not interact with the detector and contribute to a missing transverse energy measurement. A typical production and subsequent decay is shown in figure 4.3.

The chosen parameter space for this analysis is models in which $\Lambda R = 20$, $\delta = 1$, N=6, and $M_D = 5$. The compactification radius of the universal extra dimension, R, is the parameter upon which a limit will be set. This model has been implemented in PYTHIA 6.421 [26]. The motivation for looking at this particular region of parameter space has been touched upon in sections 4.1.1 and 4.1.2. The choice for the cut-off scale Λ, ie. choosing $\Lambda R = 20$, is a bit less restricted. Changing Λ will change the radiative corrections to the KK particle masses, which will alter the KK pair production cross sections. The effects of changing ΛR from 10 to 30 have been studied and are summarized in table 4.1. The main restrictions on this value come from unitarity violation of heavy gluon scattering, which limits this product to lie between 10 to 40. We can see from this table that the production cross sections change more rapidly for lower ΛR values.

$\Lambda R =$	10	15	16	18	20	21	24	26	30
Cross section [pb]	3.41	2.99	2.95	2.88	2.73	2.72	2.60	2.56	2.43
Masses [GeV]									
$m(g^*)$	830	851	854	860	865	868	874	878	885
$m(q^*)$	788	804	806	811	815	817	822	825	830
$m(Z^*)$	734	739	740	741	743	743	745	746	748
$m(W^*)$	734	739	740	741	742	743	745	746	747
$m(l^*)$	715	718	718	719	719	720	721	721	722
$m(\gamma^*)$	700	700	700	700	700	700	700	700	700

Table 4.1: *The cross section and KK particle masses for different ΛR values and fixed $1/R = 700$ GeV.*

For example changing ΛR from 10 to 20 decreases the cross section by 22%, while it is only reduced by 12% when this value is changed from 20 to 30. The point $\Lambda R = 20$ is essentially the average of the range of potential variation. This variation will also change the mass splittings between the KK particles, leaving the LKP mass unchanged. Any change in the mass splitting will affect the level of hardness of the hadronic jets from the cascade decay in this analysis. Hadronic jets were not involved in defining the signal search region and should not significantly affect the final results.

The only previous search for this process was conducted by the D0 collaboration using 6.3 fb^{-1} of proton-antiproton collisions at $\sqrt{s} = 1.96$ TeV [53]. A lower limit of $1/R < 477$ GeV was set on the compactification radius of the universal extra dimension at 95% CL.

Chapter 5

Large Hadron Collider

CERN's Large Hadron Collider (LHC) [57] [58] [56] is a proton-proton and heavy ion synchrotron built inside a tunnel, 50 to 175 m underground with a 27 km circumference, straddling the Franco-Swiss border. The tunnel originally housed the Large Electron Positron (LEP) [62] [63] collider which was decommissioned in 2000. The LHC is designed to exceed the collision rates and energies of all other collider experiments to date, which enables it to probe physics of previously unexplored regions. This chapter provides a brief summary of the injection complex preceding the main LHC ring in section 5.1, followed by a brief description of the main ring itself in section 5.2 and concludes with a summary of some of the relevant parameters for this analysis in section 5.3. The description will focus on the LHC as a proton-proton accelerator and collider.

5.1   The LHC Injection Complex

The main purpose of the LHC injection complex is two-fold [56], figure 5.1. Proton beams occupy a larger phase space at lower energies and require larger apertures. The first purpose of the injection complex is therefore to save money by injecting higher energy beams into segments with smaller apertures. The second purpose has to do with the fact that every synchrotron has a transition energy at which the phase of the

The LHC injection complex
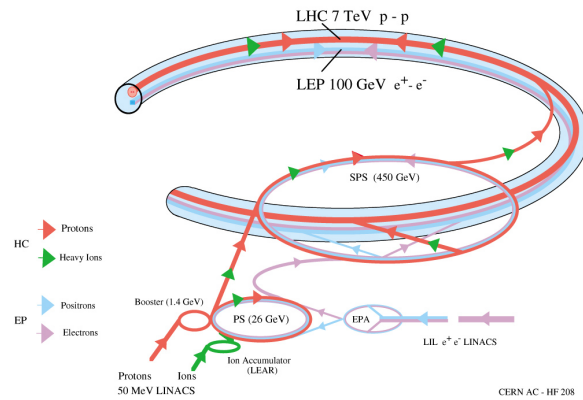
Figure 5.1: *The injection complex and main ring of the Large Hadron Collider [16].*

accelerating radio-frequency (RF) electric field has to change thereby leading to a loss of beam intensity. To avoid this loss in intensity, the beams are accelerated to just below this transition energy and injected into the next level of the chain just above the transition energy. To produce the proton source, hydrogen gas is ionized at the start of the Linac-2 accelerator. The Linac-2 is an 80m long linear accelerator which accelerates the protons to 50 MeV. The proton beam is then injected into the Proton Synchrotron Booster (PSB) where it is accelerated to 1.4 GeV and split into 3-4 parallel rings. The PSB injects 6 bunches of protons after 2 cycles into the Proton Synchrotron (PS) where they are boosted to 26 GeV and split into 72 bunches. These bunches are then transferred to the Super Proton Synchrotron (SPS). The main function of the SPS in the LHC injection complex is to accelerate proton bunches from the PS from 26 GeV to 450 GeV before extraction to the LHC ring tunnel. This whole process is repeated until both the counter-rotating LHC beams are filled and can take around 15 minutes to complete.

5.2   The LHC Main Ring

The main LHC ring [57], depicted in figure 5.2, is composed of 8 arcs and 8 straight sections. Each straight section is approximately 530 m long and serves as an insertion region for experiments or provides access to the beams for cleaning, dumping or acceleration. Two general purpose experiments, ATLAS [32] and CMS [51], are located diametrically opposite each other at Point 1 and Point 5 respectively. ALICE [44], an experiment which will mainly study heavy ion collisions, is located at Point 2. LHCb [28], a B physics experiment, is located at Point 8. The insertion regions for the two general purpose experiments at Point 1 and Point 5, also house LHCf [48] and TOTEM [38], the two forward scattering experiments at the LHC. Points 3 and 7 are used to access the beams for cleaning and collimation purposes. The beam access region at Point 6 is where the beam is dumped at the end of a fill or in case of a problem. Point 4 houses the RF acceleration system, where the proton beams can be accelerated to an energy of 7 TeV each. The RF system consists of two sets of superconducting cavities that provide independent control of the counter-rotating beams. The cavities are made of copper with a thin film of niobium on the inner surface. They use standing electromagnetic waves operating at a frequency of 400 MHz with an electric field aligned in the direction of particle motion to focus the protons into bunches. The beams are bunched because there is only a limited RF phase which leads to constant acceleration. The proton beams may consist of up to 2,808 bunches with a bunch spacing of 25 ns holding up to 1.5×10^{11} protons/bunch. The maximum number of bunches per beam reached for the dataset used in this analysis was 50. The two counter-rotating beams are housed in the same structure using a double beam pipe and are held in orbit by utilizing 1,232 15 m long dipole magnets. The dipole magnet coils are made of 36 strands which are, in turn, composed of 6000-9000 niobium-titanium filaments that become superconducting below 10 K. The strength of the dipole magnets determines the maximum energy that can be reached by a proton accelerator. By keeping the dipole magnets at a temperature of 1.9 K using superfluid
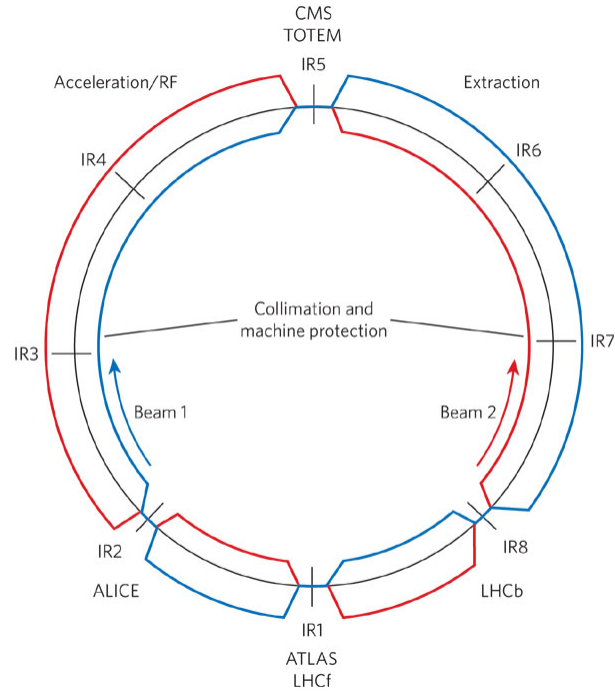
Figure 5.2: *Schematic layout of the LHC (Beam 1 - clockwise, Beam 2 - anticlockwise) [13].*

Helium, a magnetic field of up to 8.3 Tesla can be achieved which provides the lorentz force necessary to keep the proton bunches in orbit. Higher order magnets, including 392 quadrupoles, are installed around the ring to ensure orbital stability and beam focusing. The higher order magnets correct for the fact that the bending magnets and focusing magnets introduce chromatic aberations in the beam. The bunch structure has an RMS length of approximately 7.5 cm and a diameter of one millimeter when away from the collision points. However, the bunches are squeezed to a width of approximately 16 μm as they approach the collision points, thereby increasing the likelihood of a proton-proton collision.

5.3   The LHC - Parameters of Interest

The physics aim and potential of the LHC are enhanced by increasing the number of interesting collisions taking place at a given interaction point. The number of events per second, R_{events}, for any given process is given by:

$$R_{events} = L\sigma_{event} \tag{5.1}$$

where σ_{event} is the event cross-section and L is the luminosity. The cross-section, expressed in cm^2, is a measure of the probability that a collision will produce the particular event of interest. The Luminosity, measured in $cm^{-2}s^{-1}$, is determined by the the proton beam parameters as follows:

$$L = \frac{N_b^2 \times n_b \times f_{rev} \times \gamma_r}{4\pi \times \sigma_x \times \sigma_y}F \tag{5.2}$$

where N_b is the number of protons per bunch, n_b is the number of bunches per beam, f_{rev} is the revolution frequency, γ_r is the relativistic gamma factor, $\sigma_{x,y}$ is the RMS width of the beam for the coordinates transverse to the beam direction, and F is a geometrical factor which takes into account the crossing angle of the two colliding beams at the interaction point. The LHC aims for a design luminosity of $10^{34}cm^{-2}s^{-1}$ which would exceed the highest luminosity reached by the Tevatron by a factor of 50.

The dismantling of the LEP machine and the construction of the LHC began in 2001 and the first proton beams were successfully circulated on September 10, 2008. However, after a brief commissioning period a major accident imposed a 1 year stop. On November 23, 2009, the first 900 GeV collisions took place followed by 2.36 TeV collisions, which marked the world's highest beam energy collisions. There was then a winter shut-down. The 2010 operation, which is the focus of this analysis, began on March 30, 2010 with a center of mass energy of 7 TeV. The instantaneous luminosity during this period increased from 10^{27} to $10^{32}cm^{-2}s^{-1}$ and the LHC was able to deliver an integrated luminosity of $45pb^{-1}$ ($1pb = 10^{-36}cm^2$).

Chapter 6

The ATLAS Detector

6.1 Coordinate System and Definitions

The ATLAS Detector [1] uses a right-handed coordinate system in which the positive x-axis points towards the center of the LHC ring, the positive y-axis points upwards and the z-axis is along the beam line. The azimuthal angle, ϕ, spans a plane perpendicular to the beam axis and is measured from the positive x-axis in units of radians. The polar angle, θ, is measured with respect to the beam direction. Another useful variable is η, the pseudo-rapidity, expressed as:

$$\eta = -\ln(\tan\frac{\theta}{2}) \tag{6.1}$$

Large values of $|\eta|$ correspond to directions close to the beam axis or the forward/backward direction and $\eta = 0$ is perpendicular to the beam axis. Since particle production is expected to be uniformly distributed in η, the variable η is often used instead of θ to express the polar angle distribution of particles in an event. This is also the reason why the granularity of the ATLAS detector is finer in the forward direction, therefore, the detector granularity changes in θ but is almost constant when measured in η. Furthermore, at the

---

[1] Most of the information discussed in this chapter is a summary of [32]. Any sources beyond this main reference have been cited accordingly in the body of the text.

relativistic limit the pseudo-rapidity is a good approximation of the relativistic variable known as rapidity, y, expressed as:

$$y = \frac{1}{2} \ln\left(\frac{E + p_z}{E - p_z}\right) \tag{6.2}$$

The significance of this approximation at the relativistic limit is that even though the relative separation between particle directions in θ changes in a boosted frame, they remain invariant in η. Most of the collisions of interest will, furthermore, be boosted along the beam axis because protons are composite objects and the z-momentum of the interacting constituents will rarely be equal. The initial total momentum of the colliding constituents along the beam axis is unknown but the initial momentum in the transverse direction is known to be zero. For this reason, the transverse momentum, p_T is more commonly utilized and is expressed as follows:

$$p_T = \frac{|\vec{p}|}{\cosh \eta} \tag{6.3}$$

The angular separation ΔR between two particles with directions (η_1, ϕ_1) and (η_2, ϕ_2) is defined as:

$$\Delta R = \sqrt{(\eta_1 - \eta_2)^2 + (\phi_1 - \phi_2)^2} = \sqrt{\Delta\eta^2 + \Delta\phi^2} \tag{6.4}$$

This variable can be used to express the relative isolation of a given particle, for the determination of efficiencies and fake rates, or the identification of jets using the cone algorithm. The energy deposited by a typical photon, for example, is often contained in a cone of size $\Delta R \sim 0.2$.

6.2 General Layout

Weighing approximately 7000 tons with a height of 25 m and a length of 44 m, the AT-LAS detector shown in Figure 6.1, is one of the two general purpose experiments situated at the LHC. This cylindrically symmetric detector has a measurement capability extending out to $|\eta| = 4.9$. It consists of several sub-detectors employing various technologies

that are optimized in terms of cost, operational environment, and expected performance. The subdetectors are arranged radially in layers from the beam axis. The inner detectors, immersed in a 2 T solenoidal field, are situated closest to the beam pipe and are designed to provide an accurate measurement of charged particle trajectories and interaction/decay vertices in a high particle flux environment. Surrounding the inner detectors are the highly granular liquid argon (LAr) electromagnetic calorimeters which contain, measure, and identify the electromagnetic component of p-p collision products. This is followed by the hadronic calorimetry which consists of a combination of scintillator-tile and LAr-based calorimeters that are used in conjunction with the electromagnetic calorimeters for energy and position measurement and containment of hadronic jets and missing transverse energy determination. The calorimeters are surrounded by the muon spectrometer containing the toroid magnets which provide the strong bending power and the high resolution momentum reconstruction required for identifying, triggering on, and measuring the properties of muons in a given collision event. These sub-detectors will be further discussed in the following sections along with the triggering system used to handle the high collision rates provided by the LHC.

6.3   Inner Detector

At design luminosity, an average of 1000 particles within $|\eta| < 2.5$ are expected to emerge from collisions every 25 ns. The ATLAS inner detector is designed for high precision measurements of charged particle tracks and vertices without significantly disturbing the particles' original momenta. It consists of 3 complimentary subdetectors begining with the pixel detector closest to the beam pipe, followed by silicon microstrip (SCT) tracker and transition radiation tracker (TRT), as outlined in figure 6.2. The pixel detectors have 80.4 million readout channels, followed by 6.3 million and 351,000 readout channels associated with the SCT and TRT respectively. In fact, almost 97% of all the readout
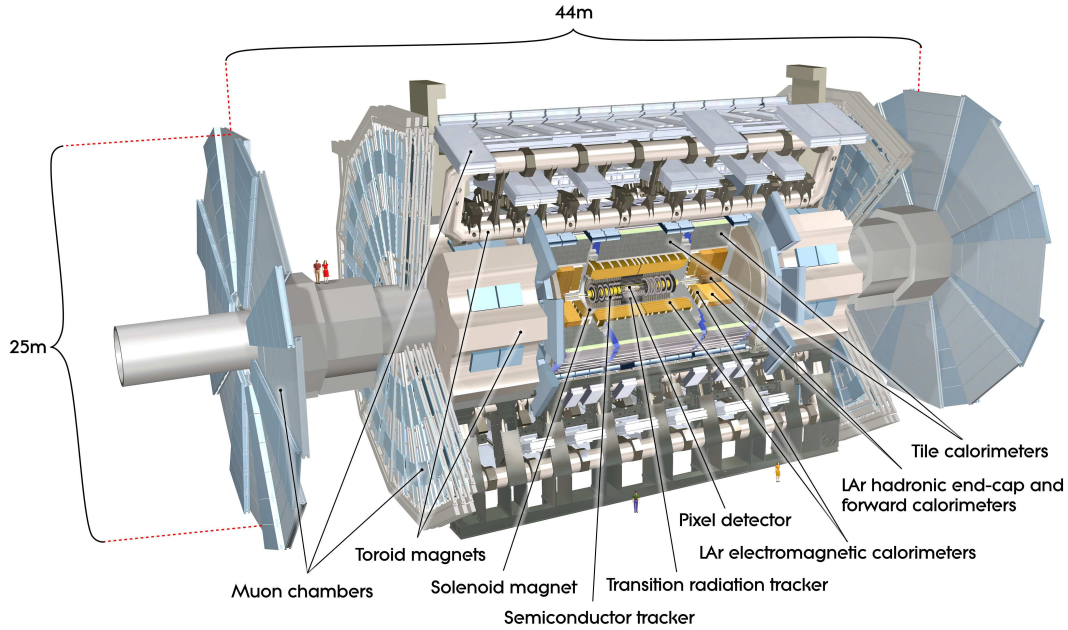
Figure 6.1: *Cut-away view of the ATLAS detector [32].*

channels in ATLAS belong to the inner detector. The inner detector is, furthermore, immersed in a 2 T solenoid magnetic field which, by bending charged particles, enables the measurement of their transverse momenta above a p_T threshold of 0.5 GeV/c and ensures a resolution per space-time point of less than $16\mu m$ in the bending direction.

The silicon pixel detector has the highest granularity for precision measurements and provides space point track measurements, which is important in a high multiplicity environment. It is arranged in 3 concentric cylindrical layers in the barrel region, corresponding to $|\eta| < 1.7$, at radii of 50.5 mm (called the B-layer), 88.5 mm, and 122.5 mm respectively. There are 3 end-cap layers on each side extending out to $|\eta| < 2.5$, which are circular discs perpendicular to the beam pipe positioned at $|z|$=495, 580, and 650 mm respectively. The individual pixels are doped semiconductors with a reverse biased voltage to increase the voltage barrier and allow minimal electric current to cross the p-n junction. The pixels consist of an n-type silicon bulk sandwiched between a more heavily doped n-type base and heavily doped p-type silicon at the surface. In the barrel,

6.2m

2.1m

Barrel semiconductor tracker
Pixel detectors
Barrel transition radiation tracker
End-cap transition radiation tracker
End-cap semiconductor tracker
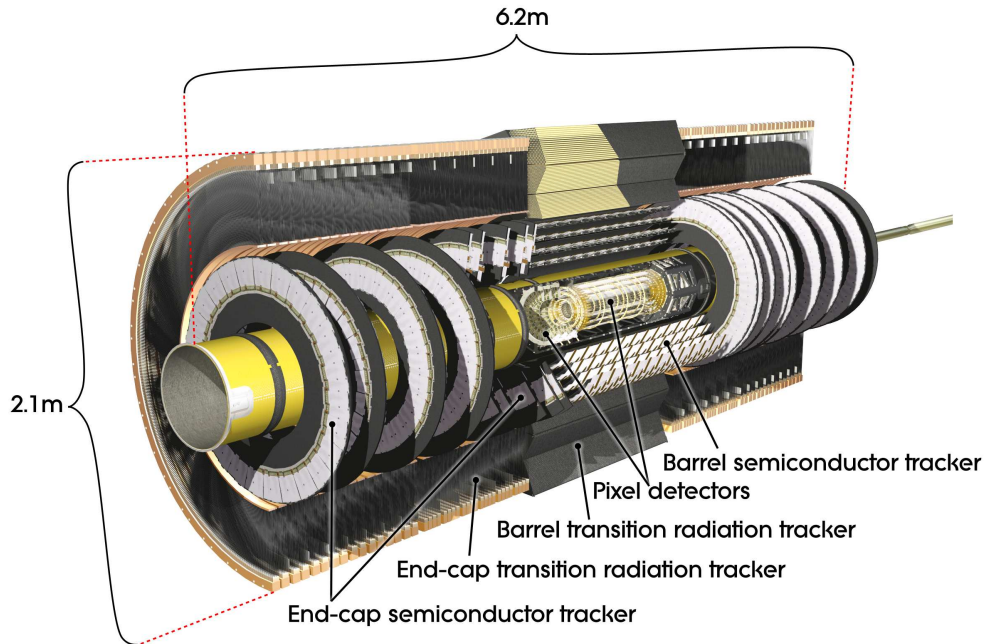
Figure 6.2: *Cut-away view of the ATLAS inner detector [32].*

the pixels extend 50 μm in the bending direction and 400 μm in the direction parallel to the beam pipe. The intrinsic accuracy is 10 μm (R-ϕ) and 115 μm (z) in the barrel and 10 μm (R-ϕ) and 115 μm (R) in the disks. When a charged particle enters the bulk, it creates a number of electron-hole pairs which are collected at the surface of the silicon. In order to reduce the contribution from electronic noise, this signal is compared to a threshold and a binary output is provided to the readout system which determines whether a given pixel has a 'hit' or not. Charged particles typically leave 3 hits in the pixel detector.

The SCT uses the same basic technology as in the pixel detector, but uses strips which have a coarser granularity and make it considerably cheaper allowing for coverage of a larger area. This is a desirable compromise because it leads to less traversed material due to a reduction in the density of the readout electronics and the expectation of a lower particle occupancy at larger radii. The SCT consists of 80 μm wide, 12 cm long silicon microstrips arranged in 4 cylindrical layers in the barrel, at R=299, 371, 443 and 514

mm, and 6 disks in each endcap , at $|z|$=890, 1091, 1350, 1771, 2115 and 2608 mm. The layers in the barrel and half of those in the endcap are double-sided, in that they consist of 2 sensors glued together with an angular offset of 40 mrad in order to measure both spatial coordinates. The intrinsic accuracy provided by the SCT is expected to be 17 μm (R-ϕ) and 580 μm (z) for the barrel and 17 μm (R-ϕ) and 580 μm (R) in the endcaps. A charged particle track is expected to cross 8 strips, or four space points, on average.

A significant contribution to charged particle momentum measurements is provided by the 30-40 hits/track expected in the TRT [33]. The TRT only provides R-ϕ tracking information with an intrinsic accuracy of 130 μm, but is also designed to distinguish between electrons and hadrons. The basic elements of the TRT are thin-walled proportional drift tubes, also known as straws, interweaved with radiator material. The straws are 4mm in diameter and contain a Xe:CO_2:O_2=70:27:2 gas mixture surrounding a 30 μm gold-plated tungsten wire [6]. The thin wall of the straw contains a layer of electrically grounded aluminum which acts as the cathode, while the wire is held at a high negative voltage and acts as the readout anode. Charged particles travelling through the straws ionize the gaseous medium and the resulting electrons are accelerated towards the wire causing a further cascade of ionization. The drift time of the ionized electrons towards the wire provides information about the impact parameter of the track parallel to the wire. Electron identification, on the other hand, is achieved through the detection of transition radiation which is emitted when electrons travel between the polypropylene/polyethelene radiator material and the drift tubes. Ultra-relativistic particles emit x-rays when they cross the boundary between materials with different dielectric constants. The intensity of the transition radiation is dependent on the relativistic gamma factor, γ, which is greater for particles of lower mass but identical momentum. When $\gamma > 1000$, significant radiation is produced. For electrons this occurs at a momentum $\sim$1 GeV/c, but for pions it is around a momentum of $\sim$100 GeV/c. The low energy transition radiation photons are absorbed in the Xenon gas mixture and tend to create a larger signal amplitude than

minimum-ionising charged particles. For this reason, there are two thresholds in the TRT ADCs and an ultra-relativistic electron is expected to have ~8 high treshold hits in the TRT. The fraction of high versus low threshold hits is used to distinguish electrons from hadrons, providing a pion rejection factor of ~150. There are 52,544 (73 layers) of 144 cm length straws in the barrel ($|\eta| < 0.7$, $563 < R < 1066$ mm), arranged parallel to the beam. The barrel straws are divided into two halves and are read out at both ends. In the endcaps ($0.7 < |\eta| < 2.0$, $848 < |z| < 2710$ mm), the 37 cm long straws are arranged radially in wheels and consist of 160 straw planes each [32].

6.4   Calorimetry

The main purpose of a calorimeter is to contain and measure energy depositions and direction of electromagnetic and hadronic showers. The calorimeters are also used to analyze the lateral and longitudinal profiles of electromagnetic and hadronic showers. ATLAS uses a set of non-compensating sampling calorimeters utilising different detection mechanisms in order to cope with the wide range of physics processes and radiation environment requirements over the $|\eta| < 4.9$ range. Figure 6.3 and Table 6.1 provide an outline of the basic structure and the main parameters of the calorimeter system in ATLAS. The electromagnetic (EM) calorimeters are 20-40 radiation lengths in depth, which is sufficient to contain electromagnetic showers of up to ~1 TeV and a fraction of the hadronic showers. The hadronic calorimeters are 8-10 interaction lengths thick, and can contain the rest of the hadronic activity. The central hadronic calorimetry uses scintillating tiles as the active medium and steel as the absorber, whereas the rest of the system incorporates a liquid argon active medium with lead, copper or tungsten absorbers.
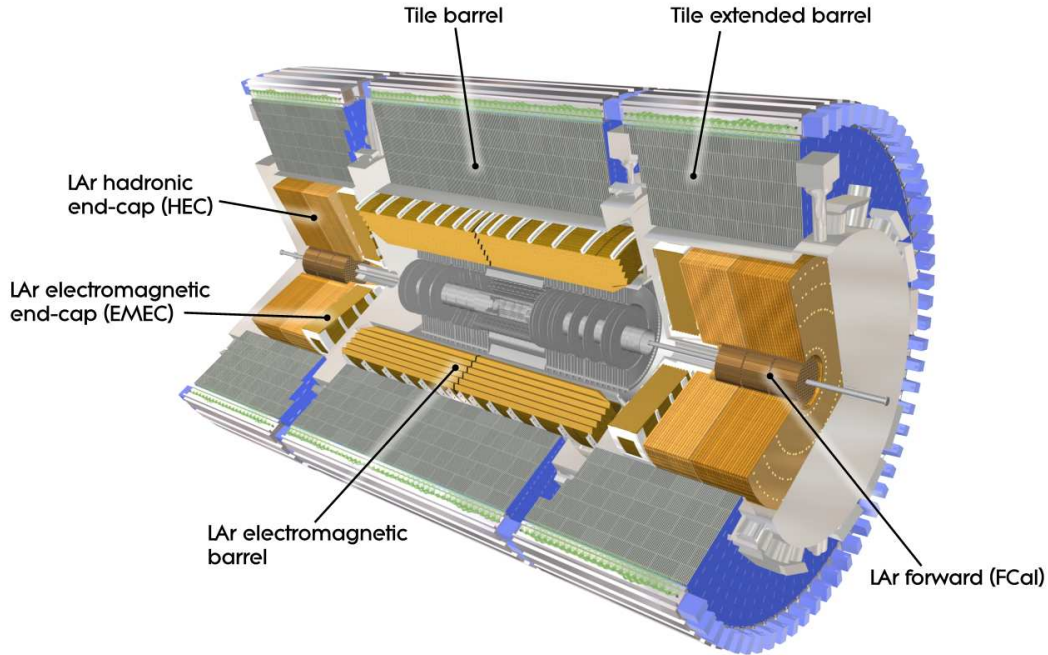
Figure 6.3: *Cut-away view of the ATLAS calorimeter system [32].*

6.4.1 Electromagnetic Calorimeters

The EM calorimeter consists of two half-barrels separated by a 4mm gap at $z = 0$, two end-caps each consisting of two wheels in the region $1.375 < |\eta| < 3.2$ and the first layer of the FCal at $|\eta| < 4.9$. The inner wheel of the endcap is 2 layers in depth and the outer wheel is 3 layers in depth. The region between the barrel and end-cap, $1.37 < |\eta| < 1.52$, is expected to have poorer performance due to the lack of instrumented material and is referred to as the 'crack region'. The EM calorimeter is a sampling calorimeter which utilises lead or copper absorbers and liquid argon as the active material. When particles pass through the LAr, they ionize it. The presence of a high voltage across the active material causes the freed electrons to drift to the anode, thereby inducing a current proportional to the number of freed electrons. Liquid argon was chosen for its stability of response over time, its uniformity, and its radiation-hardness.

In the barrel and end-caps, full azimuthal coverage is achieved through an accordion

Cells in Layer 3
$\Delta\varphi\times\Delta\eta = 0.0245\times0.05$

Trigger Tower
$\Delta\eta = 0.1$

$2X_0$

$\eta = 0$

470 mm

$16X_0$

Trigger
Tower
$\Delta\varphi = 0.0982$

$4.3X_0$

1500 mm

$1.7X_0$
$\Delta\varphi=0.0245x4$
36.8mmx4
=147.3mm

Square cells in
Layer 2

$\Delta\varphi = 0.0245$

φ

37.5mm/8 = 4.69 mm
$\Delta\eta = 0.0031$

$\Delta\eta = 0.025$

Strip cells in Layer 1

η
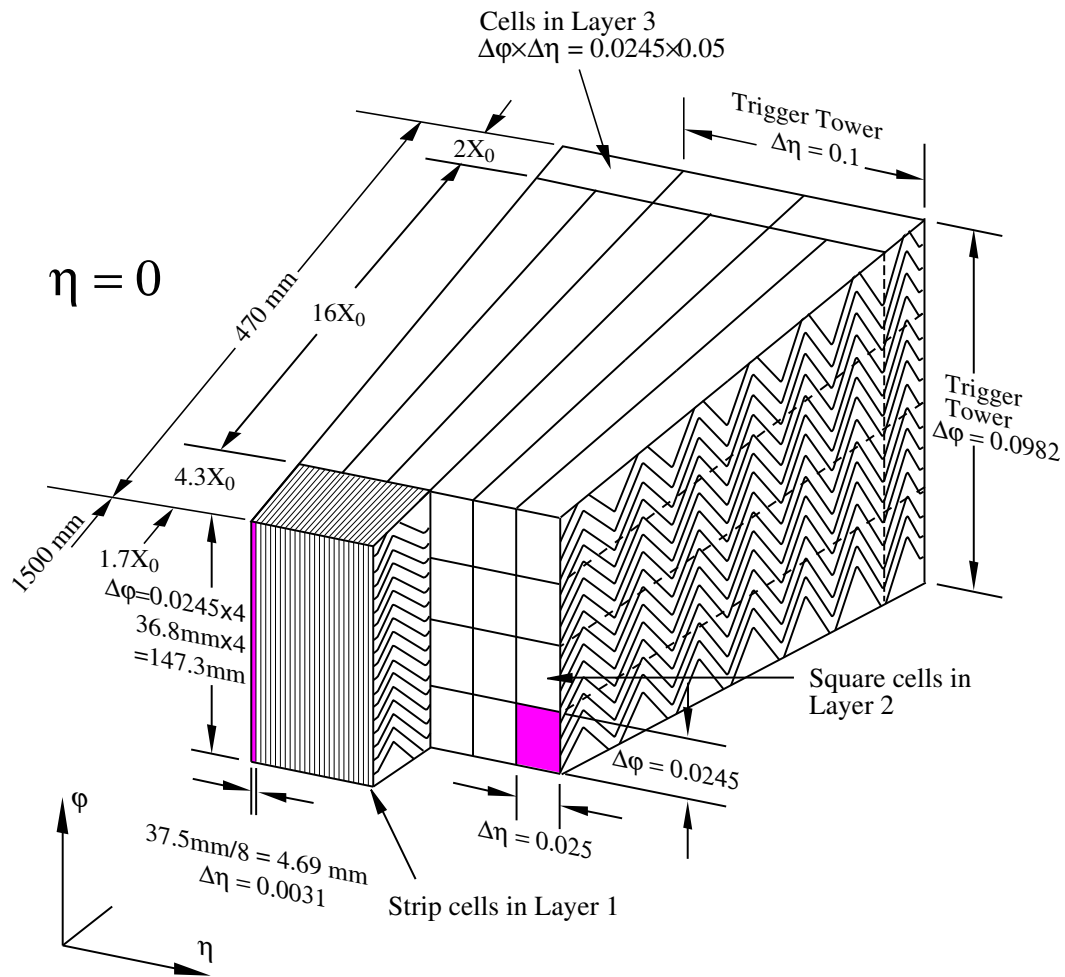
Figure 6.4: *Sketch of a barrel EM Calorimeter module outlining the different layers and granularity in η and ϕ for cells and trigger towers [32]. In this diagram the accordion waves fold radially and run parallel to the beam pipe (in the direction of η).*

geometry depicted in figure 6.4. In the barrel, the accordion waves fold radially and run parallel to the beam pipe, whereas in the endcaps the waves fold parallel to the beam pipe and run in the radial direction. The folding angle of the waves vary in such a way as to keep the liquid argon gap constant. Each subdetector contains three layers except for the inner wheel of the end-cap which contains two layers with coarser granularity because precision measurements only go up to the acceptance of the inner detector at $|\eta| < 2.5$. The first layer closest to the beam pipe, referred to as the strips layer, is finely segmented in η in order to improve $\gamma - \pi^0$ discrimination. The second layer, with its greater thickness in terms of radiation lengths, is designed to capture most of a given electromagnetic shower and the shower shape information in this layer is used to distinguish electromagnetic showers from hadronic ones. The third layer captures the tails of highly energetic electromagnetic showers and is again used to distinguish between elctromagnetic and hadronic deposits which tend to leak into the hadronic calorimeters. Photons or electrons may interact prior to reaching the EM calorimeter. This is because there is approximately 1-4 X_0 of dead material in the inner detectors, the solenoid coil and the cryostat. In order to correct for the energy lost upstream of this extra material, a presampler is placed in the region $|\eta| < 1.8$. The presampler is a layer of liquid argon, 1.1 cm thick in the barrel and 0.5 cm in the end-caps, with a 2 kV potential and electrodes that are finely segmented in η.

The first layer of the FCal is made of copper absorbers and LAr active material. Although it was not sepecifically designed to contain EM showers, it does achieve this task and is discussed in this section. Due to the high radiation dose expected in the forward region, the layout of this subdetector is different from that in the barrel and endcap. It is 45 cm thick, or 27.6 X_0 thick, and consists of a set of stacked copper plates that have 12,260 holes drilled into them. The electrode structure consists of a copper rod, acting as the anode, which is placed within each hole and surrounded by a copper tube, acting as the cathode. Between the copper rods and the tubes is a small 0.269 mm gap

filled with liquid argon. The gap size is maintained by a helically-wound radiation hard plastic fiber. This small LAr gap, compared to $\sim 2mm$ in the barrel, avoids problems due to ion build-up expected for the high particle flux environment of the FCal [29]. Copper has been utilised in the first layer because its Molière radius [2] (17 mm) is large enough to ensure uniform response and for its good heat conduction properties. The second and third layer of the FCal follow the same basic geometry but differ in material content and will be discussed in section 6.4.2.

6.4.2 Hadronic Calorimeters

The hadronic calorimetry system with its coarser granularity is optimised to fully contain and measure hadronic showers and to measure missing transverse energy in conjunction with the electromagnetic calorimeters. It consists of scintillating tile calorimeters in the central region ($|\eta| < 1.7$), hadronic end-cap calorimeters (HEC for $1.5 < |\eta| < 3.2$) and the second and third layers of the forward calorimeters ($3.1 < |\eta| < 4.9$). The Tile calorimeters use steel absorbers and doped polystyrene scintillators to measure hadronic activity, whereas the FCal and the HEC utilise LAr technology.

The Tile calorimeter is composed of 3 cylindrical structures; the barrel covering the region $|\eta| < 1.0$, and two extended barrels in the region $0.8 < |\eta| < 1.7$. The gap region between the barrel and extended barrel is necessary to supply service and contains the power supplies and cables for the inner detectors and barrel EM calorimeter. Each segment of the Tile calorimeter is divided into three layers, approximately 8 interaction lengths deep, and each layer consists of 64 wedges of size $\Delta\phi \sim 0.1$ (see figure 6.5). When charged particles cross the tiles they excite the molecules of the base scintillating material. Approximately 3% of this energy is emitted as photons within a decay time of O(10) ns. Fluors are impurities of complex molecules that are introduced to shift

---

[2]The Molière radius is the radius of a cylinder for a given material which will on average contain 90% of an EM shower.

this scintillating light to a wavelength that can be handled more easily. Because these fluors are formed from complex molecules they can absorb and emit photons in a wide range of energies and can also have the undesirable effect of increasing the likelihood of re-absorption of the emitted light, thus making the tiles less transparent. The Tile calorimeter uses two types of fluors in order to increase the light yield, decrease the decay time and increase the transparency for the transport of the signal to the optical fibres. The main function of the primary fluor, which is present at a 1.5% concentration level, is to increase the light yield and decrease the decay time of the base scintillating material. This is achieved, because at this level of concentration the distance between the base and primary fluor molecules is much smaller than the wavelengths of light emitted. At such small distances, the energy transfer between the two does not require the radiation of a photon, but involves a resonant dipole-dipole interaction which can decrease the decay time by an order of magnitude. This transferred energy is emitted by the primary fluor in the form of UV light. The UV light, however, has a very short attenuation length inside the scintillating tiles due to the high probability of re-absorption. A second fluor is introduced at a smaller concentration of ∼0.04%, which converts UV light to visible light. The tiles are transparent to visible light due to the lower probability of re-absorption, therefore this light travels to the edges of the tile. Two wavelength shifting fibres are placed in contact with each side of the tile which convert the light from the scintillators to longer wavelengths. This shift is necessary in order to attain smaller attenuation while being transported and also because the longer wavelengths of light are necessary for the efficient conversion to an electrical signal by the photomultipliers. The fibres from each side are grouped together and read out into separate photomultiplier tubes. This duplication of readout provides an equalization for signals produced by particles with different impact parameters.

The HEC is a copper-LAr sampling calorimeter located behind the end-cap EM calorimeter and uses a flat plate design. Each end-cap consists of two wheels. The
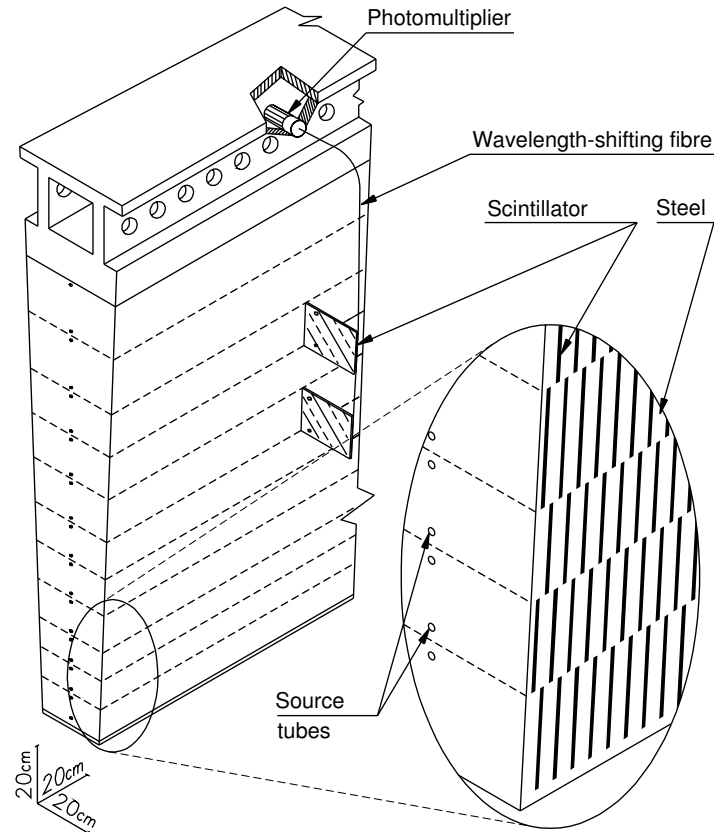
Figure 6.5: *Sketch of a hadronic Tile calorimeter module showing the different components of the optical readout [32].*

wheel closest to the interaction point is referred to as the front wheel and the one further away is called the rear wheel. The wheels are divided into 32 wedges in ϕ. The front wheel modules consist of 24 copper plates with a thickness of 25 mm interleaved with 8.5 mm LAr gaps. The rear wheel modules, on the other hand, contain 16 copper plates that are 50 mm thick. The LAr gaps are divided into four drift zones which are read out by separate electrodes.

The second and third modules of the FCal are very similar in structure to that described for the first layer, but they use tungsten as opposed to copper, and have coarser granularity. Tungsten, though difficult to work with, was used because it reduces the lateral spread of hadronic showers and is effective at containing them longitudinally.

The copper rods of the first layer are, therefore, replaced by tungsten rods and the stacked copper plates are replaced by small tungsten slugs. A copper alloy shielding plug is placed behind the third layer in order to reduce leakage into the end-cap muon system.

6.4.3 Calorimeter Resolution

The estimate of E_T^{miss} used in this analysis, described in section 7.4, is constructed from collections of calorimeter cells called topoclusters that will be described in section 7.4.1. Calorimeters are primarily designed to measure the energy of an incident particle. This measurement relies on the total absorption of the incident particle and its subsequent showering. Even when a shower is fully contained, the calorimeter response to an incident particle of a given energy follows an approximately normal distribution. The width of this response is referred to as the resolution, σ, and can be parameterized as follows [59]:

$$\frac{\sigma}{E} = \frac{a}{\sqrt{E_0}} \oplus \frac{b}{E} \oplus c \tag{6.5}$$

where E is the measured energy of the incident particle, E_0 is the initial energy of the particle, the symbol $\oplus$ refers to quadratic summation, and the constants a, b, and c are known as the stochastic term, noise term and constant term respectively. The stochastic term, a, arises from fluctuations in the shower development. In sampling calorimeters, such as the ones used in ATLAS, these fluctuations are due to variations in the number of charged particles within a given shower that cross the active layers. For hadronic calorimeters, non-compensation effects also play a significant role. The noise term, b, comes from the electronic noise of the readout chain. The constant term, c, includes contributions that are independent of the energy of the incident particle, such as calibration erros, mechanical imperfections etc. For higher incident particle energies, $\frac{\sigma}{E}$ improves and the constant term becomes the dominant contribution. At low incident particle energies, on the other hand, the noise term becomes the dominant contribution since it is energy independent.

The performance goals of the ATLAS calorimeters in terms of energy resolution are outlined in Table 6.2. In this table, the energy resolution requirement for the electromagnetic and hadronic calorimeters are given in terms of the stochastic and constant term. Figure 7.3 shows the noise levels in various regions of the calorimeter. It can be seen that the cell level electronic noise term is around $\leq$500 MeV for the entire η coverage of the ATLAS detector, decreasing to O(10) MeV in the central region.

6.5   Muon System

The ATLAS muon system, depicted in Figure 6.6, covers the region $|\eta| < 2.7$ and is designed to provide precision measurements of muon momenta, from 3 GeV/c to 3 TeV/c, and fast triggering response. Muon trajectories are bent by the large toroidal magnets which provide an independent measurement of a muon's momentum from that obtained by the inner detectors in the solenoid field. High precision tracking is achieved by a combination of monitored drift tube (MDT) chambers and cathode strip chambers (CSC) at high η. Since many interesting physics processes involve muon final states, two independent detection and triggering technologies are designed for rapid response. These technologies include the thin gap chambers (TGCs) in the end-caps and the resistive plate chambers (RPCs) in the central region.

Three superconducting toroid magnets provide the bending power for the muon system. Two end-cap toroids ($1.6 < |\eta| < 2.7$) are inserted in the barrel toroid ($|\eta| < 1.4$). The magnetic field in the region between the two magnets is supplied by a combination of the fields produced by the end-cap and barrel toroids. Each toroid consists of eight coils assembled radially around the beam axis. The three toroids provide a bending power of 1.5 to 5.5 Tm in the central region and 1 to 7.5 Tesla-meters in the end-caps.

Precision momentum measurements are performed by the 3-4 layers of MDT chambers
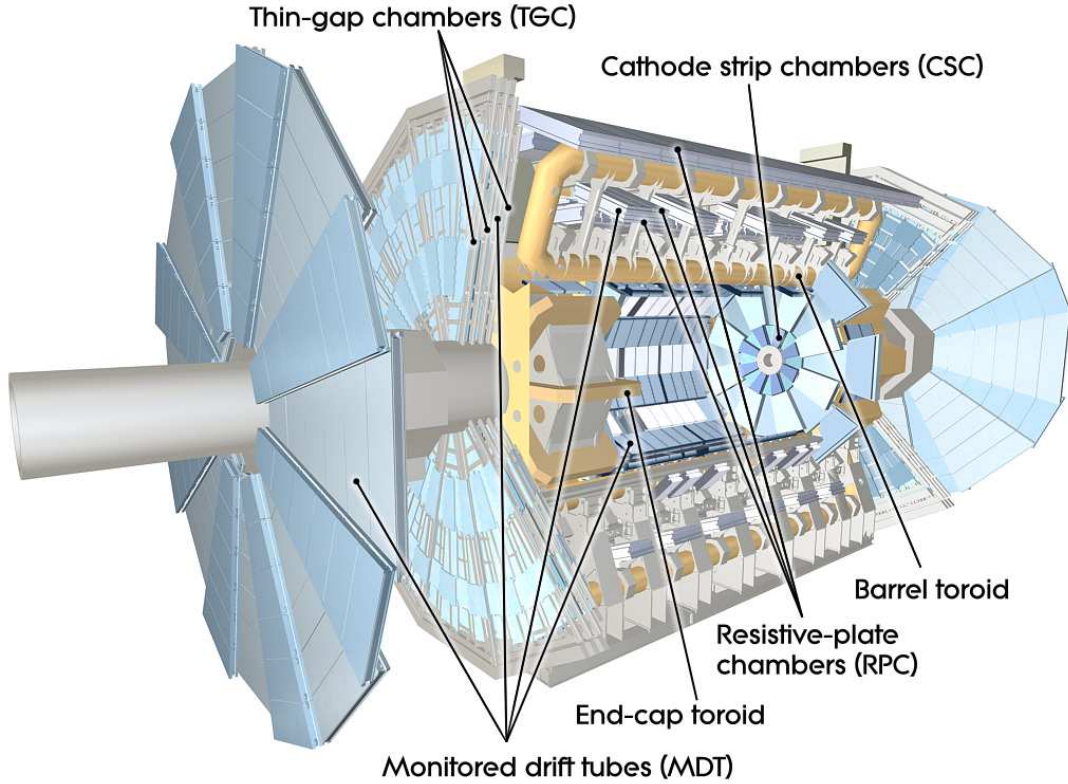
Figure 6.6: *Overview of the ATLAS muon system [32].*

in the pseudorapidity range $|\eta| < 2.7$ [3] and the CSCs in the innermost layer of the end-cap $(2 < |\eta| < 2.7)$. The MDT chambers consist of three to eight layers of drift tubes that are filled with argon, CO_2 and water vapour with an anode wire running down the center where the electrons resulting from ionization are picked up. The chambers are arranged such that the drift tubes run along ϕ in both the barrel and the end-caps and meet the ATLAS momentum resolution criterion of $\Delta p/p \approx 10\%$ for a 1 TeV/c muon track. Due to the high particle fluxes and muon track densities expected in the forward region, CSCs which are multiwire proportional chambers, are used in the innermost layer of the end-caps. There are 16 cathode strip chambers in each end-cap. Each chamber contains four regions of argon and CO_2 gas with anode wires running in the radial direction. The

---

[3]In the innermost layer of the endcap, the pseudorapidity range is for $|\eta| < 2.0$.

signal is read out from the cathode strips on either side of the anode wires and gas layers. The strips are oriented radially (parallel to the wires) on one side and perpendicular to the wires on the other side, thereby measuring the tracks in both η and ϕ.

The precision tracking chambers are complemented by two types of fast trigger chambers extending out to $|\eta| < 2.4$. They are capable of delivering tracking information within a few tens of nanoseconds. The RPC services the central region ($|\eta| < 1.05$), while the TGC has been chosen for the end-cap region ($1.05 < |\eta| < 2.4$). The RPC consists of a 2 mm layer of gas in between a cathode and an anode plate. The read-out strips are oriented in both the η and ϕ directions and the chambers are arranged in three double-layers in the central region. The TGC operates on the same principle as a multi-wire proportional chamber but has the unique characteristic of having a smaller wire-to-cathode distance (1.4 mm) than wire-to-wire distance (1.8 mm). This geometry allows for operation in a high particle flux environment where some level of saturation may be expected. Furthermore, both the RPC and TGC measurement in the non-bending (ϕ) direction are used to complement the MDT's muon track measurement.

6.6   Trigger

At design luminosity, the proton beams cross at an expected rate of 40 MHz. Without any filtering, and considering the fact that the ATLAS detector contains ~200 million channels, O(10) terabytes of data would need to be processed and recorded every second. The rate at which ATLAS can record events is limited by its ability to transfer information to CERN's Tier0 computing system, where the data is processed and stored. Output bandwidth limitations require that this interaction rate be reduced to 200 Hz. Furthermore, it takes a certain amount of time to read out a given event. During this time the detector cannot record another event. This is known as "dead time". The background event rate in ATLAS is much larger than the rate for processes of interest. If all events

were recorded, the detector would always be dead. The expected rate for many physics processes of interest is far below the 200 Hz level. For example, a typical universal extra dimension signal is expected at a rate of $\sim$0.001 to 1 Hz. Therefore, it is neither possible nor necessary to record the information for all events. This implies that a fast decision must be made with respect to each event in order to determine whether it contains any interesting signatures and all rejected events will be lost. To make a "zero dead time" trigger, all incoming events are recorded in a pipeline memory for each detector channel. To save money only short time slices are recorded. The amount of time it would take to make a decision about whether the first event in the time slice should be kept or not defines how sophisticated the first level trigger can be. Since the first level trigger has to make a decision in a very short time, it does not eliminate all the background. This implies that the second and third level triggers can be more sophisticated and can take a longer amount of time to process the remaining events. The rates of interesting events to background are further enriched in this process.

The total cross section for inelastic p-p collisions is $\sim$80 mb at 14 TeV. However, most of these interactions are from minimum bias events with a cross section of $\sim$70 mb, which are described by soft partonic interactions with large impact parameters and small momentum transfers. Most of the final state particles from these types of interactions will either escape down the beam pipe or have low p_T. However, a few particles may still have high enough p_T and will be detected by ATLAS. Hard scattering collisions, in which the impact parameters are small and the momentum transfers are large, have much smaller cross sections but are more characteristic of new physics processes. Such events are characterized by event topologies containing high p_T particles and jets and/or large E_T^{miss} that also distinguish them from minimum bias events. The ATLAS trigger system is designed to identify these hard scattering events for precision measurements and searches for new physics. It uses a three level triggering system which incorporates a higher detector granularity, precision and a larger fraction of the detector at each

successive level. A further reduction in the data rate is achieved by only reading out channels that have a signal above some threshold.

The first level of the triggering system (L1) corresponds to a data recording rate of 75 kHz and is based on coarse hardware-based detector information and fast decision making capability of less than $2.5 \mu s$. It is designed to pick out events with large E_T^{miss} and total transverse energy and those containing high p_T muons, electrons/photons, jets and hadronically decaying τ-leptons. It does not use any information from the inner detectors, and utilizes only reduced granularity information from the muon and calorimeter systems. The information from the calorimeters is based on energy deposition in trigger towers of size $\Delta\eta \times \Delta\phi = 0.1 \times 0.1$, for example. The L1 decision needs to be made fast because while being formed, the information for all detector channels is retained in pipeline memories that are placed on or near the detector where the radiation levels are high and access is difficult. Therefore, it is desirable to have shorter pipelines which limit the L1 latency and save money.

Once the L1 decision is made, the information from the front ends is read out to the on-site buffers located on the side of the ATLAS cavern where the radiation levels are low. The L1 trigger also defines Regions-of-Interest (ROIs) and passes the information about identified features and passed thresholds to the higher level triggers (HLT). The L2 trigger uses the full granularity and precision of the detector to further asses the ROI's provided by the L1 trigger. The L2 trigger system makes a decision in 40 ms and reduces the output rate to 3.5 kHz. It improves the selection criterion in the ROI by applying better calibrations, using tracking information to distinguish electrons from photons and refining missing transverse energy measurements by including muons, for example.

The final reduction to an event recording rate of 200 Hz is carried out by the event filter (EF). The EF has an average event processing time of ~4 seconds and utilises offline reconstruction algorithms on the full event to complete the trigger processing. The events that pass the EF are then transferred to Tier0, where the full offline event reconstruction

is run. Here a detailed detector description as well as conditions and configurations of the beam, the magnets, all sub-detectors etc. are used to correlate hits in the detector with reconstructed particles. This output is saved for distribution to computing centers around the world.

Various trigger chains are used to make a decision on whether or not to record an event. At high luminosities, some of the trigger chains may have too high a rate and are, therefore, prescaled; only a certain fraction of the events that satisfy the trigger are actually recorded. The trigger used for this analysis was not prescaled and is further described in section 8.1.

Table 6.1: *Main parameters of the calorimeter system [32].*

Subdetector	Layer	Granularity $\Delta\eta \times \Delta\phi$ $\Delta x \times \Delta y$ cm (for FCAL)	η Range
EM Barrel	Presampler	0.025×0.1	$|\eta| < 1.52$
	Layer 1	$0.025/8 \times 0.1$	$|\eta| < 1.40$
		0.025×0.025	$1.40 < |\eta| < 1.475$
	Layer 2	0.025×0.025	$|\eta| < 1.40$
		0.075×0.025	$1.40 < |\eta| < 1.475$
	Layer 3	0.050×0.025	$|\eta| < 1.35$
EM End-cap	Presampler	0.025×0.1	$1.5 < |\eta| < 1.8$
	Layer 1	0.050×0.1	$1.375 < |\eta| < 1.425$
		0.025×0.1	$1.425 < |\eta| < 1.5$
		$0.025/8 \times 0.1$	$1.5 < |\eta| < 1.8$
		$0.025/6 \times 0.1$	$1.8 < |\eta| < 2.0$
		$0.025/4 \times 0.1$	$2.0 < |\eta| < 2.4$
		0.025×0.1	$2.4 < |\eta| < 2.5$
	Layer 2	0.050×0.025	$1.375 < |\eta| < 1.425$
		0.025×0.025	$1.425 < |\eta| < 2.5$
		0.1×0.1	$2.5 < |\eta| < 3.2$
	Layer 3	0.050×0.025	$1.5 < |\eta| < 2.5$
Hadronic End-cap	All 4 layers	0.1×0.1	$1.5 < |\eta| < 2.5$
		0.2×0.2	$2.5 < |\eta| < 3.2$
Forward Calorimeter	Layer 1	3.0×2.6	$1.5 < |\eta| < 2.5$
		$\sim 4\times$ finer	$3.10 < |\eta| < 3.15$
			$4.30 < |\eta| < 4.83$
	Layer 2	3.3×4.2	$3.24 < |\eta| < 4.50$
		$\sim 4\times$ finer	$3.20 < |\eta| < 3.24$
			$4.50 < |\eta| < 4.81$
	Layer 3	5.4×4.7	$3.32 < |\eta| < 4.60$
		$\sim 4\times$ finer	$3.29 < |\eta| < 3.32$
			$4.60 < |\eta| < 4.75$
Tile Barrel	Layers 1 & 2	0.1×0.1	$|\eta| < 1.0$
	Layer 3	0.2×0.1	$|\eta| < 1.0$
Tile Extended Barrel	Layers 1 & 2	0.1×0.1	$0.8 < |\eta| < 1.7$
	Layer 3	0.2×0.1	$0.8 < |\eta| < 1.7$

Calorimeter Component	Required Resolution	η Coverage
EM Calorimetry	$\frac{\sigma}{E} = \frac{10\%}{\sqrt{E}} \oplus 0.7\%$	± 3.2
Hadronic Calorimetry (jets)		
Barrel and End-cap	$\frac{\sigma}{E} = \frac{50\%}{\sqrt{E}} \oplus 3\%$	± 3.2
Forward	$\frac{\sigma}{E} = \frac{100\%}{\sqrt{E}} \oplus 10\%$	$3.1 < |\eta| < 4.9$

Table 6.2: *The required performance of the ATLAS calorimeters in terms of resolution. The units of E are in GeV [32].*

Chapter 7

Particle Identification

The universal extra dimension model under investigation in this analysis gives rise to a final state consisting of two high p_T photons and large missing transverse energy. In this section the basic properties, the particle identification procedure and measurement of photons and missing transverse energy will be discussed. The identification of photons in the ATLAS detector depends on the basic properties that distinguish electromagnetic showers, induced by photons, from hadronic showers. Section 7.1 briefly reviews the characteristics of electromagnetic showers, followed by a description of hadronic showers in section 7.2. The reconstruction and identification of photon candidates is reviewed in section 7.3 followed by a description of the missing transverse energy variable in section 7.4.

7.1   Electromagnetic Showers

7.1.1   Shower Development

The identification of high energy, E> 20 GeV, photons and the ability to distinguish them from hadronic activity in the ATLAS detector depends on the signature expected for these objects [59] [45] [81]. Photons can interact with matter in a wide variety

of processes as seen in figure 7.1, however at energies above ~10 MeV, the dominant process is the interaction with the electric field of the atoms in the traversed material resulting in the production of an electron and positron pair. High energy $e^{\pm}$, on the other hand, tend to predominantly lose their energy through bremsstrahlung, the process in which the electron or positron interacts with the electric field of an atomic nucleus in the traversed material and subsequently emits a photon. However, as can be seen in figure 7.2, ionization energy loss is also still at play. A cascade of pair production and bremsstrahlung activity is, therefore, initiated by a high energy photon which leads to electrons, positrons and photons of lower and lower energies. This cascade of interactions is an electromagnetic shower, which can be generated by either a high energy photon or electron. When the energy of the resulting electrons and positrons is low enough, less than ~10-100 MeV, ionization energy loss dominates for these particles. At the end of the chain, a low energy electron is eventually absorbed by an ion and the positron annihilates with an electron producing two photons with energies > 511 KeV each. Low energy photons in the electromagnetic cascade lose their energy in a sequence of compton scattering processes ending with photoelectric absorbtion. The currents collected in the EM calorimeters result from the ionization of the liquid argon layers by the $e^{\pm}$ and γ particles of EM showers.

7.1.2   Longitudinal Shower Profile

A radiation length (X_0) is the characteristic length scale associated with EM showers. It is the mean distance an electron or a positron travels before losing $\frac{1}{e}$ of its energy through bremsstrahlung, but alternatively, it can also be defined as $\frac{7}{9}$ of the mean free path for pair production for a high energy photon. A fit to experimental data gives rise to the following approximation,

$$X_0 = \frac{716A}{Z(Z+1)\ln(287/\sqrt{Z})} \text{ g cm}^{-2},\qquad(7.1)$$
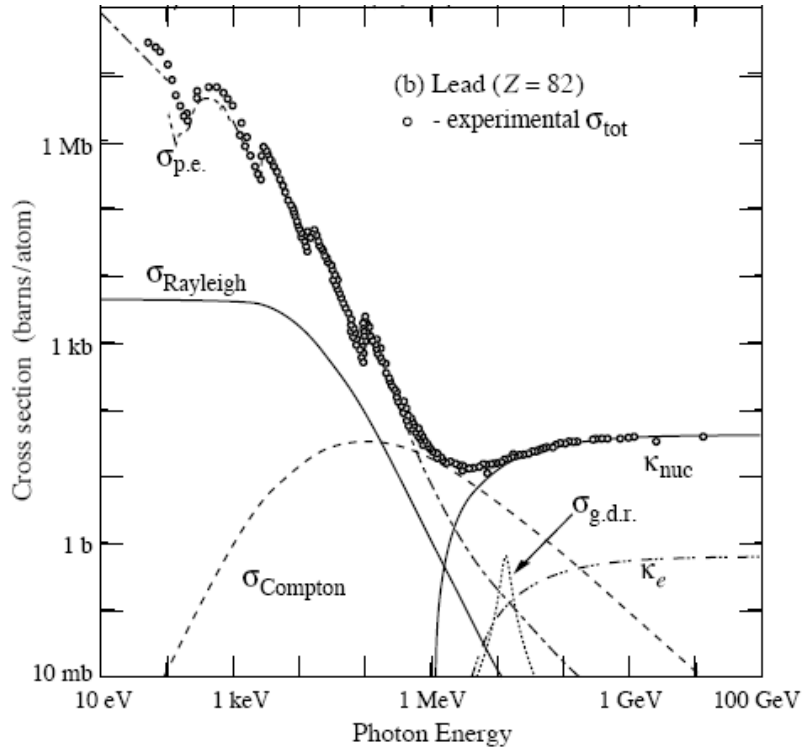
Figure 7.1: *The contribution of different processes and the corresponding cross-sections for the interaction of photons in lead. In this figure, $\sigma_{p.e.}$ refers to the atomic photoelectric effect, $\sigma_{Rayleigh}$ and $\sigma_{Compton}$ refer to Rayleigh and Compton scattering respectively, κ_{nuc} and κ_e respectively refer to pair production in the nuclear electromagnetic field and the fields of atomic electrons of a lead absorber, and $\sigma_{g.d.r}$ refers to photonuclear interactions where the target nucleus is broken up [45].*

where A is the atomic weight and Z is the atomic number. Therefore, materials with higher Z^2 values would have a shorter radiation length. An electromagnetic shower maximum for photons, or the depth at which the largest number of secondary particles is produced, is approximated by,

$$t_{max} \approx \ln(\frac{E_0}{\epsilon_c}) + 0.5, \tag{7.2}$$

where t_{max} is measured in radiation lengths, E_0 is the energy of the incident photon, and ϵ_c is the critical energy at which ionization energy loss per radiation length for an
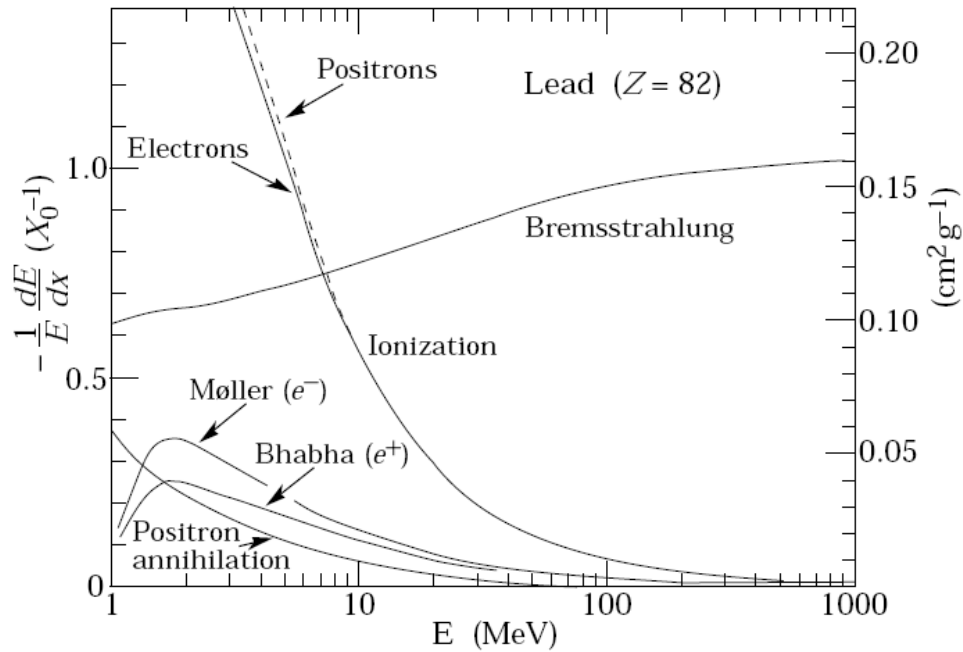
Figure 7.2: *Fractional energy loss per radiation length in lead as a function of electron or positron energy [45].*

electron or positron equals its energy. For solids and liquids, the critical energy is given by,

$$\epsilon_c = \frac{610 MeV}{Z + 1.24}. \tag{7.3}$$

Equation 7.2 shows that the shower length scales logarithmically with energy, therefore, an EM calorimeter thickness needs to also only scale logarithmically with energy. The shower maximum in lead, for example, occurs at around 8(13) X_0 for a 30 GeV(1 TeV) photon, which corresponds to the thickness of the second layer of the EM calorimeter. The calorimeter thickness (in X_0) containing 95% of the shower energy is given by:

$$t_{95\%} \approx t_{max} + 0.08Z + 9.6. \tag{7.4}$$

This implies that approximately $25X_0$ of lead are required to contain 95% of an electromagnetic shower for a 300 GeV photon. The EM calorimeters are, therefore, very efficient at containing most of the electromagnetic shower of high energy photons. Equations 7.2

and 7.4 show that as Z increases, the shower has a longer tail and the maximum shifts to greater depth in radiation lengths. Equation 7.3 also shows that the critical energy, ϵ_c, is lower for materials with higher values of Z.

7.1.3   Lateral Shower Profile

The spread of an electromagnetic shower transverse to the shower axis is caused by two types of effects. During the early stages of shower develpment, multiple scattering of $e^{\pm}$ particles is the dominant cause for the shower's lateral spread. At this stage, electrons and positrons mainly lose their energy through bremsstrahlung where they radiate a photon. The radiation of a photon causes a change in the direction of these particles which is dependent on the strength of the Coulomb field or the atomic number, Z, of the absorber material. After the shower maximum, the dominant process that leads to the lateral spread of the shower are isotropic processes, such as Compton scattering or the photoelectric effect, that produce photons and electrons with larger deviations from the shower axis than the first stage. The radial profile of an electromagnetic shower, therefore, consists of a narrow central core that broadens after the shower maximum. The transverse development of an electromagnetic shower is described by the Molière radius, R_M:

$$R_M = 21.2 \text{ MeV } \frac{X_0}{\epsilon_c}. \tag{7.5}$$

The Molière radius can be defined as the radius of the cylinder which would contain approximately 90% of the energy of an electromagnetic shower. From 7.1 and 7.3, it can be seen that the Molière radius of an electromagnetic shower has a very small dependence on the Z value of the absorbing materials used in the ATLAS detector (e.g. $R_M = 16$ mm for lead and 15.2 mm for copper) and the energy of the incoming particle. These characteristics motivate the use of a fixed size calorimeter window used to seed the photon reconstruction and identification algorithms in ATLAS.

7.2   Hadronic Showers

7.2.1   Shower Development

Hadronic shower development is in many ways similar to EM activity, in that a hadron will undergo a series of interactions with the absorbing medium that results in a cascade of particle multiplications that will reach a maximum peak after which multiplication is balanced by the absorption of shower particles. Hadronic activity is, however, also fundamentally more complicated than EM activity because hadrons can interact with the traversed medium through both electromagnetic and strong interactions. A certain fraction of the energy dissipated in a hadronic shower is undetectable and referred to as invisible energy.

When a charged high energy hadron enters a detector, it can interact electromagnetically by ionizing the traversed medium. The EM interaction of high energy hadrons is similar to muons, in that they are minimum ionizing particles. However, both charged and neutral hadrons can also interact strongly with the nuclei of the absorbing medium which can cause them to shower hadronically. The momenta of these hadronic shower products are typically approximately the same as that of the primary hadron momentum. Furthermore, they can also cause the nuclei in the traversed material to break apart and/or become excited. The de-excitation of the nucleon is achieved by evaporating a certain number of free nucleons or α's until the excitation energy is less than the binding energy. These nucleons generally have energies in the MeV range. The remaining de-excitation occurs via the relaease of γ rays. The resulting hadronic shower particles can then interact in a similar manner. A fraction of the particles produced in this cascade will, furthermore, decay electromagnetically (e.g. $\pi^0, \eta \to \gamma\gamma$) after which their decay products will produce an electromagnetic shower as described in section 7.1. The dissipated energy that is measured in the ATLAS detector is, therefore, a combination of the ionization energy loss involving charged hadrons and the detection of the EM shower

activity from the decay of light neutral mesons such as π^0's and η's. The invisible energy in hadronic showers, on the other hand, arises from the decay of hadrons to muons and neutrinos which escape full detection, nuclear binding energy losses and contributions from the photons and soft neutrons coming from nuclear reactions. A photon from a nuclear reaction can escape detection because a fraction of the photons emitted in nuclear de-excitations are associated with considerable time delays. Soft neutrons lose their energy predominantly through elastic scattering with the nuclei of the absorbing medium in which a fraction of their kinetic energy is transferred to the nucleons. This fraction depends on the medium being traversed. In LAr, for example, only 5% of the neutron's kinetic energy is transferred which will be mainly undetected. The fraction of hadronic versus electromagnetic shower activity, F_h, follows a power-law dependence and tends to decrease as the energy of the incident hadron increases. The values of F_h are in the order of 0.5 (0.3) for a 100 (1000) GeV shower.

7.2.2 Longitudinal Shower Profile

The basic longitudinal profile of a hadronic shower is similar to that of an EM shower, however, the scale that parameterizes its profile, an interaction length λ, is significantly longer. The interaction length is the average distance a high energy hadron will travel before undergoing a strong interaction. It is typically O(10) times larger than the radiation length characterizing EM showers but much less dependent on the atomic number of the absorbing material. It, therefore, takes much more material to contain a hadronic shower versus an EM shower.

7.2.3 Lateral Shower Profile

Hadronic showers are typically much broader than electromagnetic showers. They are characterized by a narrow core, representing the electromagnetic component of the shower, surrounded by a broader halo with an exponentially decreasing intensity, representing the

non-electromagnetic component of the shower. The electromagnetic core arises mainly from π^0 decay into photons which tend to remain close to the shower axis. The non-electromagnetic core is mainly caused by the soft neutrons that are emitted isotropically in all directions during the de-excitation of a nucleus in the absorbing material. The average radius of the cylinder necessary to contain 95% of the energy of a hadronic shower is typically O(10) times larger than the Molière radius associated with an EM shower induced by an EM object with the same initial energy. However, unlike EM showers that have a Molière radius independent of the initial energy of the showering particle, hadronic showers tend to get narrower as the energy of the incident hadron increases. This property is due to the increase in the electromagnetic activity as the incident hadron energy is increased and the concentration of electromagnetic activity near the shower axis.

7.3   Photon Reconstruction and Identification

The association of signals collected in the ATLAS detector with particles is typically done in two steps. In the first step, known as reconstruction, the particle candidates are selected using a set of relaxed criterion aimed at having a high efficiency for selecting the particles of interest at the cost of having a small rejection factor against fakes. The reconstructed particles often have large overlaps, which are removed during a given physics analysis in the second stage of association, known as identification. The rigorousness of the identification step is analysis dependent. There are currently two sets of recommended photon identification criterion in ATLAS. The 'loose' selection has a high efficiency for selecting photons, but a lower rejection ability against hadronic jets which may fake a photon; the 'tight' selection has a lower efficiency but provides a more pure sample of photons. In this section, the photon reconstruction algorithm is briefly described followed by a summary of the 'loose' and 'tight' photon identification criteria.

7.3.1 Photon Reconstruction

The reconstruction of photon candidates is initially intertwined with that of electrons [54] [39] [46]. The first step in the reconstruction process involves finding and identifying pre-clusters of EM calorimeter cells. These pre-clusters are then categorized as either a photon and/or an electron candidate, a procedure referred to as "egamma identification". After this identification is completed, the optimal clusters of calorimeter cells for each particle type are filled and the resulting cluster energies are calibrated. In order to reduce the large number of fakes from hadronic jets, an additional cut on the transverse energy deposited just behind the egamma cluster in the first layer of the hadronic calorimeter is applied. This cut requires that $E_{T_{had1}}/E_T < 0.2$; where $E_{T_{had1}}$ is the transverse energy deposited in the first layer of the hadronic calorimeter lying just behind the egamma cluster and E_T is the transverse energy of the electromagnetic cluster.

Electromagnetic pre-clusters which are used to seed the photon reconstruction algorithm are identified by initially dividing the EM barrel and EM end-cap calorimeters into a grid of projective towers in η and ϕ. The grid only goes up to the acceptance of the inner detector tracking system, $|\eta| < 2.5$, and consists of 200×256 ($N_\eta \times N_\phi$) sections of size 0.025×0.025 ($\Delta\eta \times \Delta\phi$). The energy in each tower is then computed by summing over the energy contribution from all the cells belonging to a given grid element. As can be seen from table 6.1, the granularity of some of the layers in the EM calorimeters is at times coarser than this tower size. In such a scenario, where a calorimeter cell is shared between several neighbouring towers, the energy contribution from that cell to the tower is computed by scaling its energy by the fractional area intersected. To find a pre-cluster, a fixed window of size 5×5 (in units of tower size) is moved across the grid until a local transverse energy maximum is found with $E_T^{threshold}$ of $3 GeV. The use of a fixed window size for electromagnetic particles is optimal because the Moliere radius asso$

The egamma identification procedure separates out pre-clusters into photon and electron candidates. The main difference between an electron and a photon is that electrons

leave a track in the inner detector. However, it is also possible for a photon to leave tracks if it converts to an e$^\pm$ pair while inside the inner detector. The egamma identification procedure, therefore, begins by associating and matching an ordered set of tracks and inner detector conversion vertices to each pre-cluster. The tracks are required to not have a B-layer hit in the pixel detector. Conversion vertices come in two varieties; single-track and double-track. Single-track conversion vertices can arise if one of the tracks is very soft or if the photon converts late in the inner detector into a pair of high p_T e$^\pm$ pair and it is not possible to resolve the two tracks, in which case, the first hit in the inner detector is taken as the conversion vertex. If there are no tracks associated with a given pre-cluster or if the associated best matched track has $p_T < 2$ GeV and consists of TRT hits only, then it is labeled as an unconverted photon. The rest of the pre-clusters are then associated to electron candidates, but a converted photon recovery procedure is also put in place. Converted photons are recovered from the electron candidate collection by comparing the best matched track to the track(s) associated with the best conversion vertex candidate. If the tracks coincide, then the electron candidate is also considered as a converted photon candidate. For pre-clusters associated with double-track conversion vertices, this recovery only takes place if the track has no B-layer hits or if both the tracks belonging to the conversion vertex have B-layer hits. Even if no matching is made between the conversion tracks and the best matched track, an electron candidate can still be labeled as a converted photon if it has a conversion track p_T greater or equal to its best matched track p_T. Electrons with no vertex candidates are, furthermore, considered as converted photons if the associated track is made only of TRT hits, has $p_T > 2$ GeV, and $E/p < 10$, where E is the pre-cluster energy and p is the momentum of the best matched track. Finally, a small number of unconverted photons with erroneous track association could potentially still exist in the electron collection. In order to recover these unconverted photons, any electron that has a best matched track $p_T < 2$ GeV and $E/p > 10$ will automatically also be labeled as an unconverted photon.

Table 7.1: *Cluster size, $N_\eta^{cluster} \times N_\phi^{cluster}$, for different particle types [54].*

Particle Type	Barrel	End-cap
Electrons	3×7	5×5
Converted Photons	3×7	5×5
Unconverted Photons	3×5	5×5

The photon collection at this point consists of those labeled as uncoverted and con-verted photons. The final cluster window size is then optimized depending on the hypoth-esized particle type and the location in the calorimeter as summarized in table 7.1. This optimization is based on a compromise between limiting the effect of noise, which is best achieved with smaller clusters, and containing most of the shower energy, best achieved with larger clusters. The window size for electrons and converted photons, which contain $e^\pm$ pairs, is larger in the ϕ direction for the barrel because electrons interact more with upstream material, can emit bremsstrahlung photons and are bent in the ϕ direction due to the solenoid magnetic field. In the end-caps the window size is the same for all particles because the effect of the magnetic field is smaller and the larger window size in η is due to the smaller physical size in this region. Converted and unconverted photons are treated differently in the energy calibration process, where the cluster energy is corrected for η and ϕ modulations of the detector response, leakage outside cluster window, and potential losses of energy in the crack region. With this procedure more than 97.8% of all photons with $p_T > 20$ GeV are included in the reconstructed photon container.

7.3.2   Photon Identification

QCD jets are the largest background to isolated photons. The photon identification procedure, based on a set of rectangular cuts on calorimetry information, is developed to reduce this fake rate. Cuts on the level of shower leakage into the hadronic calorimeters, the lateral shower shape in the second layer of the electromagnetic calorimeters and the

shower shape variables in the strip layer of the electromagnetic calorimeter are used which are designed to reject hadronic jets with π^0's, η's etc. The variables used in this procedure are defined below:

- **Hadronic Leakage** - These variables are used to reject hadronic jets with high energy pions interacting in the electromagnetic calorimeter, which are on average not entirely contained in the electromagnetic calorimeters and tend to deposit a large fraction of their energy in the hadronic calorimters.

    $\boldsymbol{R}_{had1}$ The amount of transverse energy deposited in the first layer of the hadronic calorimeters behind the electromagnetic cluster, E_T^{had1}, divided by the transverse energy of the photon candidate, E_T.

    $$R_{had1} = \frac{E_T^{had1}}{E_T} \tag{7.6}$$

    $\boldsymbol{R}_{had}$ The amount of transverse energy deposited in the hadronic calorimeter behind the electromagnetic cluster, E_T^{had}, divided by the transverse energy of the photon candidate, E_T.

    $$R_{had} = \frac{E_T^{had}}{E_T} \tag{7.7}$$

- **Shower Shape in the Second Layer of the EM Calorimeters** - Electromagnetic showers deposit most of their energy in the second layer of the EM calorimeters, therefore, the lateral shower profile in this layer provides a good estimate of the shower shape. Hadronic showers tend to be much more spread out laterally and can be distinguished from electromagnetic showers by cutting on the lateral spread of the deposited shower energy. These variables will, therefore, reject hadronic jets with a wide lateral shower profile.

    $\boldsymbol{R}_\eta$ The middle η energy ratio measures the shower's lateral spread in η. It is defined as the ratio of the energy in 3×7, $E_{3\times7}^{S2}$, to 7×7, $E_{7\times7}^{S2}$, cells $(\eta \times \phi)$

in the second layer of the electromagnetic calorimeters and centered around the cluster seed.

$$R_\eta = \frac{E_{3\times7}^{S2}}{E_{7\times7}^{S2}} \tag{7.8}$$

$\boldsymbol{R_\phi}$ The middle ϕ ratio is a measure of the shower's lateral spread in the ϕ direction. Due to the presence of the solenoid magnetic field in the inner detectors, it behaves differently for converted versus unconverted photons because the e$^+$ and e$^-$ of a converted photon bend in opposite directions in ϕ resulting in a more spread out shower in this direction. This variable is defined as the ratio of the energy in 3×3 to 3×7 cells ($\eta \times \phi$) in the second layer of the electromagnetic calorimeter and centered around the cluster seed.

$$R_\phi = \frac{E_{3\times3}^{S2}}{E_{3\times7}^{S2}} \tag{7.9}$$

$\boldsymbol{w_2}$ The lateral shower width measures the shower's energy weighted width in η using all cells in a 3×5 ($\eta \times \phi$) window centered around the cluster seed.

$$w_2 = \sqrt{\frac{\sum E_i \eta_i^2}{\sum E_i} - (\frac{\sum E_i \eta_i}{\sum E_i})^2} \tag{7.10}$$

- **Shower Shape in the Strip Layer of the EM Calorimeters** - The variables above will reject jets with high energy pions and wide lateral shower profiles. The strip layer of the EM Calorimeter, with its finer granularity in η, provides a good separation between isolated photons and hadronic jets with isolated leading π^0's, which decay to two photons. These types of hadronic showers would be wider than a photon-induced electromagnetic shower and would contain two separate energy peaks in their shower profile.

$\boldsymbol{F_{side}}$ The Front side energy ratio measures the containment of the shower around the cell with the largest energy deposit.

$$F_{side} = \frac{E(\pm3) - E(\pm1)}{E_{\pm1}} \tag{7.11}$$

Where E($\pm$n) is the amount of energy in $\pm$n strip cells around the strip with the largest energy.

w_{s3} The front lateral width (3 strips) measures the width of the shower using ± 2 strip cells about the strip with the largest energy deposit.

$$w_{s3} = \sqrt{\frac{\sum E_i \times (i - i_{max})^2}{\sum E_i}} \qquad (7.12)$$

Where i_{max} labels the strip cell with the largest energy deposit and i labels the four strip cells on either side of i_{max}.

w_{stotal} The front lateral width (total) measures the width of the shower using approximately 20 strip cells in η and 2 strip cells in ϕ about the cell with the largest energy deposit and is calculated as above.

ΔE The 'front second maximum difference' looks at the difference between the energy in the strip cell with the second largest energy deposition $E_{2^{nd}max}$, and the strip cells with the smallest energy deposition lying between the cells with the largest and the second largest energy, E_{min}.

$$\Delta E = E_{2^{nd}max} - E_{min} \qquad (7.13)$$

E_{ratio} The front maxima relative ratio measures the relative difference between the two strip cells with the largest energy.

$$E_{ratio} = \frac{E_{1^{st}max} - E_{2^{nd}max}}{E_{1^{st}max} + E_{2^{nd}max}} \qquad (7.14)$$

The discriminating variables used for identifying a "Loose" or "Tight" photon are outlined in table 7.2. The "Loose" photon identification criterion is based on discriminating variables involving shower leakage into the hadronic calorimeters and the shower shape in the second layer of the electromagnetic calorimeter. The cut thresholds are in common with those applied to "Loose" electrons, make no distinction between converted and unconverted photons and are optimized for nine different $|\eta|$ regions. The variables

associated with the strip layers are not included in the "Loose" selection because this selection was required to be robust enough to be used for trigger purposes for the early period of LHC data taking. The sensitivity of the strip layer variables to cross-talk between neighbouring cells and the amount of dead material before the calorimeters makes them a poor option for the "Loose" photon selection. From Monte Carlo studies the "Loose" identification criteria are expected to have an average identification efficiency of 96% with respect to reconstructed photons and only 1 in 1000 hadronic jets will pass this selection criterion. The "Tight" photon identification is expected to have an average efficiency of 89% and 1 in 5000 hadronic jets are expected to pass its set of cuts. Since, the "Tight" selection includes cuts on all the discriminating variables, including the strip layer ones, it also includes an η cut based on the acceptance of the strip layers. These cuts are optimized for converted and unconverted photons in seven different $|\eta|$ regions.

Table 7.2: *A summary of the discriminating variables used for the "Loose" and "Tight" photon identification [39].*

Category	Discriminating Variable	Loose	Tight
Acceptance	$1.37 < |\eta| < 1.52$, $|\eta| > 2.37$ excluded	-	X
Hadronic Leakage	R_{had1}	X	X
	R_{had}	X	X
EM Middle Layer	R_η	X	X
	w_2	X	X
	R_ϕ	-	X
EM Strip Layer	F_{side}	-	X
	w_{s3}	-	X
	w_{stotal}	-	X
	ΔE	-	X
	E_{ratio}	-	X

7.4   Missing Transverse Energy

In a p-p collider, like the LHC, momentum conservation along the $\hat{z}$ direction is impossible to measure because much of the longitudinal momentum is carried by the spectator quarks that hadronize down the beam pipe and cannot be detected. The particles that are detected and triggered on by ATLAS are mainly the products of hard collisions between partons. The fraction of the longitudinal momentum carried by these interacting partons is not known, however, the total transverse momentum before and after the collision is known to be approximately zero. Particles produced in a collision that do not interact with the ATLAS detector will, therefore, still leave a signature via missing transverse momentum. The ATLAS calorimetry system measures the energy lost by particles that traverse it. This deposited energy can translate into a measurement of the missing transverse momentum through the use of a variable known as transverse energy [12]. Transverse energy, E_T, is the energy of a particle in its rest frame where its $p_z = 0$. This variable is invariant under boosts along the $\hat{z}$ direction and is defined as follows:

$$E_T^2 = p_x^2 + p_y^2 + m^2 = p_T^2 + m^2 = E^2 - p_z^2 \tag{7.15}$$

From Eq. 7.15 it can be seen that transverse energy and transverse momentum are almost equal for relativistic particles. Furthermore, Eq. 6.2 can be re-arranged to yield the following identity for p_z:

$$p_z = E \tanh y \tag{7.16}$$

Using the fact that in the relativistic limit,

$$\cos \theta = \tanh y \tag{7.17}$$

the transverse energy can be written as follows:

$$E_T = E \sin \theta \tag{7.18}$$

The missing transverse momentum can, therefore, be detected by measuring the transverse momentum or the transverse energy of all the particles produced in an event. The ATLAS experiment uses several different methods for measuring this quantity [41] [40]. The method that was employed in this analysis uses calibrated three dimensional clusters of cells, called topoclusters, within the calorimeters. The algorithm used to define topoclusters is summarized in section 7.4.1 and the energy calibration of these clusters is briefly outlined in section 7.4.2. This procedure was found to be robust enough for the early data taking period because it does not rely on the validation of the particle reconstruction algorithms. The reconstructed missing transverse energy is defined as:

$$E_T^{miss} = \sqrt{(E_x^{miss})^2 + (E_y^{miss})^2} \tag{7.19}$$

where,

$$E_x^{miss} = -\sum_i E_i \sin \theta_i \cos \phi_i \tag{7.20}$$

and,

$$E_y^{miss} = -\sum_i E_i \sin \theta_i \sin \phi_i \tag{7.21}$$

where the index i runs over all the topoclusters formed in the event and E_i, θ_i, and ϕ_i are the energy, polar angle and azimuthal angle of the corresponding topocluster. Another related variable that has been used in this analysis is the scalar sum of all the transverse energy in the event, $\sum E_T$:

$$\sum E_T = \sum_i E_i \sin \theta_i \tag{7.22}$$

This variable measures the level of activity within the calorimeters for the event and affects the E_T^{miss} resolution.

7.4.1   Topoclusters

Topoclusters are the basic constituents of the reconstructed missing transverse energy. Topological clustering algorithms [54] group neighbouring cells with significant energy
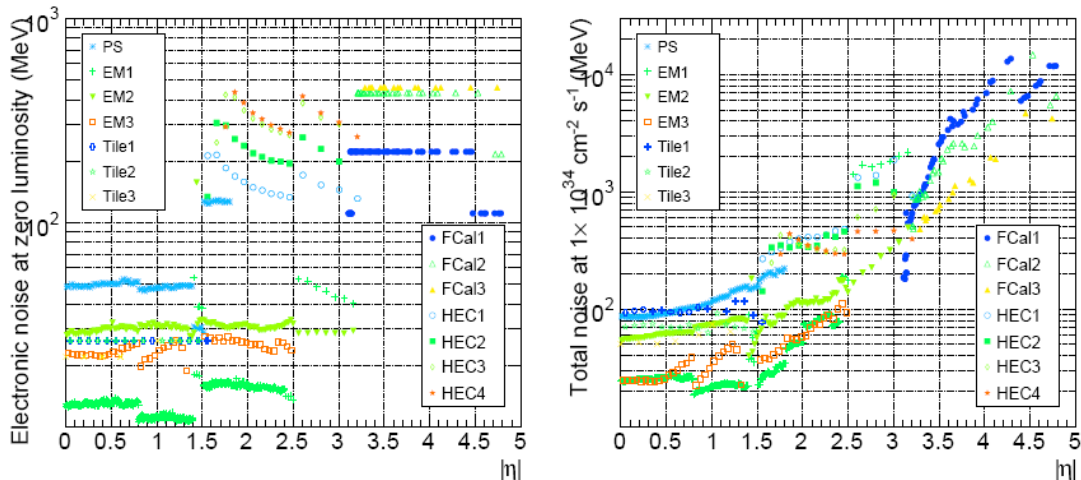
Figure 7.3: *Electronic noise (left) and predicted total noise at high luminosity (right), in MeV, for each calorimeter layer. [54].*

deposition above noise into clusters. Noise in this context is defined as the expected RMS of the electronic noise and pile-up noise added in quadrature; the Gaussian width of the cell energy distribution measured in randomly triggered events. Pile-up noise is associated with the superposition of the triggered event with other inelastic collisions within the same or neighbouring bunch crossing. As can be seen in figure 7.3, the amount of noise in the calorimeters varies quite significantly between the various layers and subdetectors of the ATLAS calorimeter and increases with increasing capacitance which depends on the geometry of the cells in each subdetector. The noise in the endcaps and forward calorimeters is dominated by pile-up at high luminosity. In contrast to the sliding window algorithm used in the reconstruction of electrons and photons, topoclusters have variable numbers of associated cells. The formation of topoclusters involves two steps; the cluster making step and the cluster splitting step.

In the cluster making step, the seed cells for the topoclusters are identified by creating an ordered list of all cells with $|E| > 4\sigma_{noise}$. The absolute value of the cell's energy is used in this context in order to ensure a symmetric contribution from noise. All neighbouring

cells which do not belong to the seed list and have $|E| > 2\sigma_{noise}$ are then added to the seed to form a 'proto-cluster', the neighbouring cells assume the role of the seed cells in the next iteration of this step. Any set of 'proto-clusters' that share a neighbouring cell are merged. In the final step, all cells on the periphery of the 'proto-cluster' are added to the cluster as well. This ensures that the tails of the shower are not discarded. Once again, if these periphery cells are associated with several 'proto-clusters' then they are added to the cluster seeded by the highest signal-to-noise significance.

The 'proto-clusters' formed by this iterative procedure could potentially be quite large, especially in the forward region where there is a higher particle density and a greater chance for overlapping showers. The purpose of the topocluster algorithm is to reconstruct a three dimensional representation for a single particle's shower development. It is, therefore, necessary to introduce a mechanism to split these 'proto-clusters' such that they are more likely to be associated with the energy deposition of a single particle traversing the ATLAS calorimeter. The cluster splitting step begins by looking at local maxima within each 'proto-cluster' with $E > 500\text{MeV}$, having at least 4 neighbouring cells with smaller energy and also belonging to the 'proto-cluster'. Each local maxima, in turn, seeds the formation of a new cluster through an iterative procedure as before, but only using the cells within the original 'proto-cluster' and excluding the merging step. The newly formed topoclusters are three-dimensional energy depositions within the calorimeter that sometimes share overlapping cells at their borders. A typical event could contain around 250 topoclusters. The number of cells in each topocluster is variable and depends on the energy of the incoming particle and its direction in η. However, this number could vary from around 200-500 cells/cluster for a typical cluster transverse energy between 20-500 GeV. In a typical di-jet event, each topocluster corresponds to approximately 1.6 stable particles such as pions or photons [54].

7.4.2 Local Hadronic Calibration

The ATLAS calorimeters are non-compensating, which means that their response to electrons/photons differs from their response to hadrons. The energy depositions that are visible to the calorimeters arise from interactions involving ionization, however interactions that do not involve ionization such as the break-up of nuclear bindings or the energy of particles like muons or neutrinos that either interact very little or escape are not visible. Therefore, it is necessary to calibrate the topocluster energies in order to account for this invisible, or escaped energy, that may be present in hadronic showers, based on the visible energy depositions in the active regions of the calorimeters. The calibration scheme that has been utilised for the measurement of missing transverse energy is referred to as local hadronic calibration [42] and consists of four steps which collectively correct the energy of the noise-suppressed topoclusters for calorimeter non-compensation effects, losses due to noise thresholds and dead material within the detector.

The first step of the local hadronic calibration method involves the classification of topoclusters coming from either electromagnetic or hadronic showers. The main classification variables used for this purpose involve the energy weighted lateral and longitudinal cluster profiles, the energy density of the clusters, and the depth of the shower maxima. The lateral and longitudinal cluster profiles use the fact that electromagnetic showers exhibit more compact shower shapes than hadronic showers. The energy density of the clusters use the property that electromagnetic showers deposit all their energy in a form that is visible to the calorimeters and in more compact showers. These variables have been studied for charged and neutral pions as a function of their energy and their direction in η. This scheme has a classification efficiency of 80-85% for neutral pions above 50 GeV, and 80-90% over the entire energy range for charged pions.

The second step of this calibrations scheme assigns weights to the cell energies within the clusters classified as hadronic, in order to correct for invisible and escaped energy. The cell weights are estimated from simulations of charged and neutral pions showering

within the ATLAS calorimeters as a function of the cluster energy to which the cell belongs, the energy density of the cell, and the position of the cell center in $|\eta|$. The third step corrects for out of cluster energy depositions within the calorimeter which are mainly due to the noise thresholds introduced in the clustering algorithm. This correction is determined from single pion simulations as a function of the pion energy, η value and shower depth within the calorimeters. The fourth step corrects both electromagnetic and hadronic cluster energies for depositions outside of the calorimeters and is again based on simulations of neutral and charged pions. This calibration scheme has been validated with testbeam and collision data [42].

Chapter 8

Samples and Event Selection

8.1 Data Samples and Trigger

The data sample used in this analysis [35] was collected by the ATLAS detector at the LHC in proton-proton collisions at a center-of-mass energy of $\sqrt{s} =$7 TeV. It includes all runs during the period from March 30th, 2010 until August 30th, 2010, referred to as periods A, B, C, D, E and F. The analysis has also been extended to the full 2010 data set ending on November 4th, 2010 [31]. The data were collected using triggers that select events with at least one loose photon. Only events from periods when all detector components were functioning as expected are used. These are referred to as good runs.

Good runs are those in which both the solenoid and the toroid magnets were operating at their nominal fields to ensure good momentum measurements required for separating electrons from photons. There was also a further requirement that there be no significant deviations from the averaged out calorimeter response, particle identification, as well as energy and momentum distributions. The systems needed for missing momentum reconstructions and photon trigger system selections were also required to be fully operational. Table 8.1 summarizes the integrated luminosity recorded by the ATLAS detector after the good runs criteria for each data taking period along with the

corresponding trigger configurations. The initial analysis was performed on 3.1 pb^{-1} of data which corresponded to approximately 170 million events that passed at least one of the egamma triggers.

The trigger used in this analysis is referred to as *g20_loose*. It is a three level trigger starting from a L1 calorimeter only selection (L1_EM14). The L1 output rate for this trigger chain was low enough during the first periods of data taking that no further HLT selection was required up to and including period E2. The L1 selection accepts events which have at least one transverse energy deposit in the EM calorimeter above 14 GeV in a fixed EM window size of 0.2×0.2 in $\eta \times \phi$. The corresponding HLT selection introduces an extra 20 GeV cut on the transverse energy deposit in the EM calorimeter in conjunction with cuts on the shape of the shower deposit in both the EM and hadronic calorimeters. These shower shape cuts are similar to the ones in the loose photon identification selection described in section 7.3.2. The efficiency of this trigger chain is found to be 100%, within statistical uncertainties, for both the collected data and the UED signal Monte Carlo samples for loose photons with E$_T$ above 25 GeV. The selection of this trigger configuration was based on the desire to minimize the cut on the transverse energy of the photon candidates at trigger level and to maximize the available luminosity by selecting an un-prescaled trigger.

8.2 Simulated Samples

8.2.1 UED Signal Samples

Universal extra dimension Monte Carlo samples were used to determine the baseline selection and estimate the signal efficiencies following each cut, used in systematic studies. The signal samples were simulated with gravity mediated UED parameter values $\Lambda R = 20$, $N = 6$ and M$_D = 5$ TeV for various values of $1/R$. Pythia is used for the computation of UED decay widths, branching ratios, the generation of MC events, and cross section

Table 8.1: *Integrated luminosity and triggers used for each data taking period.*

Period	Integrated Luminosity [pb^{-1}]	Trigger
A	0.3×10^{-3}	L1_EM14
B	7.0×10^{-3}	L1_EM14
C	8.4×10^{-3}	L1_EM14
D	0.24	L1_EM14
E1-E2	0.23	L1_EM14
E3-E7	0.78	g20_loose
F	1.80	g20_loose
Total:	3.1	-

calculations [26]. The cross sections involved Feynman diagrams with the fewest number of possible vertices (referred to as leading order - LO). Calculations that also include the addition of another vertex to the LO diagrams will be referred to as Next-to-leading-order (NLO) predictions. NLO cross section predictions for this UED model have not yet been computed, therefore all results that will follow are based on the LO calculations. Table 8.2 provides a list of the signal UED samples generated including the predicted LO cross sections. Each sample consists of 10,000 events generated using MRST2007LOmod [30] parton distribution functions. The events are processed with a full GEANT4 [52] based simulation of the ATLAS detector and reconstructed with the same algorithms that are applied to data.

Two types of special samples were generated for systematic studies of the uncertainties associated with extra material effects in the detector and pile-up. Three extra material samples were generated for 1/R values of 300, 700 and 1000 GeV/$\hbar c$ respectively. In these samples, additional dead material was added to the inner detector and calorimetry system. The inner detector material changes included a 15% material increase in the whole inner detector, a 20% increase in Pixel and SCT service components, a 15% increase

Table 8.2: *Signal cross sections for different 1/R values, with $\Lambda R = 20$, $N = 6$ and $M_D = 5$ TeV/c² for proton-proton collisions at $\sqrt{s} = 7$ TeV. MC samples with 10,000 events each were produced for all 1/R values.*

Signal 1/R [GeV/$\hbar$c]	Cross section [pb]	Generator
300 (with/wo extra material)	709.6	Pythia
330	405.7	Pythia
350	288.8	Pythia
400	127.2	Pythia
460	52.98	Pythia
500	30.28	Pythia
555	14.99	Pythia
575	11.59	Pythia
600 (with/wo pile-up)	8.588	Pythia
625	6.428	Pythia
650	4.851	Pythia
675	3.672	Pythia
700 (with/wo pile-up, extra material)	2.770	Pythia
725	2.100	Pythia
750	1.644	Pythia
775	1.226	Pythia
800 (with/wo pile-up)	0.966	Pythia
900	0.354	Pythia
1000 (with/wo extra material)	0.132	Pythia

to the end of the SCT/TRT endcap region and a 15% increase to the inner detector endplates. The calorimetry material changes included a radial increase of 0.1 X_0 in the barrel cryostat regions before the presampler followed by a radial increase of 0.05 X_0 in the region between the presampler and the first layer of the calorimeters. The effects of pile-up, i.e. referring to the presence of a signal in the detector which originates from an interaction other than the hard-scattering event in a given bunch crossing, were studied using special signal samples for 1/R values of 600, 700 and 800 GeV/$\hbar$c. For these samples the number of interactions per bunch crossing was set equal to 2, which was the average number of interactions per event during this period of data taking. However, due to poor agreement in the distribution of the number of primary vertices per event between data and Monte Carlo, some events in these samples were given a lower weight based on their number of primary vertices before any systematic studies. A primary vertex in this context refers to any reconstructed vertex in the event that has at least 3 associated tracks and is within 150 mm of the average beam spot position.

8.2.2   Background Samples

The Standard Model background contribution to the signal sample, after all cuts, was derived using a data driven method. However, Monte Carlo samples were used to define the baseline cuts by determining the expected number of background events, verify assumptions about the properties of background events and as a cross-check on the data driven background estimation method. The samples used are listed in tables 8.3, 8.4, 8.5, and 8.6, along with their expected cross sections, the equivalent integrated luminosity for the number of events per sample, and the generators used. The samples can be divided into three types; the irreducible background from events with missing transverse energy arising from the hard interaction process accompanied by two photons (table 8.3), the reducible background from QCD in which the contribution to large missing transverse energy is dominated by instrumental effects (table 8.4) and the reducible background

from events with genuine large missing transverse energy (table 8.5). These backgrounds and the corresponding Monte Carlo samples used to estimate their contribution are described below. The samples were normalized to the integrated luminosity of the data in order to study the background expectations.

(I) IRREDUCIBLE BACKGROUND

Events containing $W(\to l\nu)+\gamma\gamma$ and $Z(\to \nu\nu)+\gamma\gamma$ can fake signal events as they have genuine missing transverse energy due to the high p_T neutrinos in their final states. The two photons in the event come from intial or final state radiation. They are not accounted for using the data driven background estimation method used in this analysis. Monte Carlo simulations of these events show that their corresponding cross-sections are in the nanobarn range and that this contribution would be negligible for a 3.1 pb^{-1} study. The extension of this analysis to higher integrated luminosities has included this contribution by using Monte Carlo distributions of the missing transverse energy.

Table 8.3: *Irreducible Standard Model background processes along with their cross-sections, their effective integrated luminosity as determined by the number of events per sample and the generators used to simulate the events.*

Process	Cross section [pb]	Integrated Luminosity [pb^{-1}]	Generator
W $(\to \tau\nu) + \gamma\gamma$	7.0×10^{-8}	2.9×10^{11}	Madgraph4+Pythia
Z $(\to \nu\nu) + \gamma\gamma$	1.5×10^{-8}	6.9×10^{11}	Madgraph4+Pythia

(II) REDUCIBLE BACKGROUND WITH INSTRUMENTAL MISSING TRANSVERSE ENERGY

This type of reducible background includes events in which there is fake missing transverse energy due to instrumental effects combined with the possible presence of neutrinos and/or muons in hadronic showers associated with jets. The instrumental effects that

could give rise to large missing transverse energy are associated with poorly reconstructed particle energies within the detector that could arise, for example, from dead or noisy calorimeter regions or the presence of non-collision backgrounds. The types of processes considered in the background Monte Carlo studies include Standard Model diphoton production, γ+jets, dijets and Z($\rightarrow ee$) events, in which the diphoton final state could in some instances arise from hadronic jets or electrons faking a photon.

The Diphoton Sample - This sample includes the hard subprocesses that include two hard photons in their final state with a cut of 15 GeV/c applied to the transverse momentum of one of the photons. They include the Born $q\bar{q} \rightarrow \gamma\gamma$, the Box $gg \rightarrow \gamma\gamma$ and the Bremsstrahlung $qg \rightarrow q\gamma \rightarrow q\gamma\gamma$ processes shown in figure 8.1. This sample has been generated using LO Pythia with the MRST2007-LOmod parton distribution functions. The LO+NLO cross-sections are calculated by running DIPHOX and JET-PHOX [49] respectively with CTEQ6.6 [50]. These NLO cross sections are compared to the Pythia+MRST2007 LOmod cross sections. The ratio of the NLO to LO cross section for a given process is referred to as the K-factor. The K-factors for these processes are estimated to be 2.5 and have been included as event weights in the background Monte Carlo studies [55].
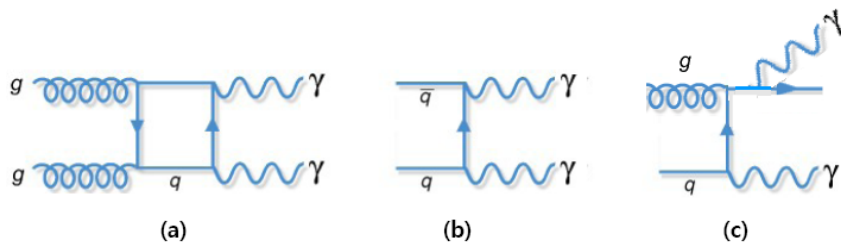
Figure 8.1: *The Standard Model background processes involving two final state photons and fake missing transverse energy. Figure (a) shows the Box process $gg \rightarrow \gamma\gamma$, (b) is the Born process $q\bar{q} \rightarrow \gamma\gamma$, and (c) is the bremsstrahlung process $qg \rightarrow q\gamma \rightarrow q\gamma\gamma$.*

The γ+jets Sample - This sample includes hard subprocesses $qg \to q\gamma$ and $q\bar{q} \to g\gamma$ with a generator level requirement that at least one of the final state photons, including those arising from initial or final state radiation, have a $p_T > 17$ GeV/c. The events have been generated as above and a K-factor of 2.5 has been estimated and included as weights in the background studies [55].

The Dijet Sample - The contribution from low p_T dijet events, ie. $p_T < 140$ GeV/c, has been estimated using three sets of jet samples generated with Pythia and referred to as JF17, JF35 and JF70. These samples have been produced with hard scattering cuts $p_{T,truth} > 15, 33, 65$ GeV/c respectively. In addition, if the vector sum of the p_T for all particles which deposit their energy in the EM calorimeter in an $\eta \times \phi \approx 0.2 \times 0.2$ window has $|\sum_i \vec{p}_{T,i}| > 17, 35, 70$ GeV/c respectively, the event is kept. In order to avoid double counting of the γ+jets contribution, these events have been removed from the JFX samples in all background studies. The samples were merged by imposing a cut on the transverse energy of the highest E_T reconstructed photon in the event: $E_T^{\gamma 1} < 45$ GeV, $45 < E_T^{\gamma 1} < 80$ GeV and $E_T^{\gamma 1} > 80$ GeV for JF17, JF35 and JF70 respectively. The contribution from dijet events with $p_T > 140$ GeV/c, has been studied using three samples of inclusive jet events generated with Pythia in different momentum slices to ensure adequate statistics for large jet energies. The hard interaction of the event is modeled via 2$\to$2 leading order matrix elements with the addition of initial and final state radiation. The samples are referred to as 'Dijet' in table 8.4 and the three samples refer to different slices of the momentum of the hard process, $\hat{p}_T$. There is no overlap between these samples, but a cut on the p_T of the leading reconstructed photon, $E_T^{\gamma 1} > 80$ GeV, has been introduced in order to avoid overlap with the JF samples.

The Z($\to ee$) samples - Six sets of Z($\to ee$)+Np$_i$ (with number of partons Np$_i$=0-5) samples were used. The diphoton signature would primarily come from electrons faking photons, but these samples are believed to model the multiparton final states well, which would contribute to the large missing transverse energy signature. These samples were

generated using Alpgen [47] which includes leading order electroweak and QCD effects for multiparton hard processes. The generator is, furthermore, interfaced with JIMMY [65] for underlying event simulation.

Table 8.4: *Reducible Standard Model background processes with large missing transverse energy from instrumental effects along with their cross-sections, their effective integrated luminosity as determined by the number of events per sample and the generators used to simulate the events.*

Process	Cross section [pb]	Integrated Luminosity [pb^{-1}]	Generator
Diphoton	103.3	967	Pythia
Photon+jet	1.0×10^5	48	Pythia
Photon+jet (with pile-up)	1.0×10^5	9.6	Pythia
Dijet ($140 \leq \hat{p}_T < 280$ GeV)	8.8×10^4	15.9	Pythia
Dijet ($280 \leq \hat{p}_T < 560$ GeV)	2348	593	Pythia
Dijet ($560 \leq \hat{p}_T < 1120$ GeV)	33.6	39948	Pythia
JF17	9.8×10^7	0.421	Pythia
JF17 (with pile-up)	9.8×10^7	0.102	Pythia
JF35	8.6×10^6	1.74	Pythia
JF70	6.9×10^5	1.45	Pythia
Z ($\to ee$) + Np0	664.1	458	Alpgen+JIMMY
Z ($\to ee$) + Np1	133.0	473	Alpgen+JIMMY
Z ($\to ee$) + Np2	40.2	472	Alpgen+JIMMY
Z ($\to ee$) + Np3	11.1	494	Alpgen+JIMMY
Z ($\to ee$) + Np4	2.9	518	Alpgen+JIMMY
Z ($\to ee$) + Np5	7.5×10^{-1}	664	Alpgen+JIMMY

(III) REDUCIBLE BACKGROUND WITH GENUINE MISSING TRANSVERSE ENERGY

Events in which the hard scattering process gives rise to a final state with neutrinos or muons could result in a large missing transverse energy signature. The diphoton signal could also arise from either one or two electrons or jets faking a photon. This contribution has been studied using the following Monte Carlo samples:

Top Pair Production - The $t\bar{t}$ final state could be an important background for this analysis because it has a large cross-section of 80 pb and approximately 54% of the time it has a decay product involving neutrinos. Each top quark decays to a W boson and a down-type quark. Each W boson, in turn, can decay leptonically (W$\to l\nu$) thus giving rise to a neutrino in the final state. The diphoton signature can, furthermore, come from one or two electrons or jets faking a photon. The MCNLO [60] generator, including full NLO QCD corrections has been used to simulate the hard process while JIMMY is used to generate the underlying event.

W($\to e/\mu/\tau+\nu$)+Np$_i$ Samples - In these types of events there is a genuine source of missing transverse energy in the hard scattering process. The final state always includes at least one neutrino. In the case of W($\to \mu + \nu$) processes, the final state muon will contribute to missing transverse energy as well. For W($\to \tau + \nu$) events, tau decays will include a neutrinos which will also result in missing transverse energy. The diphoton final state could possibly arise from one or two electrons or jets faking a photon. These W samples were generated for up to five parton matrix elements similar to the description given for the Z($\to ee$)+Np$_i$ samples.

Z($\to \mu\mu/\tau\tau$)+Np$_i$ Samples - Genuine large missing transverse energy in these events can come from either the muons in the final state or the neutrinos in tau decays. The diphoton signature can, once again, arise from the misidentification of electrons or jets as photons.

W$^\pm$($\to l\nu$)+γ Samples - One of the photons in these events comes from initial or final state radiation. The second photon in the event is fake and could come from either a lepton or a final state jet. The neutrino in the final state will contribute to

missing transverse energy. The possibility that the second photon in the diphoton final state signature could result from a real photon in W($\to l\nu$) events was further investigated with these samples. It was found to be a negligible background from Monte Carlo studies.

8.3   Signal and Background Topologies

The basic properties of the UED signal event topology compared to the expected Standard Model background were studied in Monte Carlo to select an enriched sample of signal events with low expected background. The most distinguishing features of the signal sample were found to be the existence of two high E_T photons passing the loose identification criterion, and a hard missing transverse energy distribution. A selection of some of the distinguishing variables has been included in figures 8.2 and 8.3 and will be described in this section. All distributions were plotted with the requirement that the event possess at least two reconstructed photons.

Figure 8.2 shows some of the distributions for the reconstructed photons in the event. As can be seen in figures 8.2(a) and 8.2(b), the UED signal sample is expected to have two very hard photons as compared to the Standard Model background. An E_T cut on the leading photon in the event can reduce the dijet background. A similar cut on the second leading photon in the event is very effective at further reducing the contributions from $t\bar{t}$ and γjet events. The invariant mass distribution of the two leading reconstructed photons in the event is plotted in figure 8.2(c). The two photons in the UED signal sample arise from the cascade decay of more massive first level Kaluza Klein excitations and are not associated with a resonance so no peaks are expected in the invariant mass distribution. However, a cut on this variable was considered as a possible alternative to an E_T cut on the photons. It was decided that the latter had more discriminating power while still maintaining a high signal efficiency. It should be noted that the small peak seen in the Z sample at around 90 GeV is associated with Z($\to ee$) events in which the electrons have

Table 8.5: *Reducible Standard Model background processes involving a top quark or W boson with genuine large missing transverse energy along with their cross-sections, their effective integrated luminosity as determined by the number of events per sample and the generators used to simulate the events.*

Process	Cross section [pb]	Integrated Luminosity [pb^{-1}]	Generator
$t\bar{t}$	80.1	12474	MCNLO+JIMMY
W $(\to e\nu)$ + Np0	6870	201	Alpgen+JIMMY
W $(\to e\nu)$ + Np1	1293	200	Alpgen+JIMMY
W $(\to e\nu)$ + Np2	376.6	502	Alpgen+JIMMY
W $(\to e\nu)$ + Np3	101.3	493	Alpgen+JIMMY
W $(\to e\nu)$ + Np4	25.3	514	Alpgen+JIMMY
W $(\to e\nu)$ + Np5	7.1	484	Alpgen+JIMMY
W $(\to \mu\nu)$ + Np0	6871	202	Alpgen+JIMMY
W $(\to \mu\nu)$ + Np1	1295	197	Alpgen+JIMMY
W $(\to \mu\nu)$ + Np2	376.1	499	Alpgen+JIMMY
W $(\to \mu\nu)$ + Np3	100.7	495	Alpgen+JIMMY
W $(\to \mu\nu)$ + Np4	26.0	500	Alpgen+JIMMY
W $(\to \mu\nu)$ + Np5	7.1	491	Alpgen+JIMMY
W $(\to \tau\nu)$ + Np0	6873	199	Alpgen+JIMMY
W $(\to \tau\nu)$ + Np1	1295	197	Alpgen+JIMMY
W $(\to \tau\nu)$ + Np2	375.1	501	Alpgen+JIMMY
W $(\to \tau\nu)$ + Np3	101.8	491	Alpgen+JIMMY
W $(\to \tau\nu)$ + Np4	25.8	505	Alpgen+JIMMY
W $(\to \tau\nu)$ + Np5	7.0	571	Alpgen+JIMMY
W$^+$ $(\to e\nu)$ + γ	28.0	1786	Madgraph+Pythia
W$^-$ $(\to e\nu)$ + γ	18.6	2689	Madgraph+Pythia
W$^+$ $(\to \mu\nu)$ + γ	27.9	1790	Madgraph+Pythia
W$^-$ $(\to \mu\nu)$ + γ	18.6	2689	Madgraph+Pythia
W$^+$ $(\to \tau\nu)$ + γ	25.4	11626	Madgraph+Pythia
W$^-$ $(\to \tau\nu)$ + γ	16.9	17241	Madgraph+Pythia

Table 8.6: *Reducible Standard Model background processes involving a Z boson with genuine large missing transverse energy along with their cross-sections, their effective integrated luminosity as determined by the number of events per sample and the generators used to simulate the events.*

Process	Cross section [pb]	Integrated Luminosity [pb^{-1}]	Generator
Z $(\to \mu\mu)$ + Np0	663.8	458	Alpgen+JIMMY
Z $(\to \mu\mu)$ + Np1	132.9	474	Alpgen+JIMMY
Z $(\to \mu\mu)$ + Np2	40.4	470	Alpgen+JIMMY
Z $(\to \mu\mu)$ + Np3	11.2	493	Alpgen+JIMMY
Z $(\to \mu\mu)$ + Np4	2.9	517	Alpgen+JIMMY
Z $(\to \mu\mu)$ + Np5	7.6×10^{-1}	660	Alpgen+JIMMY
Z $(\to \tau\tau)$ + Np0	662.5	458	Alpgen+JIMMY
Z $(\to \tau\tau)$ + Np1	133.9	470	Alpgen+JIMMY
Z $(\to \tau\tau)$ + Np2	40.3	484	Alpgen+JIMMY
Z $(\to \tau\tau)$ + Np3	11.0	498	Alpgen+JIMMY
Z $(\to \tau\tau)$ + Np4	2.8	535	Alpgen+JIMMY
Z $(\to \tau\tau)$ + Np5	7.8×10^{-1}	639	Alpgen+JIMMY

been reconstructed as photons. Figure 8.2(d) shows the angular distribution between the two leading reconstructed photons. Once again, this is an almost flat distribution for the UED signal sample, but the two leading photons in the Standard Model background have a greater tendency to be back-to-back or collinear. The greater tendency for collinear leading photons in dijet, $t\bar{t}$, W, and Z events is because they actually arise from hadronic jets that involve the decay of neutral mesons, such as π^0's or η's, to two photons. It can also be seen that in samples where the two hardest particles/jets in the event are mainly back-to-back, such as the γjet sample, the two leading reconstructed photons in the event also exhibit this property. This is mainly due to a jet faking a photon. Figure 8.2(e) shows the number of photons that pass the loose identification criterion in the event. Requiring that both the leading photons pass the loose identification criterion can significantly reduce the Standard Model background contribution, in which fake photons from jets are expected to be prevalent. Finally, the E_T^{Cone20} distribution is depicted in figure 8.2(f). This variable measures the relative isolation in the transverse energy distribution of the photon candidates. It is computed from the transverse energy deposited in both the electromagnetic and hadronic calorimeters in a cone of half opening angle 0.2 in $\eta - \phi$ space around the photon candidate direction, while excluding the energy of the photon itself. It is expected to be large for poorly isolated photons that may arise from misidentified jets, or photons that are close to another particle. From this distribution, it can be seen that a very loose cut on the relative isolation can reduce the contribution from dijets to the signal region. However, the main reason why this variable plays an important role in this analysis is that it can be used to alter the composition of the background control sample, this will be further discussed in section 9.

Figure 8.3(a) shows the missing transverse energy distribution for the signal and Standard Model background. The UED signal distribution has a much harder E_T^{miss} spectrum that peaks at around 100 GeV. This distribution becomes harder as the compactification radius of the universal extra dimension becomes smaller. This is because the lightest
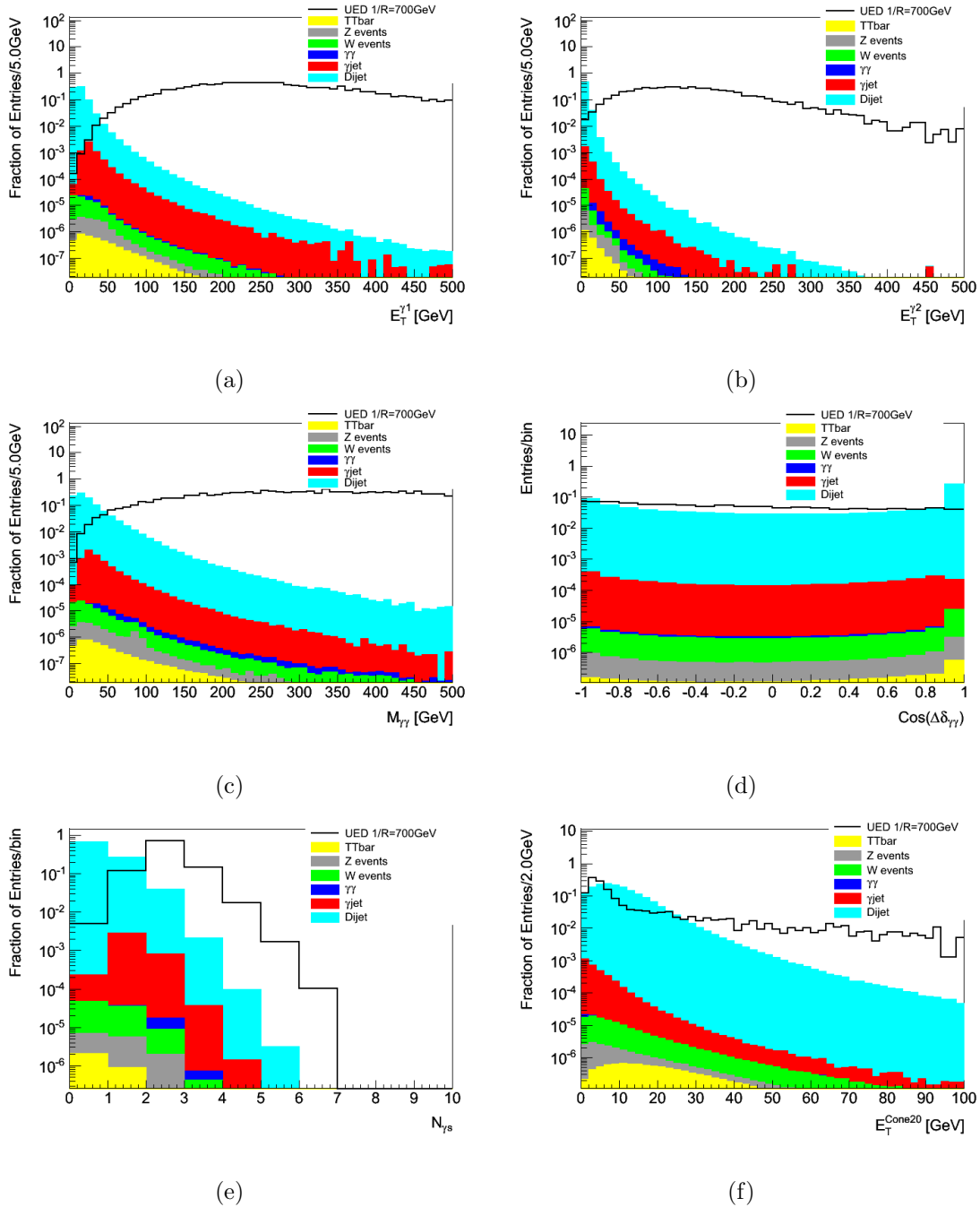
Figure 8.2: *The Standard Model background and UED Signal (1/R=700 GeV/ℏc) distributions for photon variables after requiring the existence of at least 2 reconstructed photons in the event. Both the signal and the summed background distributions have been normalized to one. The variables plotted include a) the E_T distribution of the leading photon, b) the E_T distribution of the second leading photon, c) the invariant mass distribution of the two leading photons in the event, d) the cosine of the angular distribution between the two leading reconstructed photons, e) the number of reconstructed photons that pass the Loose identification criterion, and f) the distribution of the E_T^{Cone20} isolation variable for the two leading photons.*

Kaluza Klein particle, $\gamma*$, has a mass equal to 1/R and the missing transverse energy in the event mainly comes from the excited gravitons associated with the 6 eV^{-1}-sized extra dimensions. The graviton mass distribution has a continuous shape, from 0 to 1/R, as a consequence of the fact that the graviton field appears as a massless particle with a tower of excited modes whose masses differ by order eV. This distribution also highlights the expected backgrounds that contribute to small and large E_T^{miss} values. For low E_T^{miss} values, < 20 GeV, the Standard Model background is dominated by dijets, $\gamma jets$, and $\gamma\gamma$ events. However, at larger values, W events also become important. The $\sum E_T$ distribution is shown in figure 8.3(b) showing the peaks of the distributions and the relative contribution from the Standard Model background. The sharp lower cut-offs are explained by the inherent p_T cuts introduced while generating the various Monte Carlo samples. This distribution shows that the UED signal events are expected to have a larger overall transverse energy distribution than the Standard Model background.

Each photon in the UED signal sample is a product of the cascade decay of excited Kaluza Klein particles which results in a signal topology that includes many jets with transverse momenta proportional to the mass splittings between the various excited Kaluza Klein particles. The p_T distribution of the leading jet in the event is shown in figure 8.3(c). The UED signal events include hard jets that explain the larger $\sum E_T$ distribution discussed above. Figure 8.3(d) shows the jet multiplicity for UED signal and the Standard Model background. Only jets with p_T > 30 GeV/c are included in this distribution, this shows the presence of many high p_T jets in the UED signal sample. In fact, the jet topology of UED events is very similar to that of $t\bar{t}$ events.

Some of the main discriminating variables for the UED signal topology were discussed in this section in order to highlight some of the key features of UED signal events as compared to the Standard Model background. The most discriminating variables were found to be associated with the E_T spectrum of the two leading photons with the loose photon identification criterion along with the distribution of missing transverse energy.
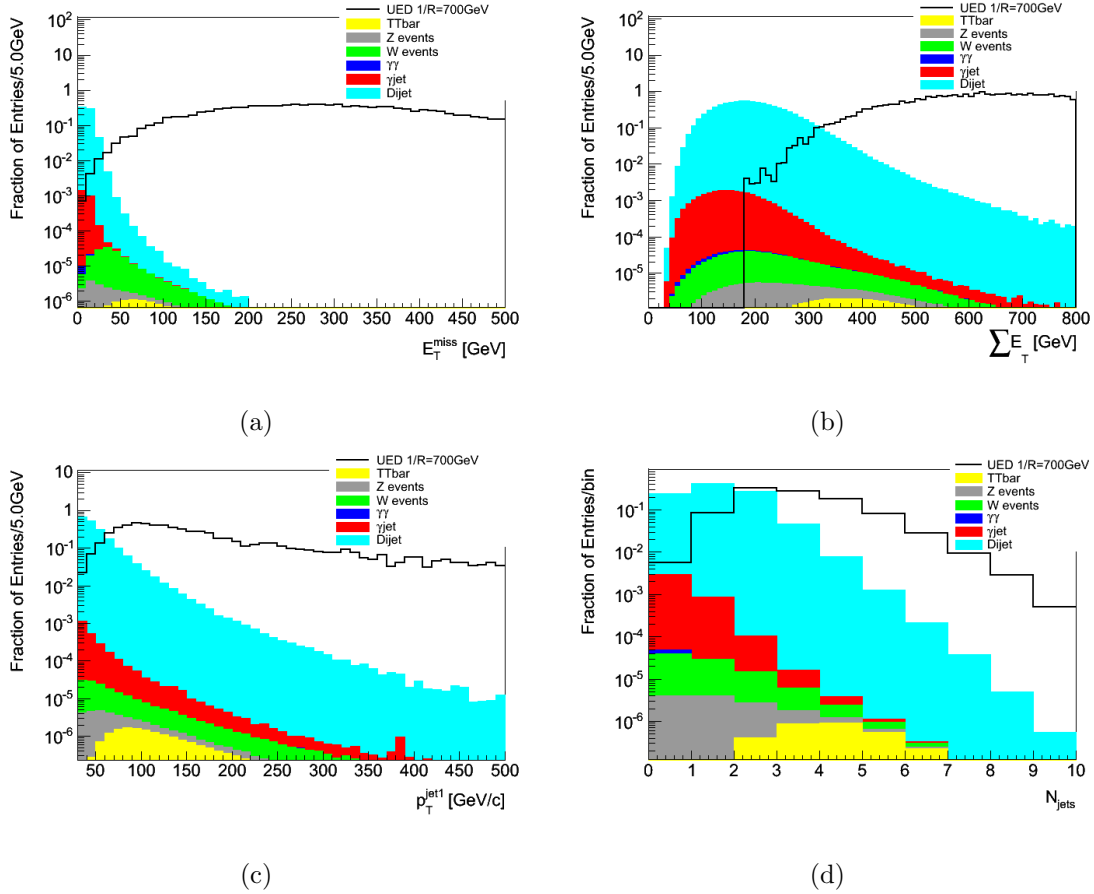
Figure 8.3: *The Standard Model background and UED Signal (1/R=700 GeV/ℏc) distributions for missing transverse energy and jet variables after requiring the existence of at least 2 reconstructed photons in the event. Both the signal and the summed background distributions have been normalized to one. The variables plotted are a) the missing transverse energy distribution in the event, b) the scalar sum of the transverse energy in the event, c) the p_T distribution of the leading jet, d) the number of jets/event with $p_T > 30$ GeV/c.*

The choice of the specific values of the cuts will be discussed in the next section.

8.4   Event Selection

Standard Model Monte Carlo and Monte Carlo UED signal samples were used to optimize the cuts applied to data. The aim of the Monte Carlo optimization procedure was to provide a clean sample of potential UED signal events with low levels of Standard Model background events in data. These cuts included the loose photon identification and isolation criterion on the two leading photons in the event, followed by cuts on their respective transverse momenta, and the missing transverse energy. A summary of this optimization procedure and the final event selection is provided in section 8.4.2. Apart from the trigger and good runs list requirements described in section 8.1, a set of cleaning cuts was also required to remove events that had a high likelihood of coming from non-collision backgrounds, or suffered from detector problems. A summary of these event cleaning cuts is described in section 8.4.1.

8.4.1   Cleaning Cuts

Prior to analyzing the data, it was important to do some event cleaning first. All events in data were required to have at least two reconstructed photons within the η acceptance of the presampler and not pointing to the crack region of the EM calorimeter. This corresponds to the following condition: $|\eta| < 1.81$, and $|\eta| < 1.37$ or $|\eta| > 1.52$. As described in section 6.4.1, the crack region is the region between the barrel and end-cap EM calorimeters which, due to its lack of instrumentation, results in poorly reconstructed EM objects.

In order to reduce the contribution from events due to non-collision backgrounds, the presence of at least one primary vertex consistent with the average beam spot position is required. Non-collision backgrounds may include cosmic rays passing through the

detector, instrumental effects such as electronic noise bursts within the detector, beam gas collisions in which protons collide with gas molecules in an imperfect vacuum, and beam halo effects where outlier protons collide with the beam-cleaning collimators upstream of ATLAS. The average beam spot position is continuously monitored and is based on the distribution of the position of reconstructed primary vertices collected from many events. This analysis only considered events in which there was one primary vertex, PV, with three associated tracks and a z position satisfying $PV_z < 150$ mm.

Tails in the missing transverse energy distribution arising from detector issues such as electronic noise bursts, non-collision backgrounds or mismeasured objects, such as jets pointing to the crack regions, could give rise to events faking a UED signal. In order to reduce the contribution from such effects, all events in which a jet with an EM-scale transverse momentum greater than 10 GeV/c was labeled as 'bad' or 'ugly' were rejected; these terms are clarified in the following. The reconstructed jets often overlap with the leading photons in the event, therefore, some of these cleaning cuts had the added benefit of acting as a cleaning cut on reconstructed photons as well.

A jet was labeled as 'bad' if more than 90% of the jet's energy was contained in at most 5 calorimeter cells and greater than 80% of the jet's energy was contained in the hadronic end-cap. This criterion was designed to reject events in which sporadic electronic noise bursts common to cells in the hadronic end-caps seed a jet. Noise was alos removed by examining the "quality" of the calorimeter signals. The quality of a calorimeter cell quantifies the difference between the measured pulse shape and the predicted pulse shape used to reconstruct the cell energy. Although most of the events with noise bursts in the hadronic end-caps are removed by the cut already mentioned, a few still remain that may be attributed to the presence of some underlying activity, such as pile-up, in the calorimeter surrounding the region where a bad HEC cell may be situated. Therefore, events containing jets that have a large fraction of their energy coming from the HEC and a low quality were also rejected. If the fraction of the jet's energy from bad quality

calorimeter cells was greater than 80% and the fraction of the jet's energy from the EM calorimeter was greater than 95%, the jet was rejected. This eliminates events in which rare noise bursts in the EM calorimeter caused coherent noise. Jets reconstructed from large out-of-time energy depositions in the calorimeter, such as photons produced by cosmic ray muons, were also eliminated, using a cut on the jet time, defined with respect to the event time. The jet time is given by:

$$t_{jet} = \sum_i E_i^2 t_i \tag{8.1}$$

where i runs over all the cells that make up a jet, E_i is the energy deposited in that cell, and t_i is the timing of the energy deposition with respect to the event time. Jet times were required to be within two beam bunch crossing (or < 50 ns).

Jets seeded by real energy depositions, but located in problematic calorimeter regions were labeled as 'ugly' and the event was removed. Problematic calorimeter regions included regions with dead cells and noisy cells that were masked during reconstruction. The energy deposits in these cells were extrapolated from the energy of their neighbouring cells and rescaled by the volume of the cells. Any event containing a jet in which more than 50% of its total electromagnetic energy was attributed to corrected-for-dead cells or masked cells was removed. If more than 50% of the jet's energy is deposited in scintillators located in the gap between the tile calorimeter barrel and end-caps, the event was also removed. The calibration of these scintillators is not optimal and could lead to mismeasured E_T^{miss}.

The above set of jet cleaning cuts removed only 0.05% of our data events but were effective at removing high energy tails in the E_T^{miss} distribution, as shown in figure 8.4.

Finally, in order to ensure that the reconstructed photons in the event were not built from a cluster affected by a detector problem, a set of object quality cuts were also applied. These cuts rejected all events in which either one of the two leading reconstructed photons contained a cluster that was associated to a detector region with a known problem. The types of problems considered included dead or non-nominal high voltage regions, and
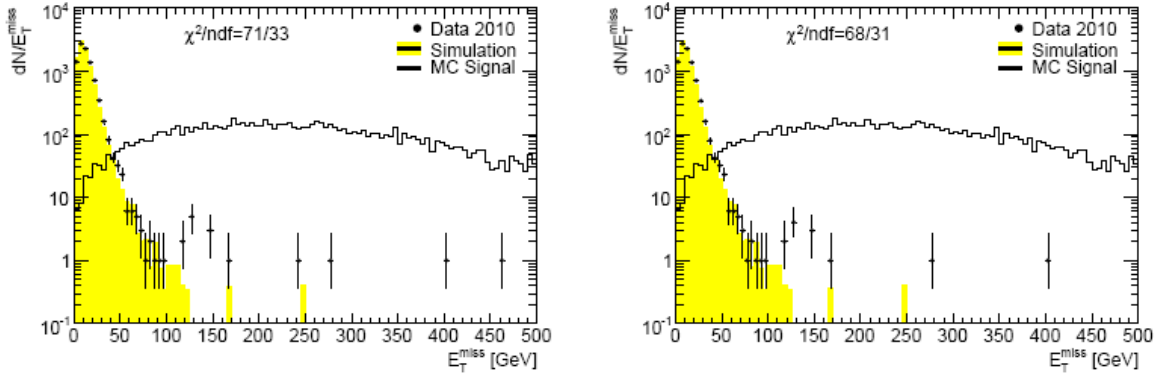
Figure 8.4: *Data and MC ($\gamma\gamma + \gamma jet+JF17+JF35+JF70$) distributions for E_T^{miss} after requiring the presence of 2 leading photons with $E_T > 25$ GeV and imposing the trigger requirement followed by all cleaning cuts except jet cleaning (left), with jet cleaning cut (right). A 2.5 K-factor has been applied to the $\gamma\gamma$ and γjet events. The $1/R=700$ GeV/$\hbar c$ UED signal sample is superimposed but not normalized, while the background MC is normalized to the number of data events [55].*

problematic cells which may have been masked in the reconstruction step.

8.4.2   Final Signal Selection Cuts

The cleaning cuts described in the previous section were designed to reject events without proton-proton collisions and ensure good quality of reconstructed jets, photons and E_T^{miss}. The final signal selection cuts, which will be described in this section, provide a clean sample of possible UED signal events while reducing the contribution from Standard Model background events. The optimization of the final set of cuts was accomplished using Monte Carlo samples of the Standard Model backgrounds and UED signal samples. The selection cuts resulting from the optimization procedure were then applied to data as will be discussed in section 8.4.3. The Monte Carlo optimization started by introducing a set of identification cuts on the photon candidates that would reduce the background from dijet events with a large cross section. To do this, the two most energetic photons in the

event were required to pass the loose photon identification criterion. The loose selection was chosen for this analysis because of the limited statistics in data if tight identification was used. The photon identification criteria were combined with an isolation cut of $E_T^{cone20} < 35$ GeV. This was found to provide a clean signal sample with very low expected background. The isolation cut mainly reduces the contribution from Standard Model dijet events. It has the added benefit of reducing the correlation between the loose identification criterion and the E_T^{miss} background composition spectrum required for the data driven background estimation method described in section 8.1.

The selection of the final set of E_T cuts to be applied to the leading photons in the event and the value of the E_T^{miss} cut was determined by optimizing for their discovery or exclusion potential in Monte Carlo. A summary of the results of this optimization procedure is outlined in table 8.7 using the following set of cuts:

- **Cut 1a)** - $E_T^{\gamma 1,2} > 25$ GeV and $E_T^{miss} > 50$ GeV.

- **Cut 1b)** - $E_T^{\gamma 1,2} > 25$ GeV and $E_T^{miss} > 75$ GeV.

- **Cut 1c)** - $E_T^{\gamma 1,2} > 25$ GeV and $E_T^{miss} > 100$ GeV.

- **Cut 2a)** - $E_T^{\gamma 1} > 50$ GeV, $E_T^{\gamma 2} > 25$ GeV and $E_T^{miss} > 50$ GeV.

- **Cut 2b)** - $E_T^{\gamma 1} > 50$ GeV, $E_T^{\gamma 2} > 25$ GeV and $E_T^{miss} > 75$ GeV.

- **Cut 2c)** - $E_T^{\gamma 1} > 50$ GeV, $E_T^{\gamma 2} > 25$ GeV and $E_T^{miss} > 100$ GeV.

- **Cut 3a)** - $E_T^{\gamma 1,2} > 50$ GeV and $E_T^{miss} > 50$ GeV.

- **Cut 3b)** - $E_T^{\gamma 1,2} > 50$ GeV and $E_T^{miss} > 75$ GeV.

- **Cut 3c)** - $E_T^{\gamma 1,2} > 50$ GeV and $E_T^{miss} > 100$ GeV.

Table 8.7 gives the expected integrated luminosity required for 10 UED signal events after applying each of the above cuts. The expected number of background events for

the calculated integrated luminosity is also shown in brackets. The entries that would

result in a 5σ discovery are in red and those representing a 1.64σ exclusion potential are

in boldface font. The criteria for discovery and exclusion follow the recommendations of

the ATLAS statistics forum [17] [24]. The formulae used to calculate significances follow

these guidelines and are given by:

$$Z_{discovery} = \sqrt{2[(S+B)\ln(1+S/B) - S]} \qquad (8.2)$$

$$Z_{exclusion} = \sqrt{2[(S - B\ln(1+S/B))]} \qquad (8.3)$$

where S is the number of expected signal events, and B is the number of expected

background events. Table 8.7 shows that for 3.135 pb^{-1} the expected discovery potential

lies between a $1/R$ value of 600 and 700 GeV/$\hbar$c using Monte Carlo samples. It also

shows that cut 1b) provides the best signal efficiency for this discovery potential. In

order to set an exclusion limit, an expectation of at least 3 UED events are required.

The expected exclusion potential for 3.135 pb^{-1} of data lie between a $1/R$ value of 700

and 800 GeV/$\hbar$c. Once again, cut 1b) would provide us with the best signal efficiency

for such an exclusion. Therefore, this cut was used to define the signal region.

8.4.3   Expected Number of Background Events and Signal Selection Efficiency

The percentage of events that survive each of the cuts mentioned is referred to as the

cut efficiency and is summarized in table 8.8, for data, the Monte Carlo background and

Monte Carlo UED signal ($1/R$=700 GeV/$\hbar$c) samples. The Monte Carlo samples have all

been normalized to the integrated luminosity of the data. The cuts optimized using Monte

Carlo were also applied to data. After applying all cuts, no events are observed in data.

This result shows that the UED scenario under investigation can be excluded for $1/R$

values between 700 to 800 GeV/$\hbar$c. Table 8.8 also shows a large data versus Monte Carlo

background discrepancy throughout. Prior to cut 8, the discrepancy can be assumed to

Table 8.7: *The integrated luminosity in pb^{-1} required for 10 UED signal events after applying the cuts defined in section 8.4.2 and, in the brackets, the expected number of Standard Model background events from Monte Carlo studies for the given integrated luminosity. The points for which a discovery significance of 5σ is expected, corresponding to < 1.72 background events are in red. The points for which an exclusion significance of 1.64σ are expected, corresponding to < 5 background events are in boldface font.*

Cut	1/R=300 GeV/ℏc	400	500	600	700	800	900	1000
1a)	**0.04 (0.01)**	**0.20 (0.07)**	**0.7 (0.2)**	**2.5 (0.8)**	**7.2 (2.4)**	20 (7)	53 (18)	139 (47)
1b)	**0.05 (0.00)**	**0.22 (0.02)**	**0.8 (0.1)**	**2.6 (0.2)**	**7.5 (0.7)**	**21 (2)**	**55 (5)**	142 (13)
1c)	**0.07 (0.00)**	**0.25 (0.01)**	**0.9 (0.1)**	**2.8 (0.2)**	**7.9 (0.4)**	**22 (1)**	**57 (3)**	147 (8)
2a)	**0.05 (0.01)**	**0.20 (0.05)**	**0.7 (0.2)**	**2.5 (0.6)**	**7.2 (1.8)**	20 (6)	53 (13)	140 (33)
2b)	**0.05 (0.00)**	**0.22 (0.02)**	**0.8 (0.1)**	**2.6 (0.2)**	**7.6 (0.5)**	**22 (1)**	**56 (4)**	143 (10)
2c)	**0.07 (0.00)**	**0.26 (0.01)**	**0.9 (0.0)**	**2.8 (0.1)**	**7.9 (0.3)**	**22 (1)**	**57 (2)**	147 (6)
3a)	**0.07 (0.01)**	**0.27 (0.03)**	**0.9 (0.1)**	**2.8 (0.3)**	**8.0 (0.8)**	**22 (2)**	57 (6)	147 (15)
3b)	**0.09 (0.00)**	**0.30 (0.01)**	**0.9 (0.0)**	**3.0 (0.1)**	**8.3 (0.3)**	**22 (1)**	**58 (2)**	**150 (5)**
3c)	**0.11 (0.00)**	**0.34 (0.01)**	**1.0 (0.0)**	**3.2 (0.1)**	**8.7 (0.2)**	**23 (1)**	**60 (2)**	**155 (4)**

originate from generator level cuts in Monte Carlo. However, no such discrepancy should remain after cut 8 if the Monte Carlo is representative of the background rates in data. The discrepancy following cut 8 is mainly due to the fact that most of the background events in this analysis contain jets that are faking photons. Monte Carlo samples followed by simulations of detector response do not accurately predict these fake rates. Therefore, in order to obtain a good exclusion limit, a data driven way of determining this fake rate is required. The data driven method used to determine the expected number of background Standard Model events will be described in chapter 9.

Monte Carlo background samples were still used to cross check the validity of the data driven method. In order to accomplish this, the Monte Carlo samples were scaled so that they could be more representative of the background composition in data. After cut 8, the data/MC ratio is 0.203±0.002. Table 8.9 shows the expected number of background events for different Standard Model MC samples. As can be seen, the background following cut 8 is dominated by dijets by a fraction of 97%. The data/MC scale factor has been applied to the dijet Monte Carlo samples after cut 8 in table 8.9 in order to provide a more probable description of the background composition. The cut flow for all Monte Carlo UED signal samples is summarized in table 8.10. The percentage of events surviving all the cuts tends to increase as the compactification radius of the universal extra dimension, $1/R$, is increased. This is due to the fact that as $1/R$ increases the E_T^{miss} spectrum and the E_T of the leading photons becomes harder. One also notices that the percentage of events surviving all cuts for the pile-up and extra material samples are the same within statistical uncertainties.

The Monte Carlo studies of the background composition in the signal region indicate the dominance of W+X and $t\bar{t}$ backgrounds. These events mainly consist of an $e^{\pm}$ in the final state, which also include τ leptons decaying to an electron. The Monte Carlo backgrounds that contain μ's in the final state are greatly reduced by the requirements relating to the existence of photons in the signal region. Prior to the E_T^{miss} cut, the

background is dominated by Monte Carlo dijets, $\gamma\gamma$ and γjet events, which motivates the importance of estimating their E_T^{miss} spectrum correctly.

Table 8.8: *Event selection cut flow for data, as well as for background MC (all samples as described in Section 8.2.2 and for UED signal MC (1/R=700 GeV/ℏc) normalized to the integrated luminosity of 3.1 pb^{-1}, with individual cut efficiencies. The 2.5 K-factors are applied to the $\gamma\gamma$ and γjet events.*

Cut	Data		Bgd MC		Signal MC	
	# of events	% effic.	# of events	% effic.	# of events	% effic.
No Cuts	193,883,454	-	3.36×10^8	-	8.68	-
1. Good Run	171,322,385	88.4	3.36×10^8	-	8.68	-
2. Trigger	4,737,963	2.77	2.63×10^7	7.82	8.66	99.7
3. Primary Vertex	4,686,624	98.9	2.62×10^7	99.6	8.55	98.7
4. Jet Cleaning	4,682,285	99.9	2.62×10^7	100	8.55	99.9
5. ≥ 2 Photons	1,946,834	41.6	5.76×10^6	22.0	8.33	97.4
6. η Cuts	1,224,358	62.9	5.06×10^6	87.8	6.76	81.2
7. $E_T^{\gamma 1,2} > 25$ GeV	10,683	0.87	51,240	0.01	6.23	92.2
8. Object Quality	9,232	86.4	45,400	88.6	5.39	86.5
9. Isolation	7,843	85.0	36,740	80.9	5.12	95.0
10. Loose Photon Id.	520	6.63	1,465	3.99	4.48	87.5
11. $E_T^{miss} > 75$ GeV	0	-	0.292	0.02	4.21	94.0

Table 8.9: *Event selection cut flow from cut 7 onwards, for different MC backgrounds (all samples described in Section 8.2.2) normalized to the integrated luminosity of 3.1 pb^{-1}. The number of dijet events has been corrected by the data/MC scale factor of 0.203±0.002 following cut 8. The 2.5 K-factors are applied to the $\gamma\gamma$ and γjet events. The purity, defined as the % of $\gamma\gamma + \gamma jet$ events is also given in the last column.*

Cuts	dijets	γjet	$\gamma\gamma$	W+X	Z+X	$t\bar{t}$	Total	% purity
7. $\mathbf{E}_T^{\gamma 1,2} > 25$ GeV	49,420	1,687	82.0	23.38	20.05	4.158	51,240	3.5
8. Object Quality	43,810	1,470	72.1	20.67	18.20	3.655	45,390	3.4
9. Isolation	7,146	1,427	72.1	16.08	15.67	2.497	8,686	17.3
10. Loose Photon Id.	204	378.6	69.3	2.538	8.138	0.138	663	67.6
11. $\mathbf{E}_T^{miss} > 75$ GeV	0.003	0	0	0.228	0.007	0.041	0.279	-

Table 8.10: *Expected number of UED signal events for 3.1 pb^{-1} and the selection efficiency after all cuts, for different $1/R$ values as well as for pile-up and extra material samples. The errors are statistical only and are omitted if negligible.*

UED Sample	# of Events	% Efficiency
$1/R = 300$ [GeV/$\hbar$c] (extra material)	603.5	27.13 ± 0.45 (26.85)
350	294.6	32.54 ± 0.47
400	142.1	35.62 ± 0.48
460	65.08	39.18 ± 0.49
500	40.45	42.61 ± 0.49
555	21.48	44.17 ± 0.50
600 (pile-up)	12.06	44.79 ± 0.50 (45.81)
650	7.207	45.67 ± 0.50
700 (pile-up)(extra material)	4.206	48.43 ± 0.50 (50.10)(47.05)
725	3.191	48.47 ± 0.50
750	2.492	48.35 ± 0.50
775	1.917	49.86 ± 0.50
800 (pile-up)	1.514	49.98 ± 0.50 (50.06)
900	0.577 ± 0.017	51.67 ± 0.50
1000 (extra material)	0.220 ± 0.017	53.17 ± 0.50 (52.69)

Chapter 9

Background Estimation

The large discrepancies between data and Monte Carlo highlighted in table 8.8 indicate that the Standard Model Monte Carlo does not give a reliable estimate of the background. The Monte Carlo samples have been utilized, however, in order to gain some insights into the composition and general behaviour of the Standard Model background. The overall composition and the final estimate for the number of background events in the signal region have been achieved using a data driven method. In section 8.2.2 the reducible background in the signal region was broadly categorized as arising from two contributions and the irreducible background was shown to be negligible for this study. The method used measured the contribution of the Standard Model background to the signal region. The reducible background, arising from instrumental effects, and the background from events with genuine E_T^{miss} is described in section **??**. The reducible background from events with genuine E_T^{miss}, where an electron fakes a photon, are underestimated in the initial treatment of section **??**. The method used to correct for this is discussed in section 9.2.

(a)

(b)

(c)

(d)
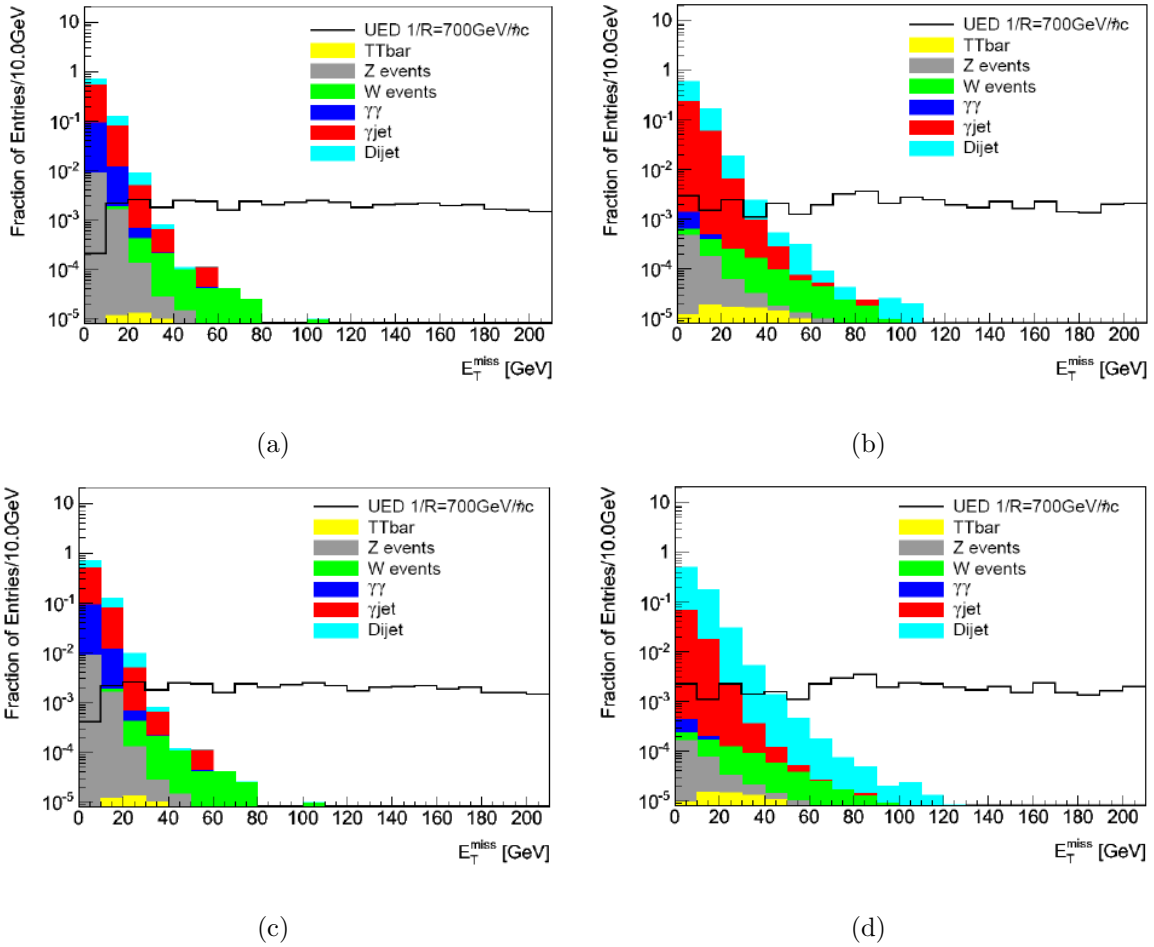
Figure 9.1: E_T^{miss} distribution for a) signal sample containing two loose isolated photons, b) Standard Model sample containing two isolated reconstructed photons in which at least one of the photons fails the loose identification criterion, c) signal sample containing two loose photons without the isolation criterion, and d) anti-loose sample containing two reconstructed photons without isolation criterion in which at least one of the photons fails the loose identification criterion. The distributions include all background Monte Carlo processes studied and the $1/R=700$ GeV/$\hbar c$ UED sample. The $\gamma\gamma$ and γjet samples have been scaled by a 2.5 K-factor and the dijet sample has been scaled by the data/MC ratio defined in section 8.4.3.

9.1 Estimation of Instrumental E_T^{miss}

Mismeasurement of the energy can lead to large apparent E_T^{miss}. This is possible if there is an energy mismeasurement associated with one or more of the main particles in the event, or if there are non-collision backgrounds overlapping with the measured event. Examples of energy mismeasurements include resolution effects or instrumental problems associated with dead or noisy cells. The main source of these instrumental E_T^{miss} backgrounds is from Standard Model $\gamma\gamma$, γjet, and multi-jet events. These sources include both hadronic and electromagnetic shower activity with differing energy scales, therefore their corresponding E_T^{miss} spectra are modelled using two different control samples. The control sample used to model the hadronic component is referred to as the "anti-loose sample" and is described in section 9.1.1, and that used to correct for the electromagnetic component is referred to as the "Z($\rightarrow ee$) control sample" and is described in section 9.1.2. The method used to combine these two samples is described in section 9.1.3.

9.1.1 anti-loose Control Sample for Hadronic Activity

Before applying the loose identification criterion to both of the reconstructed photons, the data sample consists of events in which there are two reconstructed isolated photons with $p_T > 25$GeV. This sample is then divided into two distinct sets; the signal sample consisting of two loose photons, and the anti-loose sample consisting of events in which at least one of the reconstructed photons has failed the loose identification criterion. Since the anti-loose sample has also passed the g20_loose criterion described in section 8.1, approximately 99% of these events contain only one photon which fails the loose identification cut. The anti-loose sample is the basic component of the control sample used to model the instrumental E_T^{miss} background spectrum in the signal region, in which at least one of the loose photons is associated with a hadronic jet. In order to ensure that this control sample is orthogonal to the W($\rightarrow e\nu$) control sample, which will be described

in section 9.2, an additional electron veto is also applied and will be described in this section.

Figures 9.1(b) and 9.1(d) show the expected SM background composition of the E_T^{miss} spectrum in Monte Carlo for the anti-loose sample with and without the isolation criterion respectively. These distributions can be compared to the corresponding signal samples in figures 9.1(a) and 9.1(c). The motivation for applying a very loose isolation criterion can be seen in these figures, the isolation criterion does not affect the background composition of the signal sample. This is because the loose identification criterion, with its focus on removing shower activity with large lateral spread, is very much correlated with an isolation requirement. Therefore calorimeter showers that pass the loose identification cuts are also very likely to pass the isolation cut. On the other hand, the anti-loose sample is sensitive to the isolation criterion on the reconstructed photons. Without the isolation cut, the anti-loose sample displays a harder E_T^{miss} spectrum with a tail dominated by events with wide hadronic showers that do not represent the background composition in the signal region. The isolation criterion, therefore, makes the anti-loose sample more representative of the jets in the background of the signal sample.

As mentioned previously, approximately 99% of the events in the anti-loose sample contain one reconstructed photon which has passed the loose identification criterion. This photon can be associated to a real photon, an electron or a hadronic jet faking a photon. The other reconstructed photon in the event which has failed the loose identification cut, on the other hand, is most likely a hadronic jet associated with a $\tau-$lepton or a parton. The unlikelihood of its association with a real photon is due to the expected high efficiency of 96% for the loose photon identification criterion. Furthermore, the loose identification cuts, which are designed to remove hadronic jets, will not remove an electron which has already been reconstructed as a photon candidate. In fact, the efficiency of the loose identification cut applied to an electron reconstructed as a photon is very similar to that associated with a real photon. For this reason, the anti-loose sample

underestimates the contribution from backgrounds consisting of a final state photon or electron from the hard scattering process. A comparison of figures 9.1(a) and 9.1(b) shows that the contributions from $\gamma\gamma$, γjet and $Z(\rightarrow ee)$ events are under-represented in the anti-loose sample. This contribution needs to be corrected for using a different control sample which will be described in section 9.1.2.

(a)   (b)
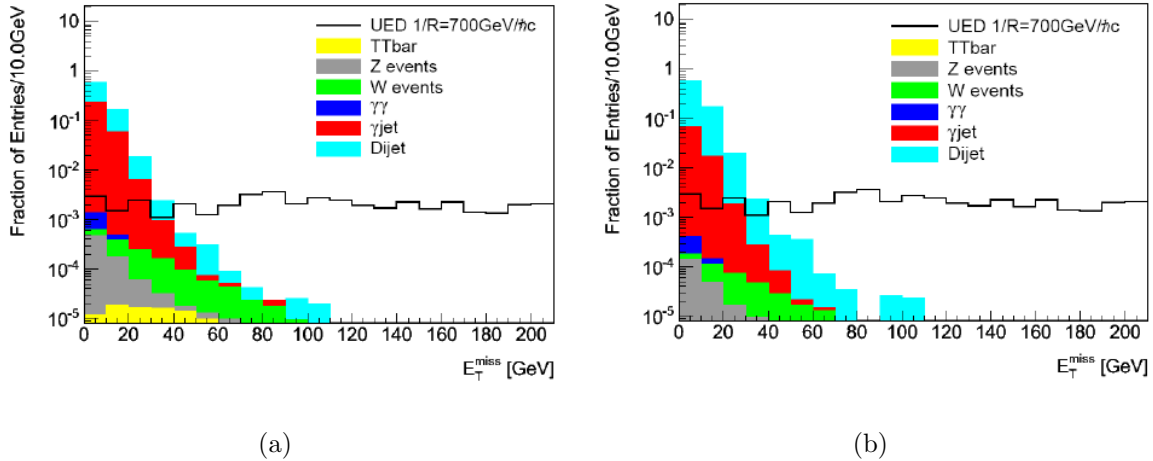
Figure 9.2: *Normalized E_T^{miss} distribution and background composition in the anti-loose sample without the electron veto criterion (a) and with electron veto (b). The distributions include all background Monte Carlo processes studied and the 1/R=700 GeV/ℏc UED sample. The $\gamma\gamma$ and γjet samples have been scaled by a 2.5 K-factor and the dijet sample has been scaled by the data/MC ratio defined in section 8.4.3.*

Monte Carlo studies show that, at high values of E_T^{miss}, the anti-loose sample also contains events with genuine E_T^{miss} containing final state neutrinos. The anti-loose sample is, therefore, also used to estimate the contribution of genuine E_T^{miss} events to the signal region. Comparisons between the fractional composition of the genuine E_T^{miss} component in the anti-loose sample and signal sample, show that the contribution from events involving a W boson decaying to an $e^{\pm}+\nu$ are underestimated in the anti-loose sample. To account for the $W(\rightarrow e\nu)$ contribution a separate method has been adopted and will be described in section 9.2. In order to eliminate the possibility of double counting, a separate electron

veto was applied to the anti-loose sample. This ensures that the anti-loose sample is or-
thogonal to the background control sample used to estimate the $W(\rightarrow e\nu)$ contribution.
The electron veto on the anti-loose sample removes events containing a tight electron
with $p_T > 20 GeV/c$ and $E_T^{miss} > 20 GeV$. An additional requirement for the existence
of a loose photon with $p_T > 25 GeV/c$, not overlapping with the identified electron, is
placed on this veto. In order to ensure that such events in the anti-loose sample are asso-
ciated with $W(\rightarrow e\nu)$ events, a further requirement on the transverse mass distribution
involving the identified electron and the E_T^{miss} defined by $40 GeV/c^2 < M_T < 100 GeV/c^2$
is applied. A more in depth discussion of these cuts is in section 9.2. Monte Carlo studies
show that this veto reduces the contribution from $t\bar{t}$ and $W(\rightarrow e\nu)$ events in the anti-
loose sample as shown in figure 9.2. This reduced composition is especially significant
for this analysis in the signal region where $E_T^{miss} > 75 GeV$.

The E_T^{miss} distribution of the anti-loose sample in data is presented in figure 9.3. There
are 7,323 events in this sample. The electron veto discussed above does not remove any
additional events. This suggests that the anti-loose sample in data was already orthogonal
to the $W(\rightarrow e\nu)$ sample which will be discussed in section 9.2. The anti-loose sample in
data contains 4 events in the region with $E_T^{miss} > 75 GeV$.

9.1.2 $Z(\rightarrow ee)$ Control Sample for Electromagnetic Energy

The background contributions due to electromagnetic energy deposited in the calorimeter
arises from $\gamma\gamma$, γjet and a small fraction of $Z(\rightarrow ee)$ events. The fractional composition of
this background is underestimated in the anti-loose sample compared to the signal sample.
In order to make the anti-loose sample more representative of the signal sample this must
be corrected for. To model the E_T^{miss} distribution from electromagnetic energy deposition,
a sample of $Z(\rightarrow ee)$ data events was used. The motivation for using $Z(\rightarrow ee)$ events
to correct for the electromagnetic energy leading in the instrumental E_T^{miss} background
is because it is easy to extract from data and contains E_T balanced events with isolated
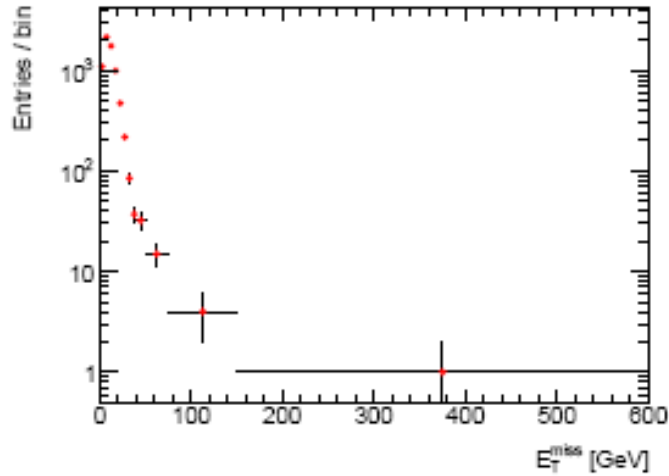
Figure 9.3: E_T^{miss} distribution for the anti-loose sample in 3.135 pb^{-1} of data [55].

EM clusters similar to the electromagnetic energy deposition that is being modeled.

The Z($\rightarrow ee$) events in data were selected by requiring two medium electrons with $p_T > 25$GeV/c with an isolation criterion similar to that placed on the photons and described in section 8.3. It was also required that the dielectron invariant mass fall in the range $66 < m_{ee} < 116$GeV. The medium identification criterion for electrons is described in [46] and includes all cuts described for the loose photon selection, described in section 7.3.2, followed by a set of cuts on the shower shape variables in the strip layers and the track quality. The strip layer cuts are applied to the variables w_{stotal} and E_{ratio} defined in section 7.3.2. The additional track quality criteria are designed to ensure that there is a sufficient number of hits associated with the matched track in the inner detector and that the EM cluster and track match well (i.e. $\Delta\eta$ between the electron track and cluster is < 0.01). The medium electron identification criterion has a 90% efficiency for isolated electrons and is expected to have a jet rejection factor of approximately 7000 [46]. This more stringent identification requirement on the electrons was appropriate for ensuring a pure sample of dielectron events. The additional cut on the dielectron invariant mass was chosen to contain the Z peak. The E_T^{miss} distribution

for this sample of data events is shown in figure 9.4. As can be seen, the E_T^{miss} distribution for this sample does not contain any events in the signal region with $E_T^{miss} > 75\text{GeV}$ and is, therefore, mainly used to scale the 4 events in the anti-loose sample that fall in the high E_T^{miss} signal search region.
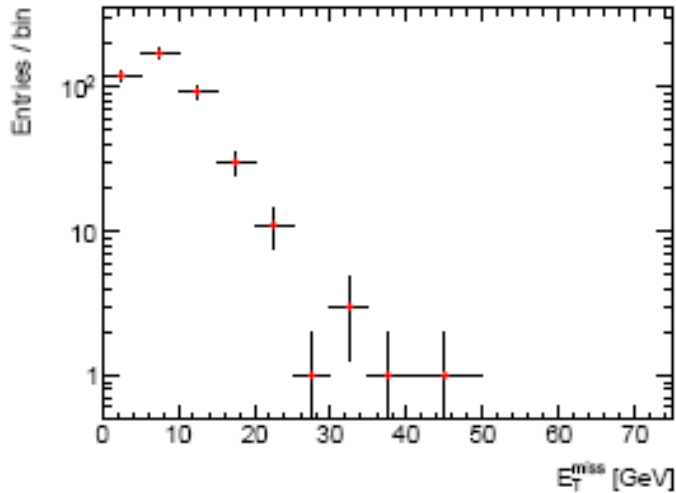
Figure 9.4: E_T^{miss} distribution for the Z($\rightarrow$ ee) sample in 3.135 pb^{-1} of data [55].

Monte Carlo studies were used to justify the use of Z($\rightarrow$ ee) events to model the background E_T^{miss} distribution arising from electromagnetic energy deposition. These Monte Carlo studies are summarized in figure 9.5, in which the electromagnetic instumental E_T^{miss} distributions in the signal sample are compared to that of the anti-loose and Monte Carlo Z($\rightarrow$ ee) events that have been selected using the same set of cuts that were applied to data. As can be seen the combined E_T^{miss} distribution of the $\gamma\gamma$, γjet and Z($\rightarrow$ ee) distributions in the signal sample (black) is slightly softer than that in the anti-loose sample (red). The inclusive Z($\rightarrow$ ee) E_T^{miss} distribution (blue) looks quite similar to the distribution in the signal sample (black).

Figure 9.5: *Normalized E_T^{miss} distributions in Monte Carlo for the combined $\gamma\gamma$, γjet and $Z(\to ee)$ contributions in the signal sample (black) and the anti-loose sample (red), along with the expected distribution for $Z(\to ee)+X$ events from Monte Carlo (blue).*
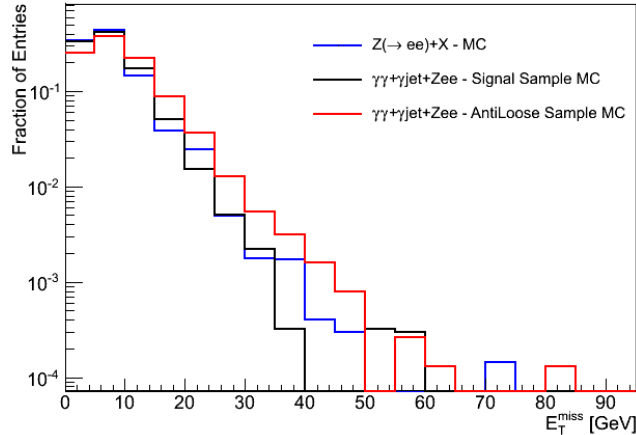
9.1.3 Combining the Instrumental Background Control Samples

The shapes of the normalized E_T^{miss} distributions for the anti-loose and electromagnetic control samples are compared in figure 9.6. The anti-loose control sample has a somewhat harder E_T^{miss} spectrum compared to the $Z(\to ee)$ control sample used to model the electromagnetic energy deposition. This is expected because the anti-loose sample is dominated by events with jets faking photons and should have worse calorimeter energy resolution than events dominated by electromagnetic energy depositions. Also superimposed in this figure is the E_T^{miss} spectrum for events in the signal sample in which both the isolated reconstructed photons have passed the loose identification criterion. The distribution for the signal sample lies between the two background control samples, harder than the $Z(\to ee)$ distribution and softer than the anti-loose sample, therefore the distribution of the signal sample can be described by an appropriate mixture of the two backgrounds.
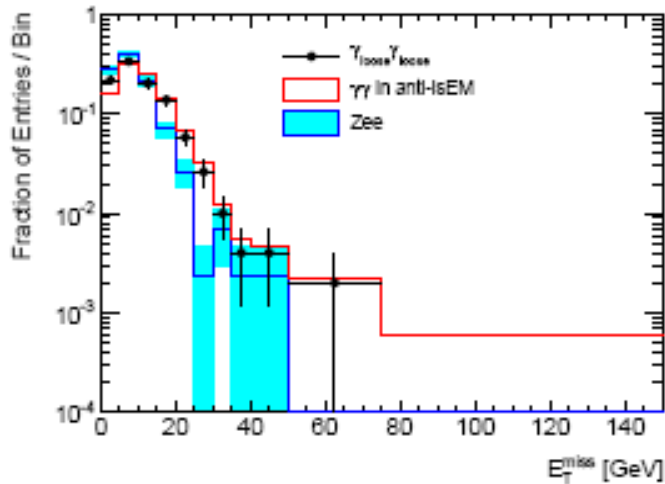
Figure 9.6: *Normalized E_T^{miss} distributions in 3.135 pb^{-1} of data for the anti-loose (red), $Z(\rightarrow ee)+X$ (blue) and the signal sample (points) [55].*

The low E_T^{miss} region defined as $E_T^{miss} < 20$GeV has been used to determine the relative contributions of these two control sample and to set the corresponding normalization. This region is dominated by events belonging to instrumental E_T^{miss} backgrounds. The contributions from events arising from genuine E_T^{miss} backgrounds or any possible UED signal is negligible in this low E_T^{miss} region. The weighted sum of the E_T^{miss} spectrum of the anti-loose and $Z(\rightarrow ee)$ control samples was normalized to the number of events in the $E_T^{miss} < 20$GeV region of the signal sample. In order to determine the relative weight of the two control samples a χ^2 test was employed, in which the measured deviation between the signal sample and the weighted sum of the two control samples in the region with $E_T^{miss} < 20$GeV was optimized in order to give the best agreement with data. The behavior of the χ^2 not only allows the determination of estimating the $Z(\rightarrow ee)$ fraction which gives the best agreement with data, but also provides an uncertainty for this estimation. The resulting value of the $Z(\rightarrow ee)$ fraction was determined to be 36±22% using this method. For the final background prediction, the central value of 36% was used and the error was treated as a systematic uncertainty.

Figure 9.7 shows the results of this procedure in Monte Carlo studies. Prior to this procedure the fractional composition of electromagnetic instrumental E_T^{miss} background is underestimated in the anti-loose sample as compared to the signal sample. The fraction of instrumental E_T^{miss} background from events with a photon or electron in the final state is estimated to be 69±4% of the total background in the signal sample. However, this fraction is only 39±2% in the anti-loose sample. When the χ^2 method described above is applied in Monte Carlo, the resulting value of the $Z(\to ee)$ fraction was determined to be 62±31%, which is higher than the fraction determined in data. This is, of course, expected because jets faking photons are not described accurately in Monte Carlo and do not model the dijet contribution, which results in a higher than expected background prediction for E_T balanced events with electromagnetic energy depositions. The compositional breakdown of the E_T^{miss} spectrum after combining the anti-loose and the $Z(\to ee)$ Monte Carlo samples resembles that of the signal sample as seen in figure 9.7. Furthermore, the overall fraction of instrumental background from electromagnetic activity in the combined anti-loose+$Z(\to ee)$ sample increases from 39±2% to 67±3% after this procedure, a number more representative of the compostition in the signal sample.

9.2 W($\to e\nu$) Control Sample for Background Events with Genuine $\mathbf{E}_T^{miss}$

Events involving a W boson decaying to an electron and neutrino are underestimated in the anti-loose+$Z(\to ee)$ sample described above. Such events can contribute to the background in the signal region if the electron is misidentified as a photon, and the second photon in the event is due to either a real photon in a W+γ event, or is faked by a jet in a W+jet event. The neutrino in the W($\to e\nu$) events will lead to a large genuine E_T^{miss} measurement and can potentially populate the high E_T^{miss} search region. This background is corrected for using data, by measuring the number of W($\to e\nu$)

(a)

(b)

(c)

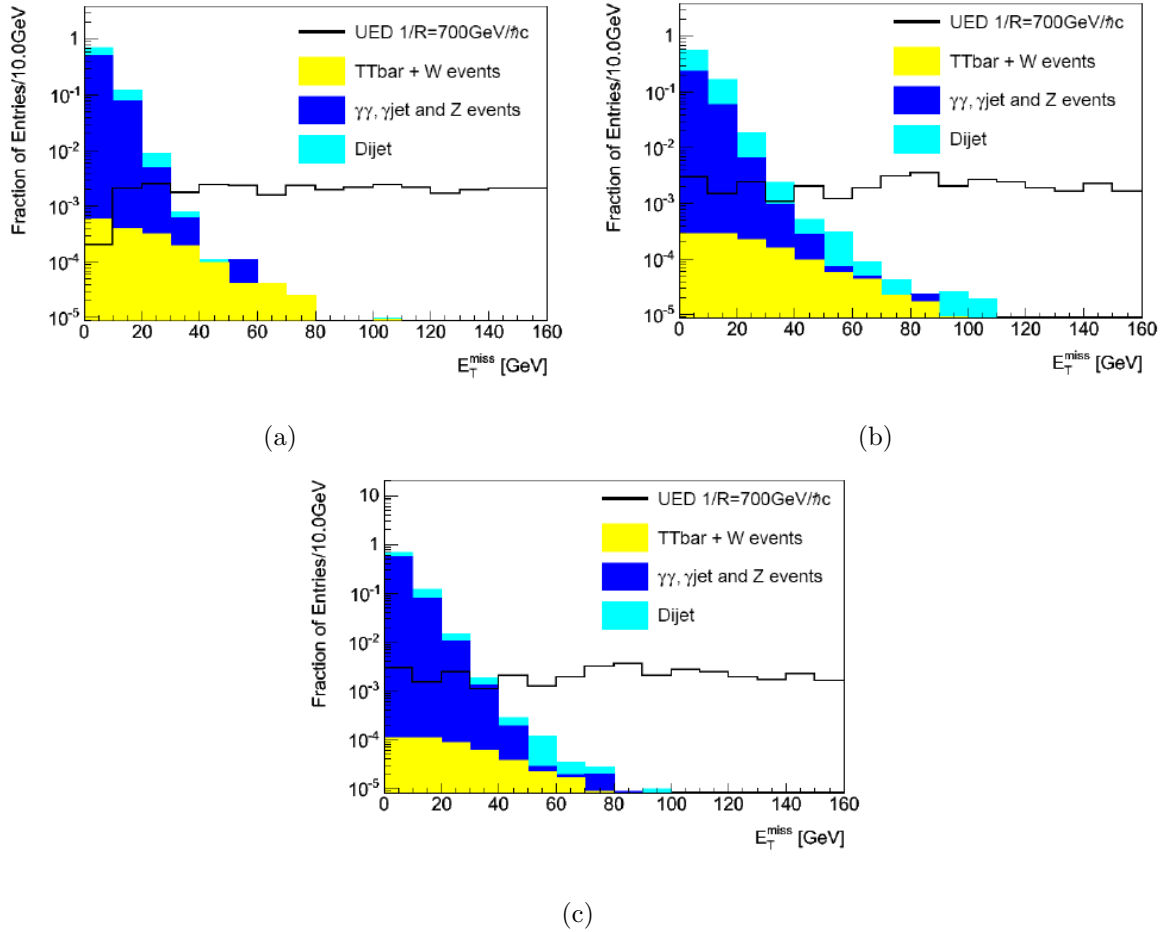Figure 9.7: *Normalized E_T^{miss} spectrum in MC signal sample (a), MC anti-loose sample (b) and the combined MC anti-loose+Z($\rightarrow$ ee) samples (c). These plots show the fractional background composition from events with genuine E_T^{miss} (yellow), purely hadronic instrumental E_T^{miss} (light blue) and instrumental E_T^{miss} from events with electromagnetic energy depositions (dark blue).*

events that also include a loose photon with $p_T > 25\text{GeV/c}$. The size of this sample is, however, very small. Therefore, the shape of the E_T^{miss} distribution is modeled using inclusive $W(\to e\nu)$ events normalized to the total number of $W+\gamma$ events and scaled by the probability for an electron to fake a loose photon.

A clean sample of $W(\to e\nu)$ events is selected by requiring a tight electron with $p_T > 20\text{GeV/c}$ and by applying a cut of > 20 GeV on the measured E_T^{miss}. The tight identification criterion for electrons is similar to that described for photons in section 7.3.2 and includes an additional set of cuts on the quality of its associated track. The E_T^{miss} cut is introduced in order to reduce any background contribution to this sample from E_T balanced events which have already been accounted for with the anti-loose+$Z(\to ee)$ sample. Figure 9.8(a) shows the transverse mass distribution for these events. The transverse mass is defined as follows:

$$M_T = \sqrt{2p_{T,e}E_T^{miss}(1 - \cos\theta)} \qquad (9.1)$$

where $p_{T,e}$ is the transverse momentum of the identified electron and θ is the polar angle between the electron and E_T^{miss}. As can be seen, the transverse mass distribution for these events contains a sharply falling peak at $M_T^{max} = M_w$ on top of a small background. Therefore, in order to reduce the contamination from backgrounds and to isolate a more pure sample of $W(\to e\nu)$ events, an additional cut, defined by $40 < M_T < 100 GeV$, is place on the transverse mass of the selected events. The E_T^{miss} spectrum for these events is shown in figure 9.8(b). The set of events collected thus far will be referred to as the inclusive $W(\to e\nu)$ sample and consists of approximately 7,000 events. After imposing an additional requirement that the event also contains a loose photon with $E_T > 25\text{GeV}$, which does not overlap with the electron candidate from the W decay ($\Delta R > 0.1$), only 5 events are left which will be referred to as the $W+\gamma$ sample. This sample is now completely orthogonal to the anti-loose sample with the electron veto.

In order to estimate the contribution of events with genuine E_T^{miss}, the $W+\gamma$ sample is scaled to estimate the size of a sample of similar events reconstructed as diphotons.
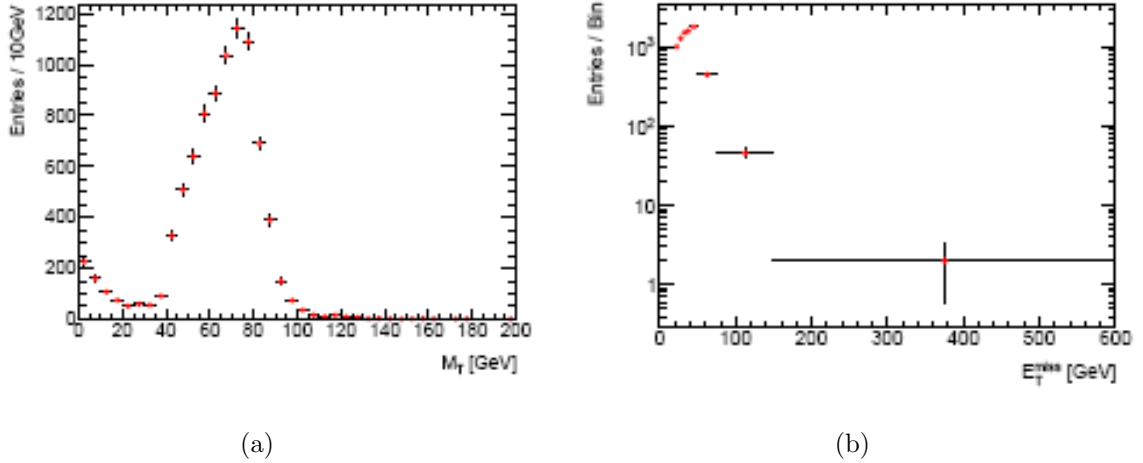
Figure 9.8: *The transverse mass distribution for data events with an identified tight electron with $p_T > 20\,GeV/c$ after requiring $E_T^{miss} > 20\,GeV$, for 3.1 pb^{-1} (a). The E_T^{miss} distribution for these events which are found in a $40 < M_T < 100\,GeV$ window (b) [55].*

This scale factor is not strictly a fake rate, but more a measure of the relative size of the W+γ sample to a similar sample where instead the electron was reconstructed as a loose photon. The scale factor s is measured from a background-subtracted tag-and-probe selection using Z($\rightarrow ee$) events described below and is defined by:

$$s = \frac{N_{pass-\gamma}/N_{probe}}{N_{pass-e}/N_{probe}} = \frac{N_{pass-\gamma}}{N_{pass-e}}, \tag{9.2}$$

where $N_{pass-\gamma}$ is the number of selected photon probe events that pass the loose identification criterion, N_{pass-e} is the number of selected electron probe events passing the tight identification criterion and N_{probe} is the total number of probe events.

This scale factor was measured using a sample of Z($\rightarrow ee$) events in 3.1pb^{-1} of data after applying the trigger and good run list criteria. Figure 9.9(a) shows the dielectron invariant mass distribution of tag-probe pairs, where both electrons must have $p_T > 20$GeV/c. The tag electron must satisfy the tight identification criterion for electrons, while the probe electron is just reconstructed as an electron. A clear Z peak is observed. Using a sideband technique to estimate the background, a total of 492.5±28.9 events are found in the peak region between 75 and 105 GeV. The number of such events reduces to

407.6±20.7 if the probe electron is required to also pass the tight identification criterion. The invariant mass distribution for these events is shown in figure 9.9(b) and this number represents our measure of N_{pass-e}.
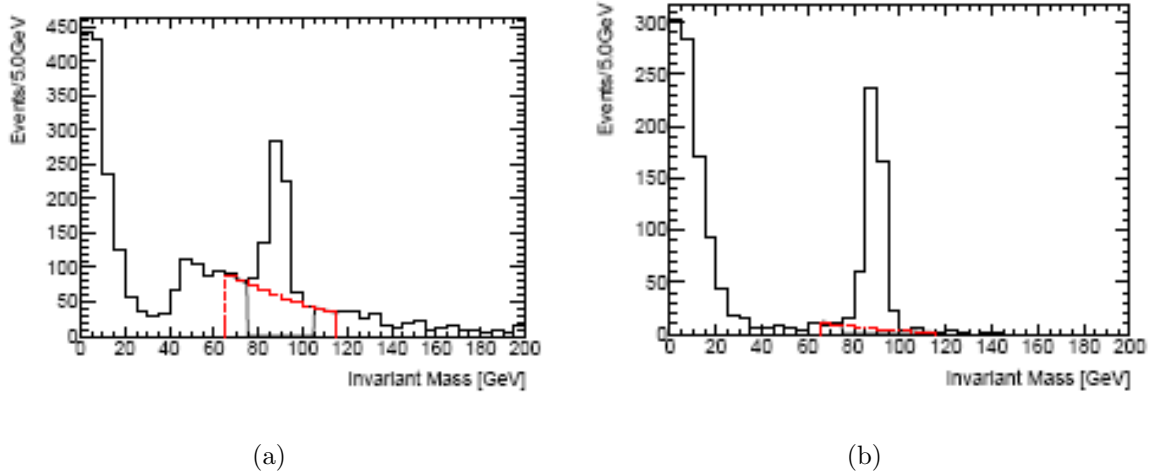

(a)   (b)

Figure 9.9: *The dielectron invariant mass distribution of tag-probe pairs, where both electrons must have $p_T > 20\,GeV/c$. The tag must be a tight electron. The probe electron must be a reconstructed electron (a) or a tight electron as well (b) [55].*

Figure 9.10 shows the electron-photon invariant mass distribution for events selected with a tight tag electron, but with the probe chosen to be a loose photon candidate. Again, a clear peak is seen at the Z mass, demonstrating that the loose photon candidates are, in fact, misidentified electrons faking a the loose photon signature. After background subtraction, a total of 31.5±6.8 events are found in the e-γ mass peak and this number is a measure of $N_{pass-\gamma}$.

A prediction of the E_T^{miss} spectrum for W($\rightarrow e\nu$) events in the signal sample is obtained by normalizing the inclusive W($\rightarrow e\nu$) sample in figure 9.8(b) to the five events measured in the W+γ sample and scaling it down by 31.5/407.6, the ratio of the number of e/γ events in the Z peak versus the number of e/e_{tight} events in the Z peak. This procedure adds a total of 0.42±0.15 events to the background prediction in the signal sample. The large statistical uncertainty is due to the small size of the W+γ sample.
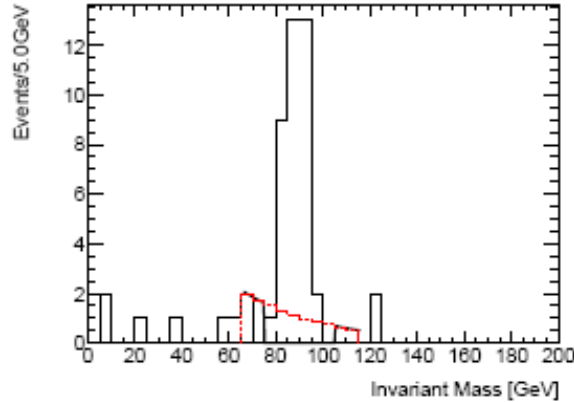
Figure 9.10: *The electron-photon invariant mass distribution of a tight tag electron and a probe chosen to be a loose photon, both with $p_T > 20\,GeV$ [55].*

Following a smiliar procedure with Monte Carlo shows that the predicted fractional composition of the genuine E_T^{miss} background is a good representation of that in the signal sample. Figure 9.11(a) shows the fractional background composition of events with genuine E_T^{miss} in the Monte Carlo signal sample. We can see that the $W(\to e\nu)$ and $W(\to \tau\nu)$ backgrounds dominate at higher values of E_T^{miss}. The same composition is shown in the anti-loose+$Z(\to ee)$ sample in figure 9.11(b). As can be seen the contribution from backgrounds with genuine E_T^{miss} is almost a factor of 10 smaller in the anti-loose+$Z(\to ee)$ sample as compared to the signal sample. Once the scaled down $W(\to e\nu)$ sample is added to the anti-loose+$Z(\to ee)$ background estimation, as shown in figure 9.11(c), the relative scale of the predicted genuine E_T^{miss} background and composition becomes much more representative of that in the signal sample. However, the genuine E_T^{miss} contribution measured with this method does tend to underestimate the contributions from events involving a τ lepton in the final state because they fail the transverse mass cut. This discrepancy tends to result in an underestimation of the expected background from genuine E_T^{miss} in the search region (ie. $E_T^{miss} > 75$GeV) of 30% as compared to the signal sample. This discrepancy has been considered as a systematic uncertainty.
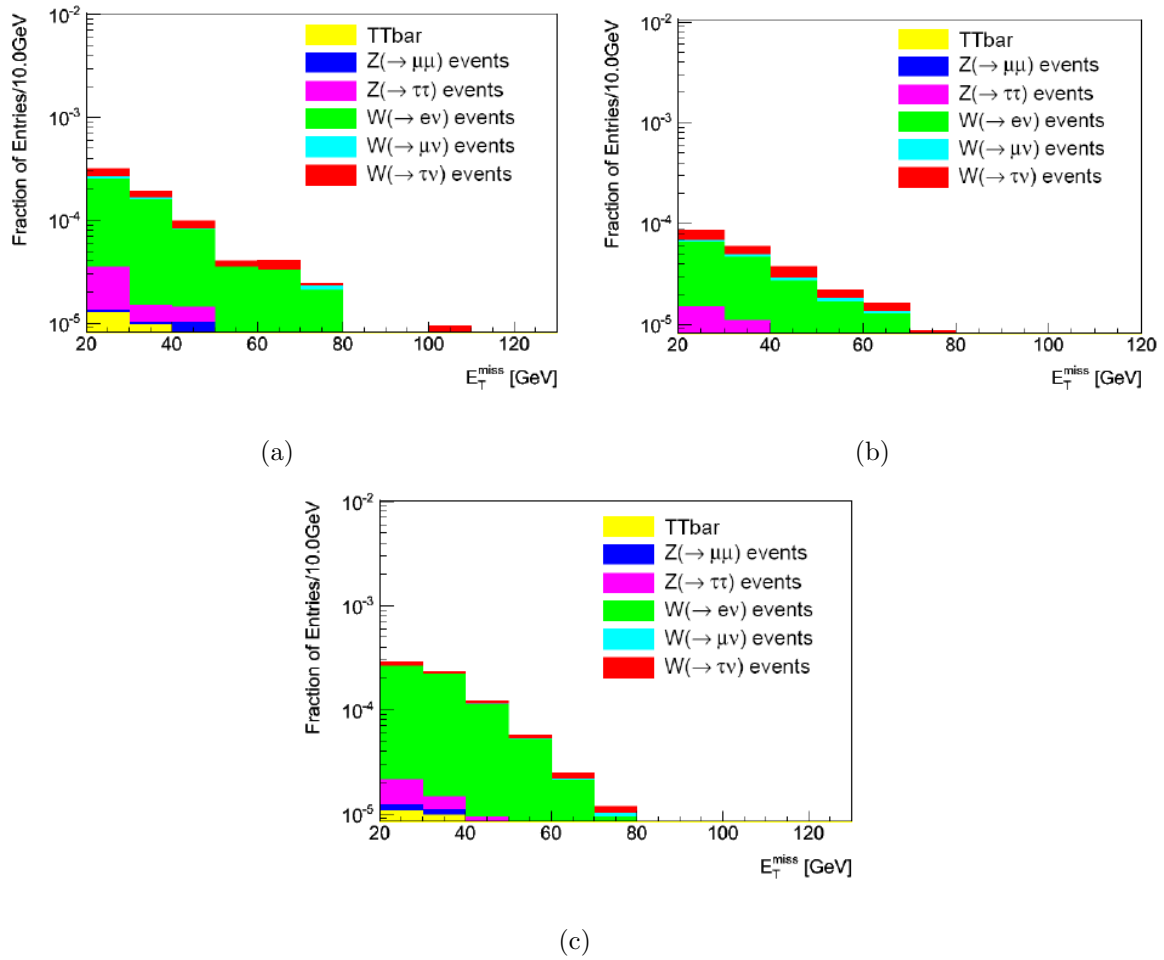
(a)

(b)

(c)

Figure 9.11: *The fractional Monte Carlo background composition of events with genuine E_T^{miss} in the signal sample (a), the anti-loose+Z($\to$ ee) sample (b), and the antiloose+Z($\to$ ee)+W($\to$ eν) sample (c).*

However, the overall statistical uncertainties in the search region are so large that they make this contribution negligible.

9.3   Final Background Estimation

The composition of the background in the signal sample is shown in figure 9.12(a). This plot shows the overall E_T^{miss} distributions from the anti-loose (brown) and $Z(\to ee)$ (green) backgrounds normalized to the data for $E_T^{miss} < 20$GeV. Also included is the predicted E_T^{miss} distribution from the $W(\to e\nu)$ (blue) sample. The E_T^{miss} distribution of the data collected in the signal sample is represented by black points. Figure 9.12(b) shows the total background prediction summing over these control samples (brown) as compared to the data collected in the signal sample (points). For comparison, the expected E_T^{miss} spectrum from UED signals with 1/R=500 GeV and 700 GeV have also been included. The UED signal would give a clear excess at high E_T^{miss} values. However, the total predicted background is in excellent agreement with the data in the signal sample over the entire E_T^{miss} range.

Table 9.1 summarizes the observed number of events, predicted background and expected UED signal contribution for 1/R=700 GeV, for various E_T^{miss} ranges. Also listed are the statistical errors on the predictions, as determined from the various data samples used to measure the backgrounds, or from Monte Carlo statistics in the case of the UED signal models. For the search region defined by $E_T^{miss} > 75$GeV, a total of 0.32±0.16(stat.) background events are expected, while no events are observed in data. The background is dominated by the scaled anti-loose sample with a very small contribution from the $W(\to e\nu)$ sample. The E_T^{miss} spectrum of the $Z(\to ee)$ sample which was used to correct for the underestimation of the $\gamma\gamma$ and γjet composition in the anti-loose sample does not contain any events beyond 45 GeV and, therefore, does not contribute to the background prediction in the signal search region. The purpose of the $Z(\to ee)$ sample was to
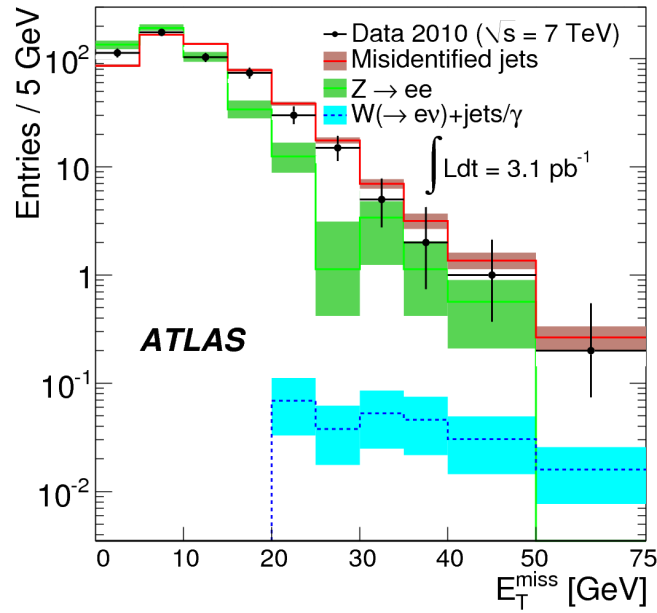
(a)
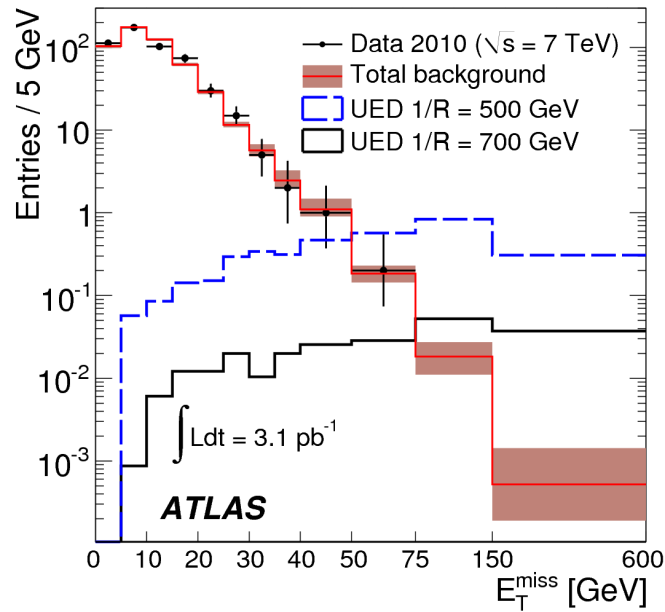
(b)

Figure 9.12: E_T^{miss} spectrum for data events in the signal sample (points), superimposed on the SM background distributions from the anti-loose (brown), $Z(\to ee)$ (green), and $W(\to e\nu)$ (blue) samples (a). The anti-loose and $Z(\to ee)$ backgrounds have been normalized to the $E_T^{miss} < 20\,GeV$ region in data. As well (b), the E_T^{miss} spectrum for data events in the signal sample (points), superimposed on the total SM background prediction (brown). Also shown are the expected UED signal contributions for $1/R=500\ GeV$ and $700\ GeV$ [35].

Table 9.1: *For various E_T^{miss} ranges, the number of observed data events as well as the expected SM backgrounds and expected UED signal for 1/R=700 GeV. The errors listed are statistical only. The first row, for $E_T^{miss} < 20$ GeV, is the control region used to normalize the anti-loose+Z($\to$ ee) prediction to the number of observed events in the signal sample.*

E_T^{miss} Range	Data	Predicted Background Events				Expected UED Signal
(GeV)	Events	Total	Anti-loose	Z	W	1/R=700 GeV
0 - 20	465	465.0 ± 9.1	297.1 ± 3.7	167.9 ± 8.3	0.0 ± 0.0	0.02 ± 0.00
20 - 30	45	40.5 ± 2.2	35.5 ± 1.3	4.9 ± 1.8	0.1 ± 0.1	0.03 ± 0.01
30 - 50	9	10.4 ± 1.3	8.2 ± 0.6	2.0 ± 1.2	0.2 ± 0.1	0.08 ± 0.01
50 - 75	1	0.92 ± 0.23	0.84 ± 0.22	0.00 ± 0.00	0.08 ± 0.05	0.14 ± 0.01
75+	0	0.32 ± 0.16	0.28 ± 0.16	0.00 ± 0.00	0.04 ± 0.03	4.21 ± 0.06

provide a mechanism by which the anti-loose sample could be scaled properly. Table 8.9 shows that the Monte Carlo expectation for the number of SM background events in the signal search region was $0.28^{+2}_{-0.1}$ (stat.), which when compared to the number estimated from the data driven background estimation method described in this section gives good agreement.

Chapter 10

Systematics

The systematic uncertainties associated with this analysis can be divided into two broad categories. In section 10.1 the systematics uncertainties associated with the acceptance of a UED signal are summarized. Section 10.2 outlines the systematic uncertainties arising from the data driven background estimation method described in chapter 9. Table 10.1 lists the sources of all systematics considered, and their associated uncertainties. The description of these systematics will focus on those associated with the 75GeV E_T^{miss} cut imposed on Monte Carlo UED signal events. The determination of the rest of the systematics that were specific to this analysis will be briefly summarized.

10.1 UED Signal Systematics

The expected acceptance of UED signal events is derived from Monte Carlo data following a GEANT4 simulation of the detector response. Uncertainties in this simulation could lead to uncertainties in the estimation of the expected signal acceptance. The main systematic that will be described in this section is that associated with the E_T^{miss} cut which defines the signal search region. Other systematics are listed in table 10.1 and the method used to estimate their contribution will be briefly summarized.

Source	Signal (%)								Background (%)
	$1/R[\text{GeV}/\hbar c]=300$	400	460	600	700	800	900	1000	
Luminosity	11								-
Photon reco+id	3.2								-
+Photon isolation	-								-
+Photon E_T	4	3	2	1	1	0.7	0.5	-	-
+Object Quality	0.9								-
=Sum Phot. Syst.	5.2	4.5	3.9	3.5	3.5	3.4	3.4	3.3	-
Pile-up	1.6								-
E_T^{miss} Cut	3.7	2.5	1.3	0.5	0.2	0.1	-	-	-
MC statistics	1.7	1.3	1.3	1.1	1	1	1	0.9	-
PDFs	8								-
Data driv. bgd. est.	-								+116/-31
Total (w.o pdf)	12.9	12.3	11.9	11.7	11.7	11.7	11.7	11.6	+116/-31
Total (with pdf)	15.2	14.7	14.3	14.2	14.2	14.2	14.2	14.1	+116/-31

Table 10.1: *Summary of individual systematic uncertainties (in %) assigned to signal and background acceptances, and the total, without and with the pdf uncertainty. The signal uncertainties are given for different 1/R values when necessary. The detailed photon systematic uncertainties are given as well as the sum of all of these. When not applicable or negligible, a "-" is placed in the entry.*

10.1.1 E_T^{miss} Resolution:

Calorimeter energy resolution summarized in section 6.4.3 will also affect any E_T^{miss} measurement or cut, since this variable is just the vector sum of the individual transverse energies of all the interacting particles in any given event. The E_T^{miss} resolution can be expressed as:

$$\sigma_{E_T^{miss}} = \sqrt{\Sigma_i (\Delta E_{T,i})^2} \qquad (10.1)$$

where the subscript i runs over all the particles in the event and $\Delta E_{T,i}$ is the energy resolution of each particle. If it is assumed that the stochastic term for hadronic activity dominates the contribution to this effect then:

$$\Delta E_{T,i} = a\sqrt{E_{T,i}} \qquad (10.2)$$

this implies that the E_T^{miss} resolution will to scale with ΣE_T as defined in equation 7.22. A quantitative evaluation of the E_T^{miss} performance was obtained by measuring the E_x^{miss} and E_y^{miss} resolutions as a function of ΣE_T [41]. The variables E_x^{miss} and E_y^{miss} are defined in equations 7.20 and 7.21 respectively. The resolution of these variables is determined by the width of the difference between the measured and expected $E_{x,y}^{miss}$ distributions for a collection of events in bins of ΣE_T. For the range of ΣE_T values that are of interest in this analysis, the stochastic term from hadronic activity dominates the contribution to the overall E_T^{miss} resolution. The resolutions increase proportionally with $\sqrt{\Sigma E_T}$ across most of the ΣE_T range, given by $\sigma = a\sqrt{\Sigma E_T}$. Deviations from this behaviour are present for small and large values of ΣE_T, where detector noise and energy mismeasurements associated with calibrations errors, mechanical imperfections etc. may respectively dominate. In data events it is not possible to know what the 'true' value of $E_{x,y}^{miss}$ is. However, for topologies such as dijet events in which there is no real E_T^{miss}, these distributions will peak around zero and the widths of the $E_{x,y}^{miss}$ distributions serve as a good estimate of the resolution. In order to obtain an estimate of the resolution in data events for the different event topologies which will be discussed in this section, only

the range of ΣE_T values in which Monte Carlo studies showed that events with genuine E_T^{miss} made up $< 1\%$ of the total background were considered.

The simulation of the ATLAS detector response for UED signal events already takes into account energy resolution effects. However, uncertainties in this resolution could lead to uncertainties in the acceptance of the signal search region defined by $E_T^{miss} > 75\text{GeV}$. The uncertainty associated with the E_T^{miss} resolution is estimated by measuring the difference between data and Monte Carlo. UED signal events either do not exist in data or, if they do, are few in number. To overcome this, the assumption is made that event topologies in Standard Model background events containing 2 loose isolated photons with $E_T > 25\text{GeV}$ have similar resolution to UED signal events. Such Standard Model topologies also suffer from limited statistics in data. Furthermore, similar background topologies in data span a lower ΣE_T range; ie. $\Sigma E_T < 350\text{GeV}$; while UED signal events generally have a higher ΣE_T; ie. $250 < \Sigma E_T < 800\text{GeV}$. Therefore, the measured resolution curve in data must be extrapolated to higher ΣE_T values in order to provide an estimate of the resolution uncertainty for UED signal events.

Figure 10.1(a) shows the $E_{x,y}^{miss}$ resolution curves versus ΣE_T for three different topologies in non-pileup data. Non-pileup events are those in which there is only one primary vertex candidate with more than 4 associated tracks. This cut provides a good separation between events with pileup and those without in Monte Carlo. The first topology, in red, is dijet events in which each jet has a measured $p_T > 25$ GeV/c and is within the same η acceptance as was imposed on the photon candidates in this analysis. The second topology, in purple, is events containing two reconstructed photons with $E_T > 25$ GeV. The third topology, in green, is events in which the leading photon passes the loose identification and isolation cut and has an $E_T > 25$ GeV, and the second leading photon in the event has an $E_T > 10$ GeV and passes 2 of the 4 loose identification cuts for photons, namely R_{had} and w_2 defined in section 7.3.2. The third topology is the closest one to the desired signal topology, and contains enough statistics to make a resolution

measurement possible. Figure 10.1(a) shows that at low ΣE_T, the resolution curves for all 3 topologies are approximately the same, but the dijet topology has more events, hence a more well-defined resolution curve that extends out to larger values of ΣE_T and can be extrapolated to even larger values more reliably. Therefore, in order to estimate the resolution in data for larger values of ΣE_T for topologies similar to UED signal events, the dijet events have been used. The E_T^{miss} resolution uncertainty was obtained by looking at the difference between the dijet topology in data and the Monte Carlo UED signal events. Figure 10.1(b) compares the resolution curves for dijets in data, in red, and UED signal events, in black. The difference between these 2 resolution curves over the ΣE_T range spanned by the UED signal events is on average 20%.

The effect of this resolution uncertainty on the acceptance of the 75 GeV E_T^{miss} cut in UED signal events was determined by shifting the $E_{x,y}^{miss}$ resolution in each UED signal event by 20%. Figure 10.2 summarizes the determined acceptance shift from resolution uncertainties as a function of 1/R. A 20% shift in resolution leads to a negligible, <0.2%, effect in the acceptance for a 75 GeV E_T^{miss} cut, and is independent of the UED signal 1/R value. The parametrization of the uncertainty as a function of 1/R is also included in the plot.

Due to the higher statistics in the 36pb^{-1} of data in the follow-up analysis [31], it was possible to measure the E_T^{miss} resolution in event topologies that were more similar to the UED signal topology. In that analysis, the resolution curve for data events containing two loose isolated photons with $E_T > 20\text{GeV}$ was compared to that from Monte Carlo UED signal events. Figure 10.3 compares these resolution curves. The E_T^{miss} resolution uncertainty decreased to 3% from the estimated 20% in the intial analysis [35].

10.1.2 E_T^{miss} Scale:

The energy response of the ATLAS calorimetry system is variable due to the utilization of different calorimeter technologies and the non-uniformity of the amount of dead material
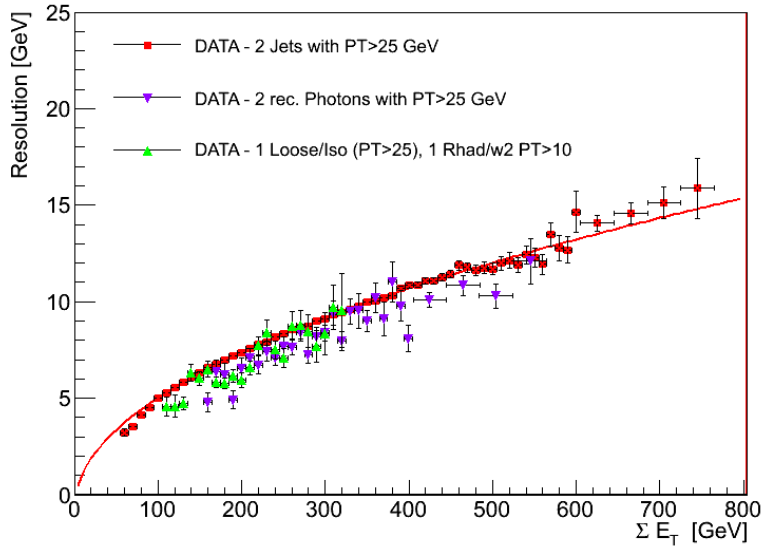
(a)
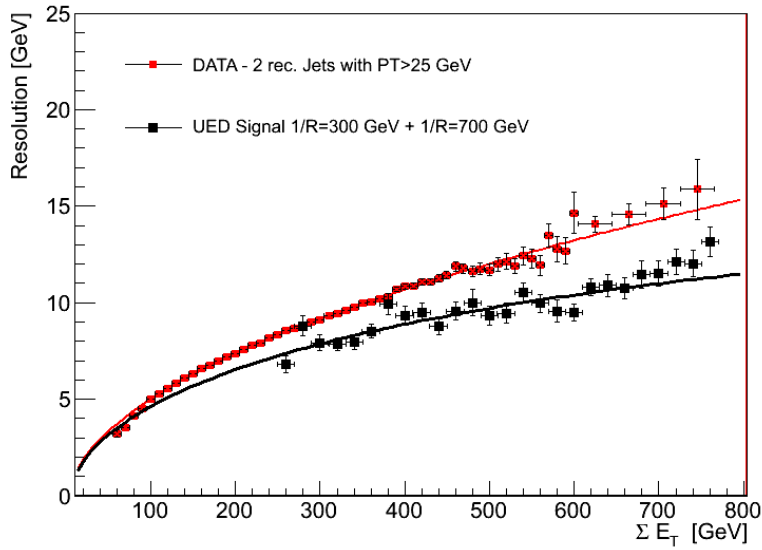
(b)

Figure 10.1: $E_{x,y}^{miss}$ resolution curves as a function of ΣE_T for different event topologies in data (a). All events have passed the trigger and cleaning cuts, in red are the events that also contained 2 jets with $p_T > 25 \, GeV/c$, in purple are events containing 2 reconstructed photons with $E_T > 25 \, GeV$, in green are events in which the leading photon passes the loose+isolation cuts and has $E_T > 25 \, GeV$, while the second leading photon has $E_T > 10 \, GeV$ and passes the R_{had} and w_2 photon identification cuts. $E_{x,y}^{miss}$ resolution curves for dijet events in data (red) and UED signal events in Monte Carlo (black) (b).
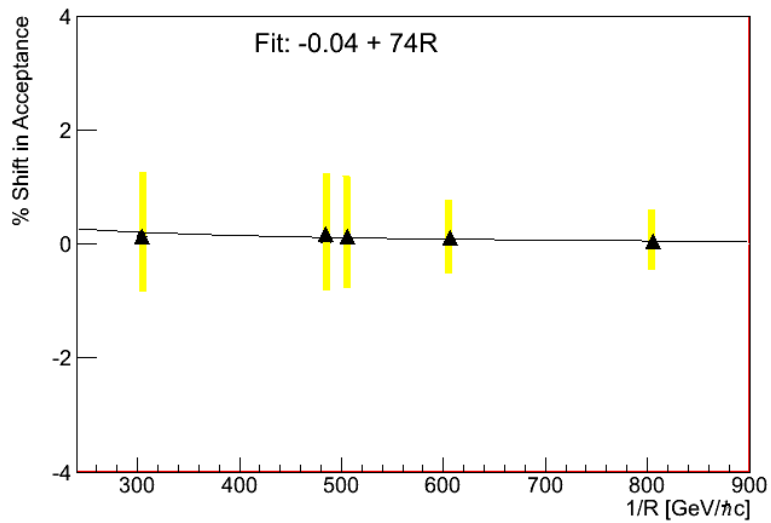
Figure 10.2: *Percent shift in $E_T^{miss} > 75$ GeV cut acceptance resulting from an E_T^{miss} resolution uncertainty of 20% in UED signal events as a function of 1/R.*

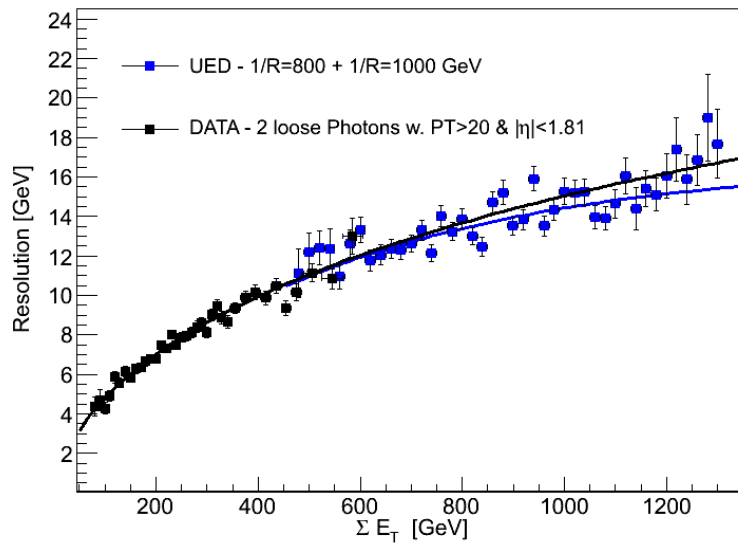Figure 10.3: *$E_{x,y}^{miss}$ resolution curves as a function of ΣE_T in $36pb^{-1}$ of data containing 2 loose isolated photons with $E_T > 20 GeV$ (black) versus that for Monte Carlo UED signal events (blue).*

in any given direction. The energy calibration applies an energy correction factor to ensure a uniform response across the whole detector, account for non-compensation effects in the hadronic response, and out of cluster energy depositions. These correction factors were derived from test beam response to electrons and pions and Monte Carlo simulations and have an associated uncertainty. Energy scale uncertainties for single particles affect the scale of the measured E_T^{miss} and lead to uncertainties in the acceptance of UED signal events in the search region.

Uncertainties in the E_T^{miss} scale were accounted for by following a modification of the method employed in [4] for the measurement of the W boson cross section. All topoclusters in a given UED signal event were initially divided into two categories, EM clusters and hadronic clusters. EM clusters, included all topoclusters that were within proximity $\Delta R < 0.1$ to a generator level photon associated with the decay of a γ^*, the lightest Kaluza Klein particle. These clusters are assumed to belong to an electromagnetic shower. All the remaining clusters in the event were considered to be hadronic. Figure 10.4(a) shows the E_T^{miss} distributions for EM clusters in blue and hadronic clusters in red for Monte Carlo UED signal events with $1/R$=700 GeV/$\hbar$c. The EM clusters from the decay of the lightest Kaluza Klein particle, γ^*, have a harder E_T^{miss} spectrum than those from hadronic clusters. Figure 10.4(b) shows the $\Delta\phi$ angle between the measured E_T^{miss} direction and that from EM clusters and hadronic clusters in red and blue respectively. These figures show that the EM clusters are collinear with the E_T^{miss} direction and make the most significant contribution to the measured value of E_T^{miss}. Therefore the higher uncertainties from jet energy scales will contribute less to the overall uncertainty of the E_T^{miss} energy scale.

The energy scale uncertainty assigned to EM clusters was 3% [3]. This was obtained by taking into account differences in the pulse shape reconstruction methods, calibration corrections, uncertainties in the liquid argon temperature and the time stability of the electromagnetic scale in the test beam and full ATLAS experiment. The hadronic clusters
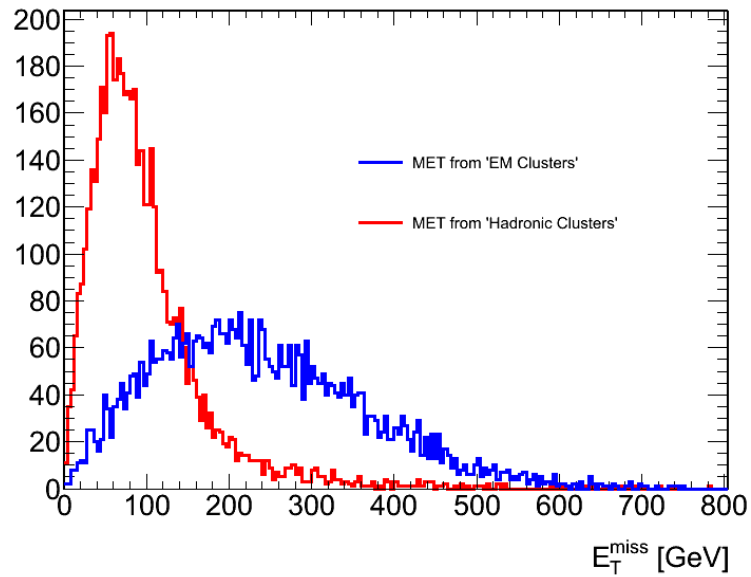
(a)
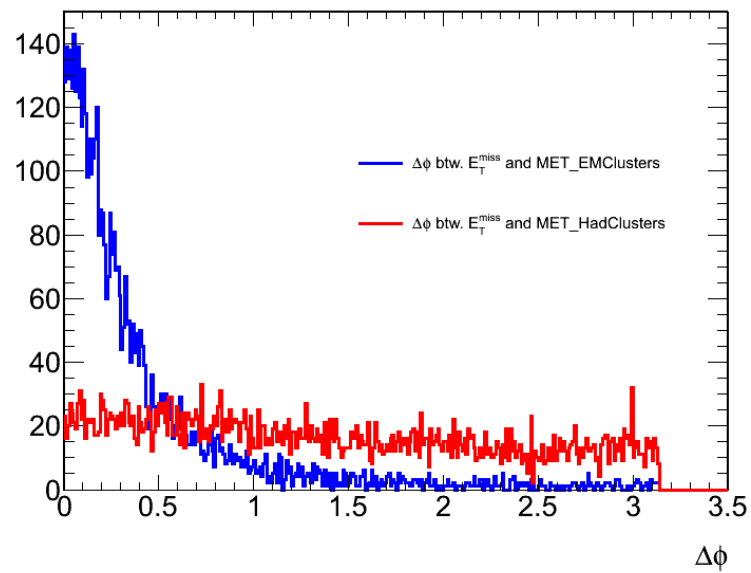
(b)

Figure 10.4: *The E_T^{miss} distributions of EM clusters (blue) and hadronic clusters (red) for Monte Carlo UED signal events with 1/R=700 GeV/ℏc (a). The $\Delta\phi$ angle between E_T^{miss} and the E_T^{miss} contribution from EM clusters (blue), hadronic clusters (red) for Monte Carlo UED signal events with 1/R=700 GeV/ℏc (b).*

are assigned a p_T (in GeV) and η-dependent energy scale uncertainty. In the central region, $|\eta| < 2.3$, the same uncertainties as those used in [4] are used in which the cluster energy scale uncertainties are derived from E/p studies [1] [2]. The E/p studies [1] used data versus Monte Carlo differences in calorimeter energy response E to an isolated track with momentum p using an integrated luminosity of 300 μb^{-1}. The energy E associated with a given track is obtained from all topoclusters within a cone of $\Delta R < 0.2$ around the track. The assumption is made that the track and its associated topoclusters belong to a single isolated charged hadron, and no special treatment is introduced for neutral hadrons. The data/MC E/p differences are sensitive to the hadronic energy scale uncertainties, due to the high precision track momentum measurements in the ATLAS inner detectors. Uncertainties in the topocluster energy scale, which are the main building blocks of the E_T^{miss} variable used in this analysis, arise from the noise suppression mechanism of the topoclustering algorithm which may cut some of the energy from signal. This error could be different for isolated and non-isolated particles, and is not properly accounted for in Monte Carlo simulations. Therefore, an uncertainty was assigned to the presence of this noise threshold by comparing the calorimeter response, E/p, from energy measurements from topoclusters and cells. The ratio between cluster and cell energies was determined to provide a conservative estimate of the uncertainty due to any possible bias from the clustering algorithm. Figure 10.5 shows the ratio of the relative calorimeter response for measurements made using topoclusters versus cells in two different η regions [1]. The difference between data and Monte Carlo simulation is at most $\pm 20\%$ for low p_T tracks (ie. $p_T \approx 500$MeV) and decreases to within $\pm 5\%$ at higher p_T values. The data/MC discrepancy was taken as the topocluster energy scale uncertainty and was parameterized as follows [4]:

$$\sigma_{Escale}(|\eta| < 2.3) = \pm 0.05(1 + \frac{1.5}{p_T}), \qquad (10.3)$$

where p_T is measured in GeV. For hadronic clusters with $2.3 < |\eta| < 3.2$, an additional

5% uncertainty is added in quadratures to the above. This is motivated by in-situ pseudo-rapidity inter-calibration studies using 17 nb^{-1} of colision data [2], which have measured a relative jet response uncertainty of 5% between jets in this η range, as compared to those in the central region. These measurements compare the transverse momenum of reference jets in the central region to those of a probe jet in the forward region, by assuming that these jets have equal p$_T$ due to transverse momentum conservation. The two leading jets in the event are required to be back to back in ϕ, $\Delta\phi(j_1, j_2) > 2.6$, and the third leading jet in the event is required to have a transverse momentum which is less than 25% of that of the leading jet in the event. This selection ensures 2→2 topology in which the assumption of equality between the transverse momenta of the two leading jets is valid. The topocluster energy scale uncertainty in the region defined by $2.3 < |\eta| < 3.2$ was parameterized as follows:

$$\sigma_{Escale}(2.3 < |\eta| < 3.2) = \pm\sqrt{(0.05(1 + \frac{1.5}{p_T}))^2 + 0.05^2} \qquad (10.4)$$

Using the same studies as above, an additional 15% uncertainty is added in quadrature with the uncertainties in the central region for hadronic clusters within $3.2 < |\eta| < 4.5$. The uncertainty assigned to these clusters is as follows:

$$\sigma_{Escale}(3.2 < |\eta| < 4.5) = \pm\sqrt{(0.05(1 + \frac{1.5}{p_T}))^2 + 0.15^2} \qquad (10.5)$$

In order to estimate the systematics associated with energy scale uncertainties, the energy of each topocluster was scaled in Monte Carlo UED samples and the effect on the cut acceptance was measured. Figure 10.6 summarizes the determined systematics from this effect in Monte Carlo UED signal events as a function of 1/R. The effect is small, ≈1-2%, for small 1/R signal events and is negligible for larger 1/R values. The fit and parametrization of the uncertainty as a function of 1/R is also included in figure 10.6.
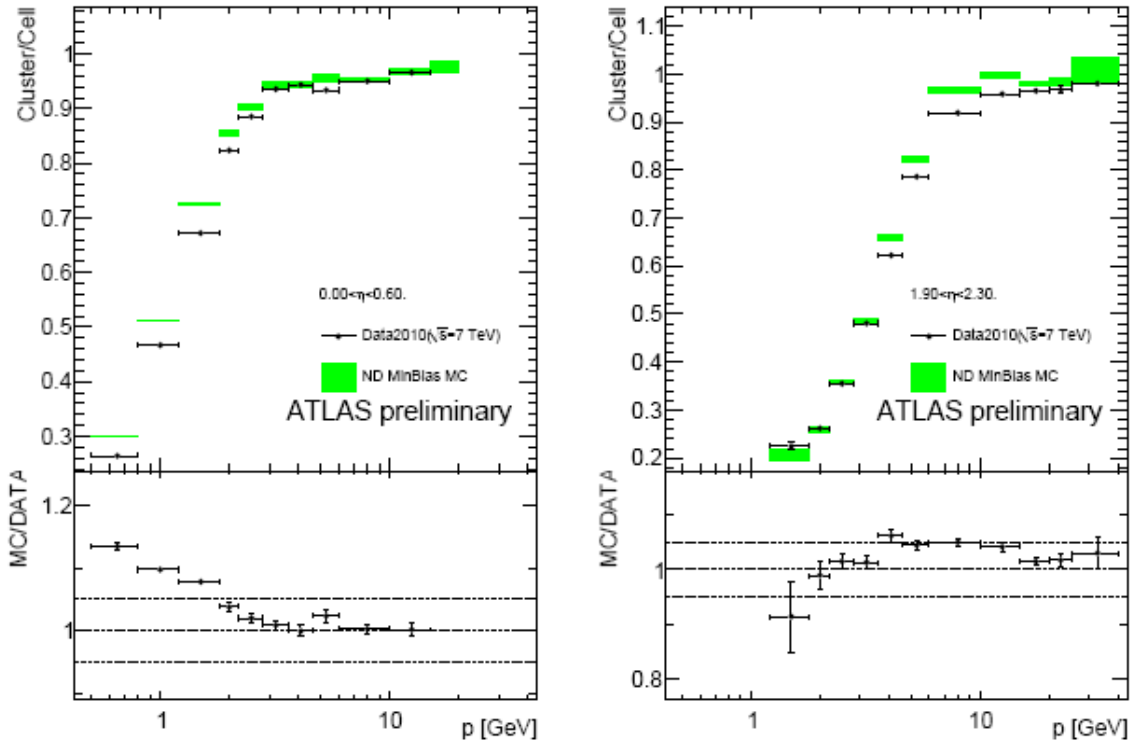
Figure 10.5: *Relative calorimeter response* $\langle (E_{cluster}/p)/(E_{cell}/p) \rangle$ *measured with clusters to that measured with cells as a function of the track momentum p in the central (0 < |η| < 0.6) and forward (1.9 < |η| < 2.3) region of the detector. The black dots represent the collision data, while the green rectangles represent the Monte Carlo prediction. The lower part of the figures shows the ratio between the Monte Carlo simulation prediction and collision data. The dotted lines are placed at ±5% of unity [1].*
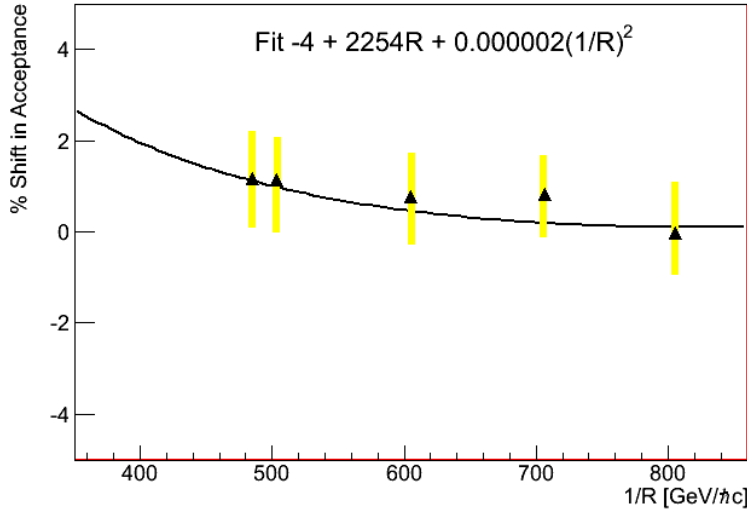
Figure 10.6: *Percent shift in $E_T^{miss} > 75$ GeV cut acceptance resulting from topocluster energy scale uncertainties in UED signal events as a function of 1/R.*

### 10.1.3 Pileup Effects on $\mathbf{E}_T^{miss}$:

In order to study the E_T^{miss} systematics associated with pileup effects, the data is divided into a pileup enriched and a non-pileup set. Pileup versus non-pileup Monte Carlo UED samples were used to verify that pileup events were unlikely to have a secondary primary vertex associated with more than 4 tracks. This requirement removes 99% of Monte Carlo UED events generated with pileup and only removes 1% of events without pileup. The pileup enriched set, therefore, includes all events with more than one primary vertex with ≥ 5 tracks. Approximately 50% of all events in data for this analysis were in the pileup set. This fraction remains constant within statistical uncertainties as each set of cuts is applied. Figure 10.7 shows the E_T^{miss} distributions for pileup and non-pileup events in the signal region 10.7(a) and anti-loose region 10.7(b) in data. Pileup events have a harder E_T^{miss} spectrum than non-pileup events. Within statistical uncertainties, this behaviour has a negligible effect on the acceptance of UED signal events given a 75 GeV E_T^{miss} cut. The isolation requirement was also shown to reduce the difference in the

E_T^{miss} spectrum of these two sets, and more importantly cuts out many of the non-pileup events in the tails of the E_T^{miss} distribution.

One known consequence of the presence of pileup in data is its effect on the E_T^{miss} resolution. In order to associate a systematic error to this, the E_T^{miss} resolution in the dijet topology was studied. Figure 10.8 shows the ΣE_T distributions for dijet events in non-pileup (black) versus pileup (blue) events. Pileup events tend to have a shifted ΣE_T distribution compared to the non-pileup events. So, in order to measure the effect of pileup on E_T^{miss} resolution, the non-pileup curve was initially shifted in ΣE_T. The shifted non-pileup distribution (red) closely matches the pileup distribution. Figure 10.9 shows the resolution curves for non-pileup (red) versus pileup (blue) dijet events. The dashed red line in the figure represents the fit to the non-pileup resolution curve after applying the shift in ΣE_T. The average discrepancy between the shifted non-pileup resolution curve and the pileup curve in the ΣE_T range between 260-800 GeV is 11%. The effect of pileup on the E_T^{miss} resolution is, once again, estimated by shifting the resolution in Monte Carlo UED signal events by 11% and measuring the effect on the $E_T^{miss} > 75$GeV cut acceptance. This effect is negligible, <0.1%, for UED signal events.

10.1.4   Photon Reconstruction and Identification:

The UED signal search region is defined by events containing two loose isolated photons with $p_T > 25$GeV and $E_T^{miss} > 75$GeV. In this section the systematics errors from the loose photon identification cut applied to the two leading reconstructed photons are discussed. Figures 10.10 and 10.11 show the data and Monte Carlo distributions for all of the variables used for the loose photon identification criteria. There is poor agreement between data and Monte Carlo, especially for R_η and w_2, which is also observed in [34]. At the time of this analysis, the method used to account for these discrepancies involved measuring the difference between the central values of each shower shape variable as a function of photon E_T and η [15]. It was observed that the difference between data and
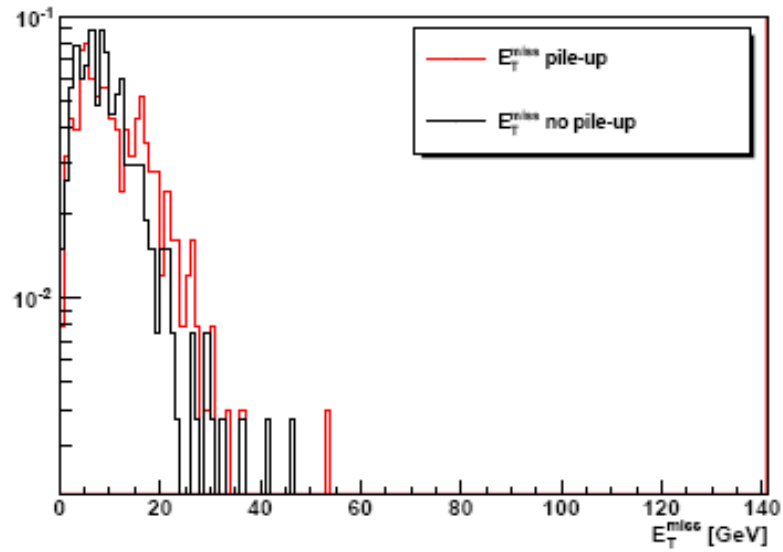
(a)
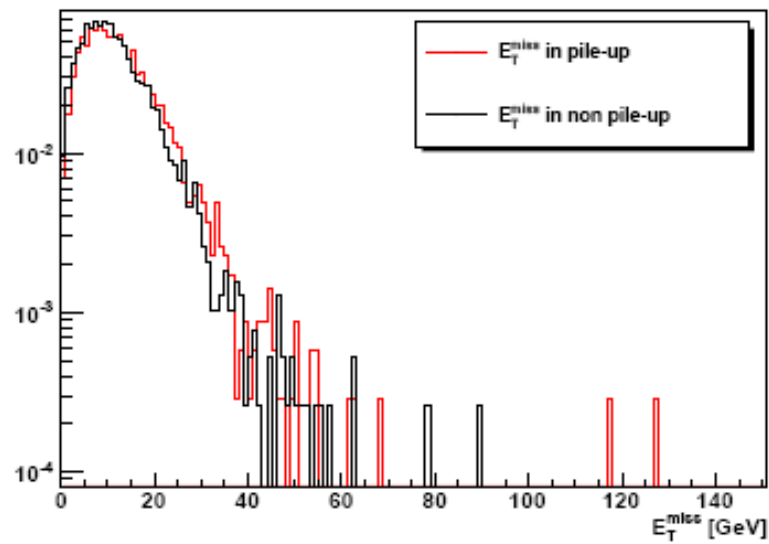
(b)

Figure 10.7: E_T^{miss} distributions for non-pileup (black) and pileup (red) data events in the signal region (a) and the anti-loose region (b). An outlier at 400 GeV is not included in the pileup (red) anti-loose plot (b).

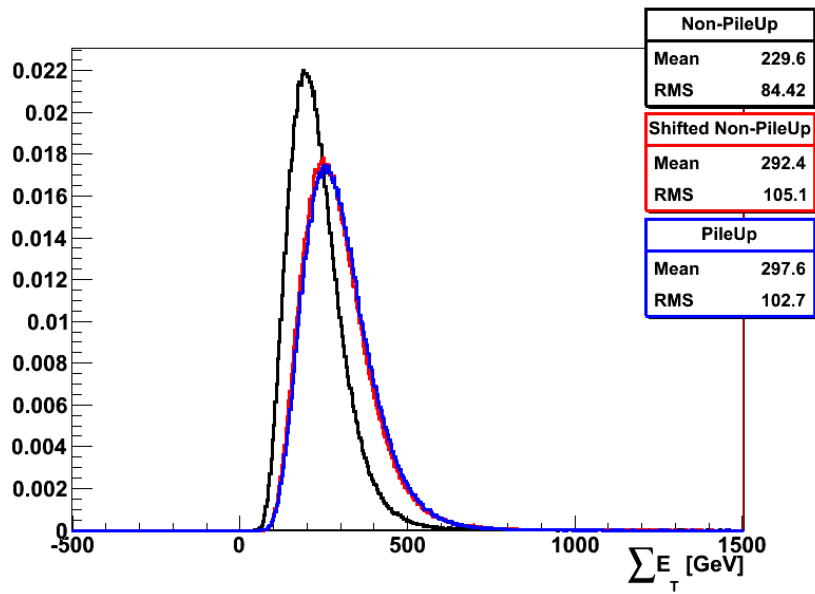Figure 10.8: ΣE_T distributions in dijet events, for non-pileup (black), pileup (blue) and shifted non-pileup events (red).
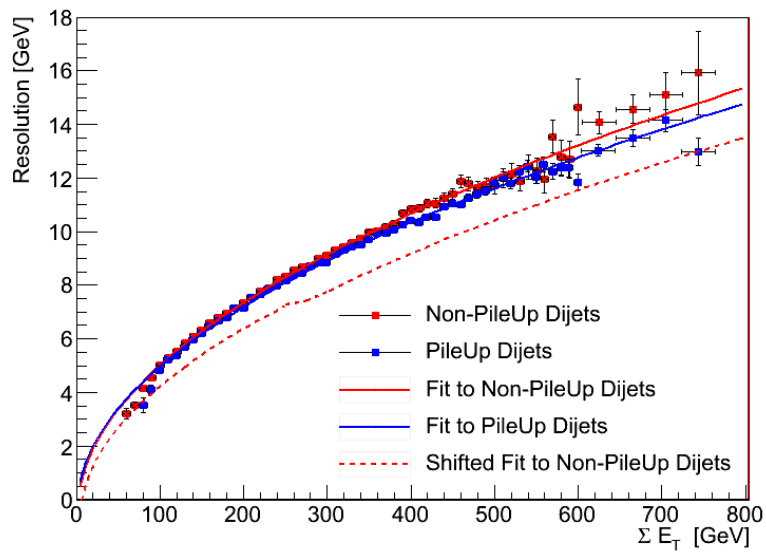

Figure 10.9: $E_{x,y}^{miss}$ resolution in data dijet events; non-pileup (red), pileup (blue), shifted non-pileup fit (dashed red).

Monte Carlo improved for smaller values of η and at higher photon E_T [15]. The photon shower shape variables in Monte Carlo were then corrected by these E_T and η dependent scale factors and the change in the selection efficiency was determined to be $\approx 1\%$. The photons studied in data, however, had limited statistics in the high E_T range of interest in this analysis. In order to extend this method to the UED analysis, the corrections were extrapolated to higher E_T values, the change in the identification efficiency was determined to be $\leq 1\%$, and the uncertainty associated with the extrapolation procedure was also determined to be 1% per photon. Added in quadrature, this led to a 1.4% uncertainty on the identification efficiency per photon. Assuming a 100% correlation for identifying 2 photons, this corresponds to a 2.8% uncertainty in the identification efficiency of 2 loose photons.

The effect of the uncertainty in the description of extra material in the ATLAS detector was also studied using dedicated UED Monte Carlo samples described in section 8.2.1. These samples were generated for 1/R values of 300, 700 and 1000 GeV/$\hbar c$ and included the addition of extra material to the inner detector, and calorimeters in the detector description. The change in the UED signal acceptance in the signal search region was on average found to be 1.4%. Combining this effect with that associated with the photon identification criterion resulted in the 3.2% quoted in table 10.1 for the systematic uncertainty attributed to the photon reconstruction and identification criteria.

10.1.5 Photon Isolation and E_T Cuts:

The data and Monte Carlo distributions for the photon E_T^{Cone20} variable defined in section 8.3 are compared in figure 10.12. The average relative difference between these two distributions was found to be $10\pm12\%$. This was taken to be the relative uncertainty on this variable. The effect of increasing or decreasing the isolation criterion of $E_T^{Cone20} < 35\text{GeV}$ was studied within these uncertainties for all UED signal samples and found to be negligible.
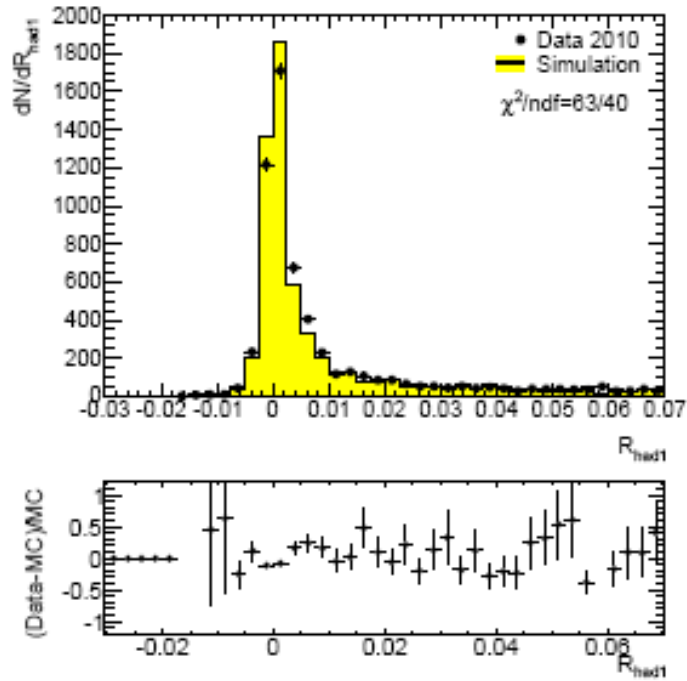
(a)
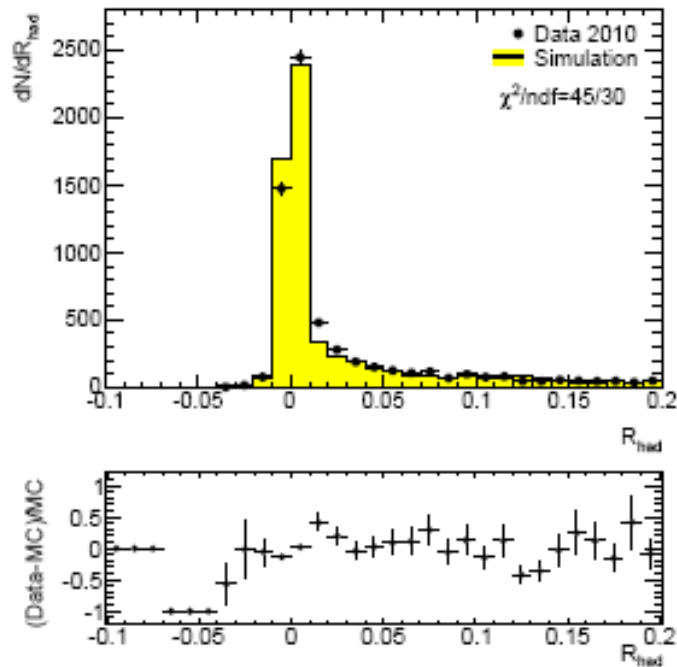
(b)

Figure 10.10: *Data and Monte Carlo distributions for R_{had1} (a) and R_{had} (b) after requiring the presence of 2 reconstructed photons with $p_T > 25 GeV$ in the event. The 2.5 K-factors are applied to the $\gamma\gamma$ and γjet events, and the dijets are weighted using the data/MC scale factor. The Monte Carlo is normalized to the number of data events. The (data - MC)/MC distributions are also shown below.*
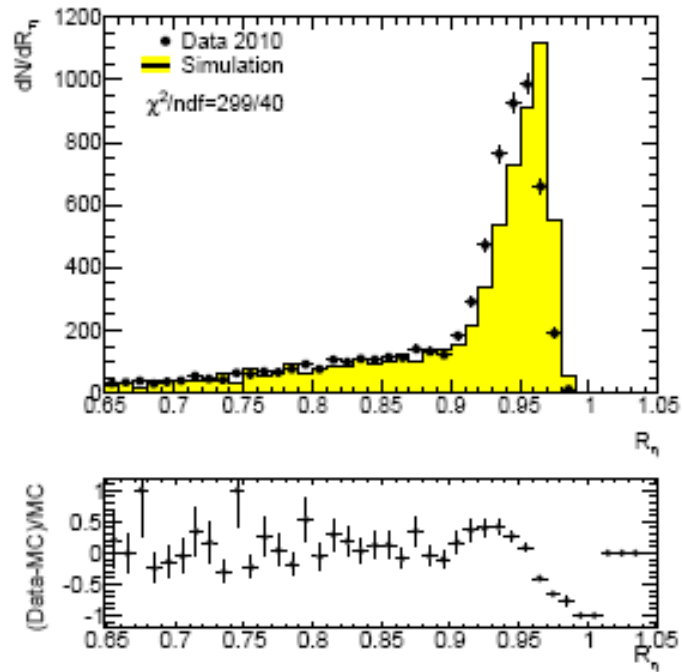
(a)
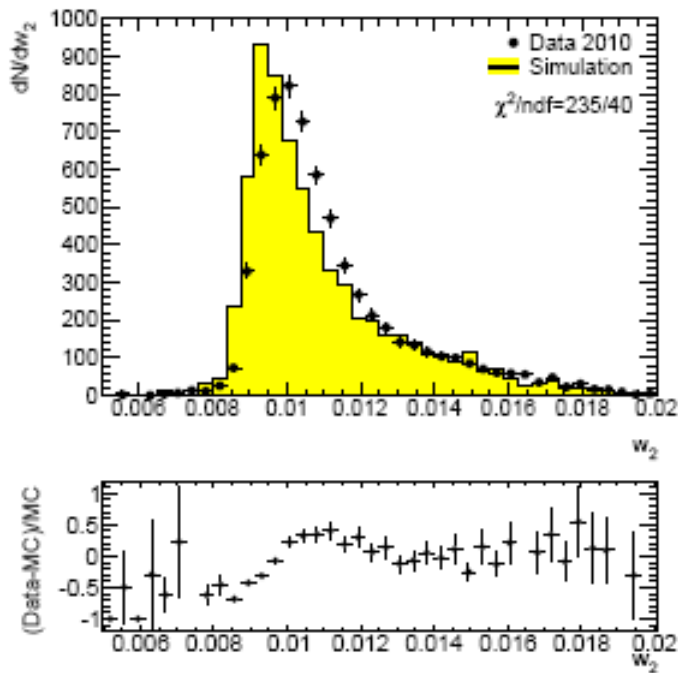
(b)

Figure 10.11: *Data and Monte Carlo distributions for R_η (a) and w_2 (b) after requiring the presence of 2 reconstructed photons with $p_T > 25\,GeV$ in the event. The 2.5 K-factors are applied to the $\gamma\gamma$ and γjet events, and the dijets are weighted using the data/MC scale factor. The Monte Carlo is normalized to the number of data events. The (data - MC)/MC distributions are also shown below.*

Figure 10.12: *Data and Monte Carlo distributions for E_T^{Cone20} after requiring two reconstructed photons with $E_T > 25\,GeV$. The 2.5 K-factors are applied to the $\gamma\gamma$ and γjet events, and the dijets are weighted using the data/MC scale factor. The Monte Carlo is normalized to the number of data events. The (data - MC)/MC distributions are also shown below.*
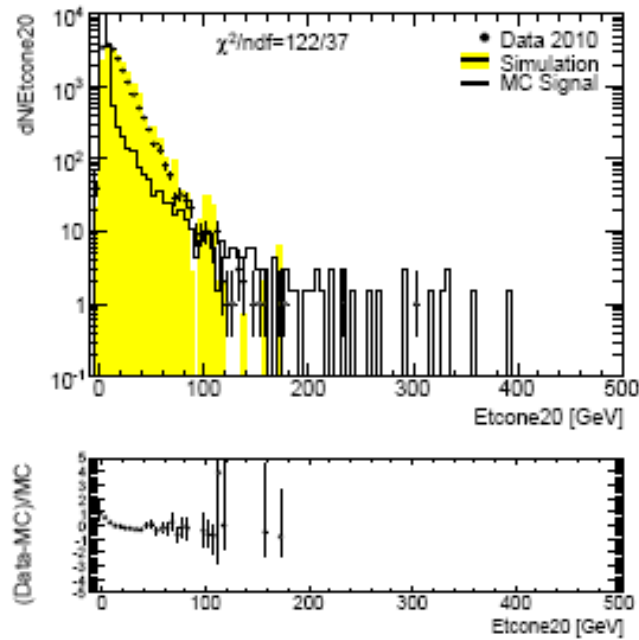
Figure 10.13 shows the data and Monte Carlo E_T distributions for the leading and second leading reconstructed photon in the event. The relative difference between data and Monte Carlo was on average found to be 4±8% for the leading photon in the event, and 5±10% for the second leading photon in the event. The E_T cut on the two leading reconstructed photons in the signal UED events was shifted by these uncertainties and the effect on the UED signal acceptance for different 1/R values is summarized in table 10.1. This effect on the UED signal acceptance tends to decrease for larger values of 1/R because the photon E_T distribution for these signal events becomes harder. This systematic uncertainty was checked for correlations with the 3% EM scale uncertainty already considered for the E_T^{miss} cut and was found to be negligible.

10.1.6   Photon Object Quality Cuts:

The photon quality cuts are described in section 8.4.1. Their purpose was to remove events in which either of the two leading photons had poorly reconstructed energy or E_T^{miss} due to the photons being in a problematic region of the calorimeter. The method used to estimate the systematic error due to this cut compared the efficiency of this cut between data and Monte Carlo using the nominal dead regions and control regions. The control regions have the same area and ϕ as the nominal dead regions, so it is possible to use the detector's ϕ symmetry to determine the effects on reconstruction around the borders of the nominal dead region. The basic idea is that any differences should arise from the edge regions where the energy, direction, and shower shape variables are affected by energy losses in the dead regions that have not been properly taken into account in simulated Monte Carlo data. This systematic error on the efficiency of this cut was determined to be 0.9%.
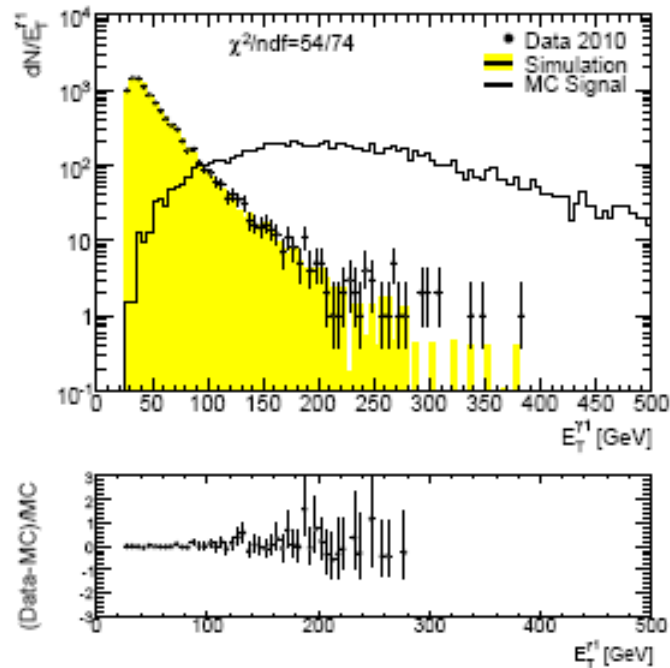
(a)
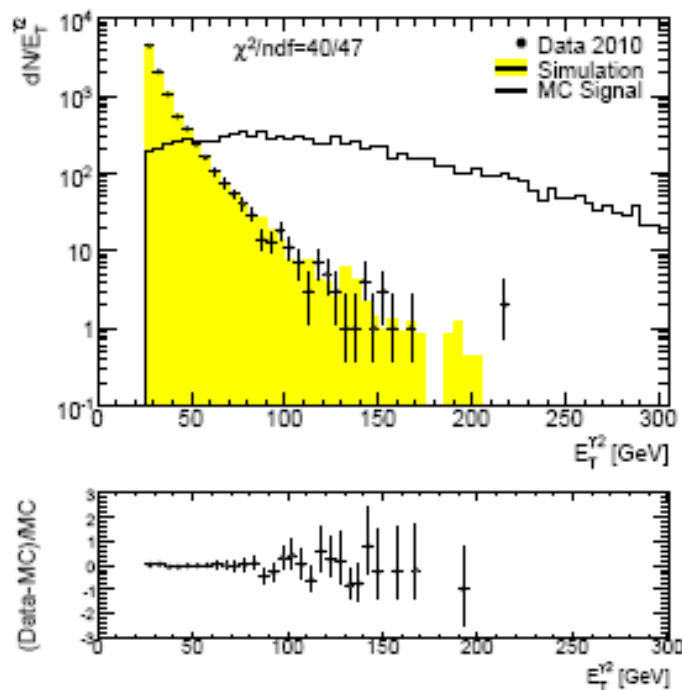
(b)

Figure 10.13: *Data and Monte Carlo distributions for the transverse energy of the leading photon, $E_T^{\gamma 1}$ (a) and that of the second leading photon, $E_T^{\gamma 2}$ (b), after requiring two reconstructed photons with $E_T > 25\,GeV$. The 2.5 K-factors are applied to the $\gamma\gamma$ and γjet events, and the dijets are weighted using the data/MC scale factor. The Monte Carlo is normalized to the number of data events. The (data - MC)/MC distributions are also shown below.*

10.1.7 PileUp

The effect of pileup on E_T^{miss} resolution was discussed in section 10.1.3, its effect on the efficiency associated with the photon isolation, E_T, and loose identification cuts was also be taken into account. These additional effects were also considered as a possible source of systematic uncertainty on the signal acceptance by using dedicated UED signal pileup samples described in section 8.2.1. The UED signal acceptance was determined to shift by an average of 1.6% with and without pileup.

10.2 Systematic Errors on the Background Estimation

Many cross checks were made to ensure the stability of the exclusion limit set on the UED compactification radius from the data-driven background estimation method. These variations included the use of the tight, as opposed to the loose, photon identification criterion to define the antiloose and signal regions, the removal of the isolation criterion, and other variations on the definition of the antiloose sample. The removal of the isolation criterion makes the E_T^{miss} distribution in the antiloose sample harder. The central value of the predicted number of Standard Model background events in the signal search region was found to be 0.32. This prediction remained stable within statistical uncertainties. Some of these variations and re-definitions of the background control samples were taken as a possible source of systematic uncertainty associated with the method used.

To estimate the systematic uncertainty on the predicted number of background events, the weight of the $Z(\to ee)$ control sample was varied within its fit error resulting in a shift of ± 0.10 events. The removal of the isolation criterion shifted the background prediction in the signal search region by $+0.37$. The redefinition of the antiloose control sample by requiring that either both photons fail the loose identification criterion or that only

one fails the loose identification criterion, shifts the predicted background by -0.08 and $+0.03$ respectively. The underestimation of the genuine E_T^{miss} contribution to the signal region from the background estimation method which was obtained from MC studies in section 9.2 is also considered as a possible source of systematic uncertainty suggesting a shift of $+0.1$ in the prediction of the central value. Since the removal of the isolation cut made the largest contribution to a positive shift in the central value, thereby making other positive shifts negligible, a systematic uncertainty of $+116\%$ was used on the predicted number of background events. The negative shifts in the predicted background arise from the variation of the weight of the $Z(\to ee)$ control sample within its fit uncertainties and the redefinition of the antiloose sample. In this scenario, the largest negative shift of -31% was considered as the systematic on this method.

Chapter 11

Discussion of Results

Zero events were observed in the signal search region defined by $E_T^{miss} > 75$ GeV. The E_T^{miss} spectrum derived using the data driven background estimation method described in section 9 was also found to be in good agreement with that of the signal region containing two loose isolated photons with $E_T > 25$ GeV. This agreement can be seen in figure 9.12 (right) and table 9.1. Given this good agreement, a limit was set on excess production of diphoton events with large E_T^{miss}.

These results were interpreted in the context of the UED model described in chapter 4 [35]. The expectations for the UED signal acceptance and their corresponding systematic uncertainties were determined using Monte Carlo and are summarized in tables 8.10 and 10.1 respectively. A Bayesian approach [43] was used to calculate the limit based on the number of observed and expected events with $E_T^{miss} > 75$ GeV. A Poisson distribution was used to describe the likelihood function for the expected number of observed events. The priors, referring to the distribution functions used to define the prior probability of a given parameter, were taken to be Gaussian for the signal efficiency, luminosity, and expected number of background events with the systematic and statistical uncertainties taken as the respective standard deviations. It was verified that the detailed form assumed for the priors did not affect the results. A flat prior was used

for the signal cross section. Since the primary interest was in the signal cross section, the luminosity, signal efficiency and the expected number of background events were all taken as nuisance parameters. Figure 11.1 shows the 95% CL upper limit obtained for the UED cross section as a function of $1/R$. This figure also shows the LO UED cross section as a function of $1/R$ along with the 8% uncertainty associated with the parton distribution functions depicted as a blue band and independent of the $1/R$ value. The LO cross sections were used because higher order cross sections were not calculated for this UED model.

For 3.1 pb^{-1}, UED models defined in chapter 4 with $1/R \leq 728$ GeV have been excluded with 95% CL. Neglecting all the systematic uncertainties only raised the upper limit of the excluded region to $1/R$=732 GeV, showing that the result is not sensitive to the systematic uncertainties. Changing the E$_T^{miss}$ cut to 60 (or 90) GeV resulted in a change of +2 (or -4) GeV on the set limit. The results were further cross checked against other selection criterion, such as changing the loose photon identification to tight, and were observed to be consistent with the quoted results. The upper limit on the number of signal events after all selection cuts was determined to be 3.12.

Prior to this study, the only existing experimental limit set on the universal dimensions model under investigation used the D0 detector at the Fermilab Tevatron Collider [53]. The search by the D0 collaboration used 6.3 fb^{-1} of $p\bar{p}$ collisions at $\sqrt{s} = 1.96$ TeV and the compactification radius of the UED models being considered in this analysis was excluded for $1/R < 477$ GeV. Our result significantly improves on this limit. With ten times the data, a lower limit of $1/R > 961$ GeV was set on the UED compactification radius R at 95% CL [31].

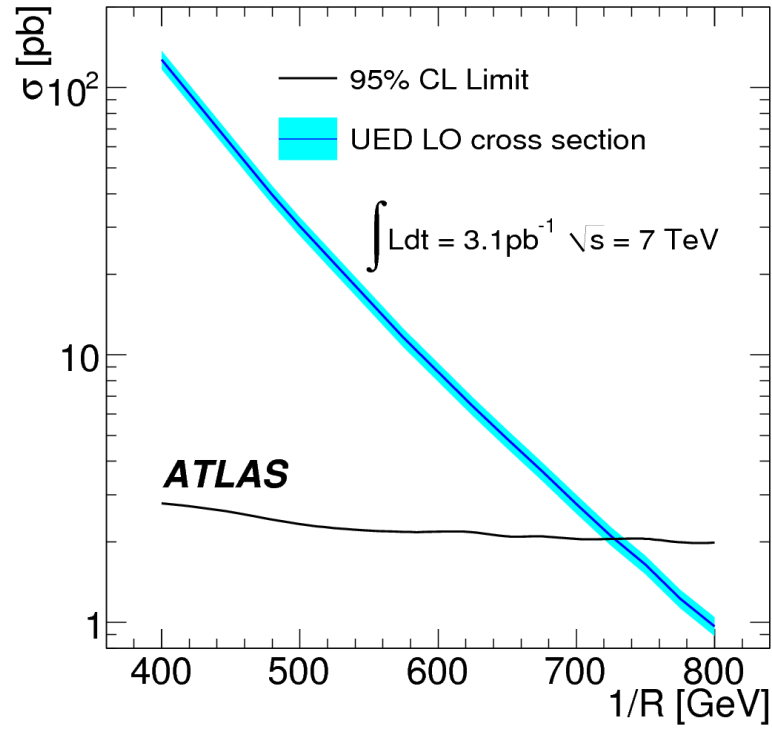Figure 11.1: *The 95% CL upper limits on the UED production cross section, and the LO theory cross section prediction, as a function of 1/R. The blue band shows the pdf uncertainty [35].*

Chapter 12

Conclusion

A search for diphoton events with large missing transverse energy produced in pp colli-sions at $\sqrt{s} = 7$ TeV has been presented. The data was collected by the ATLAS detector at the CERN Large Hadron Collider during the period between March 30, 2010 until August 30, 2010, and corresponds to 3.1 pb^{-1} of integrated luminosity. The missing transverse energy distribution for the Standard Model background in the signal search region, defined by events containing two loosely identified photons with p$_T$ > 25 GeV, has been modelled using a data driven method. The observed missing transverse energy distribution in the signal search region shows good agreement with the predicted back-ground. No excess events were observed in the signal search region, defined by E$_T^{miss}$ > 75 GeV. These results were interpreted in the context of a beyond the Standard Model the-ory. The theory considered was a Universal Extra Dimension (UED) model with gravity mediated decays with $\Lambda R = 20$, $N = 6$ and $M_D = 5$ TeV. The signal acceptance of the UED model was determined from Monte Carlo. This model was excluded for a UED compactification radius of $1/R < 728$ GeV at 95% CL.

This result significantly extended beyond the only exisiting experimental limit on this model from the D0 collaboration[53] at the Fermilab Tevatron Collider. The D0 analysis, used 6.3 fb^{-1} of integrated luminosity of p$\bar{p}$ collisions at $\sqrt{s} = 1.96$ TeV and set an upper

limit of 477 GeV on $1/R$.

This search has since been extended by the ATLAS collaboration to consider larger data samples corresponding to 36 pb^{-1} [31] and 1 fb^{-1} [36]. These extensions placed upper limits of 961 GeV and 1.23 TeV respectively on $1/R$. Both limits provided the most stringent tests of this model to date and included considerations of supersymmetric models as well. The exclusion limits did not scale to the same extent as the increase in integrated luminosity. One reason for this is that the UED cross-sections decrease exponentially as a function of $1/R$. Another reason is that for $1/R$ values up to 1 TeV, the branching ratio for the diphoton and E_T^{miss} final state is close to 100%. However, as $1/R$ increases beyond this value the gravitational decay widths become more important for all KK particles, not only the LKP, and the branching ratio into diphotons decreases. For example for $1/R = 1.5$ TeV, the branching ratio into diphotons is only 50%. These considerations show the significance of the first period of data taking at the LHC for setting exclusion limits on this model.

Bibliography

[1] ATLAS Calorimeter Response to Single Isolated Hadrons and Estimation of the Calorimeter Jet Scale Uncertainty. ATLAS-CONF-2010-052.

[2] In-situ pseudorapidity intercalibration to evaluate jet energy scale uncertainty and calorimeter performance in the forward region. ATLAS-CONF-2010-055.

[3] Jet energy scale and its systematic uncertainties for jets produced in proton-proton collisions at $\sqrt{s}$ =7 TeV and measured with the ATLAS detector. ATLAS-CONF-2010-056.

[4] Measurement of the W cross section and assymmetry in the electron and muon decay channels at $\sqrt{s}$ =7 TeV. Methodology, E_T^{miss}, Theoretical Uncertainties and Final Results. ATLAS-COM-PHYS-2010-477.

[5] Search for new phenomena in monojet plus missing transverse momentum final states using 1 fb^{-1} of pp collisions at $\sqrt{s}$=7 TeV with the ATLAS detector. Technical Report ATLAS-CONF-2011-096, CERN, Geneva, Jul 2011.

[6] E. Abat et al. The ATLAS Transition Radiation Tracker (TRT) proportional drift tube: Design and performance. *JINST*, 3:P02013, 2008.

[7] B.M. Abazov. Search for large extra dimensions in the monojet + missing E_T channel at D0. *Phys. Rev. Lett.*, 90:251802, 2003.

[8] I. Antoniadis. A Possible new dimension at a few TeV. *Phys. Lett.*, B246:377–384, 1990.

[9] T. Appelquist, H. Cheng, and B. Dobrescu. Bounds on universal extra dimensions. *Phys. Rev.*, D64:035002, 2001.

[10] N. Arkani-Hamed, Y. Grossman, and M. Schmaltz. Split fermions in extra dimensions and exponentially small cross-sections at future colliders. *Phys. Rev.*, D61:115004, 2000.

[11] N. Arkani-Hamed and M. Schmaltzn. Hierarchies without symmetries from extra dimensions. *Phys. Rev.*, D61:033005, 2000.

[12] A. R. Baden. Jets and kinematics in hadronic collisions. *Int. J. Mod. Phys.*, A13:1817–1845, 1998.

[13] O. Brüning and P. Collier. Building a Behemoth. *Nature*, 448, 2007.

[14] G. Cacciapaglia, C. Csaki, C. Grojean, and J. Terning. Curing the Ills of Higgsless models: The S parameter and unitarity. *Phys. Rev.*, D71:035015, 2005.

[15] L Carminati, M Delmastro, M Hance, M Jimenez Belenguer, R Ishmukhametov, Z Liang, G Marchiori, V Perez Reale, D Malinsky, M Tripiana, and G Unal. Reconstruction and identification efficiency of inclusive isolated photons. Technical Report ATL-PHYS-INT-2011-014, CERN, Geneva, Mar 2011.

[16] Jean-Luc Caron. The LHC injection complex.. l'ensemble d'injection du LHC. AC Collection. Legacy of AC. Pictures from 1992 to 2002., May 1993.

[17] Diego Casadei. Statistical methods used in ATLAS for exclusion and discovery. 2011.

[18] J. Chen. Search for minimum universal extra dimensions with four leptons final state at CMS. *AIP Conf. Proc.*, 1200:579–582, 2010.

[19] H. Cheng. 2009 TASI Lecture – Introduction to Extra Dimensions. arXiv:2010.1003.1162, 2010.

[20] H. Cheng, K. Matchev, and M. Schmaltz. Bosonic supersymmetry? Getting fooled at the CERN LHC. *Phys. Rev.*, D66:056006, 2002.

[21] H. Cheng, K. Matchev, and M. Schmaltzn. Radiative corrections to Kaluza-Klein masses. *Phys.Rev.*, D66:036005, 2002.

[22] K. Cheung and G. Landsberg. Kaluza-Klein states of the standard model gauge bosons: constraints from high energy experiments. *Phys.Rev.*, D65:076003, 2002. Initial stage of work performed at UC, Davis.

[23] R. Chivukula, D. Dicus, and H. He. Unitarity of compactified five-dimensional Yang-Mills theory. *Phys.Lett.*, B525:175–182, 2002.

[24] Glen Cowan, Kyle Cranmer, Eilam Gross, and Ofer Vitells. Asymptotic formulae for likelihood-based tests of new physics. *Eur. Phys. J.*, C71:1554, 2011.

[25] K. R. Dienes, E. Dudas, and T. Gherghetta. Grand unification at intermediate mass scales through extra dimensions. *Nucl. Phys.*, B537:47–108, 1999.

[26] M. El Kacimi, D. Goujdami, H. Przysieniak, and P. Skands. One Universal Extra Dimension in Pythia. *Comput. Phys. Commun.*, 181:122–127, 2010.

[27] A. Abulencia et. al. Search for large extra dimensions in the production of jets and missing transverse energy in p anti-p collisions at $\sqrt{s} = 1.96$-TeV. *Phys. Rev. Lett.*, 97:171802, 2006.

[28] A. Alves et al. The LHCb Detector at the LHC. *JINST*, 3:S08005, 2008.

[29] A. Artamonov et al. The ATLAS forward calorimeters. *JINST*, 3:P02010, 2008.

[30] A. Martin et al. Physical gluons and high E_T) jets. *Phys.Lett.*, B604:61–68, 2004.

[31] G. Aad et al. Search for Diphoton Events with Large Missing Transverse Energy with 36 pb^{-1} of 7 TeV Proton-Proton Collision Data with the ATLAS Detector. *Eur.Phys.J.C*, 71:1744, 2011.

[32] G. Aad et al. The ATLAS Experiment at the CERN Large Hadron Collider. *JINST*, 3:S08003, 2008.

[33] G. Aad et al. Expected Performance of the ATLAS Experiment - Detector, Trigger and Physics. 2009.

[34] G. Aad et al. Measurement of the inclusive isolated prompt photon cross section in pp collisions at $\sqrt{s} = 7$ TeV with the ATLAS detector. oai:cds.cern.ch:1318459. *Phys. Rev. D*, 83(arXiv:1012.4389. CERN-PH-EP-2010-068):052005. 33 p, Dec 2010. Comments: 19 pages plus author list (33 pages total), 10 figures, 5 tables, submitted to Phys. Rev. D.

[35] G. Aad et al. Search for Diphoton Events with Large Missing Transverse Energy in 7 TeV Proton-Proton Collisions with the ATLAS Detector. arXiv:1111.4116, 2011.

[36] G. Aad et al. Search for Diphoton Events with Large Missing Transverse Momentum in 1 fb^{-1} of 7 TeV Proton-Proton Collision Data with the ATLAS Detector. *Phys. Rev. Lett*, 105:221802, 2011.

[37] G. Aad et al. Observation of a new particle in the search for the Standard Model Higgs boson with the ATLAS detector at the LHC. arXiv:1207.7214v1, 2012.

[38] G. Anelli et al. The TOTEM experiment at the CERN Large Hadron Collider. *JINST*, 3:S08007, 2008.

[39] H. Abreu et al. Expected Photon Performance in the ATLAS Experiment. ATLAS-PHYS-INT-2010-137.

[40] H. Abreu et al. Performance of the Missing Transverse Energy Reconstruction and Calibration in Proton-Proton Collisions at a Center-of-Mass Energy of $\sqrt{s} = 7$ TeV with the ATLAS detector. ATLAS-CONF-2010-057.

[41] H. Abreu et al. Performance of the Missing Transverse Energy Reconstruction in Minimum Bias Collisions at Center-of-Mass Energy of $\sqrt{s} = 7$ TeV with the ATLAS detector. ATLAS-CONF-2010-039.

[42] H. Abreu et al. Properties of Jets and Inputs to Jet Reconstruction and Calibration with the ATLAS Detector Using Proton-Proton Collisions at $\sqrt{s} = 7$ TeV. ATLAS-CONF-2010-053.

[43] I. Bertram et al. A recipe for the construction of confidence limits. (FERMILAB-TM-2014), 2000.

[44] K. Aamodt et al. The ALICE experiment at the CERN LHC. *JINST*, 3:S08002, 2008.

[45] K. Nakamura et al. Review of particle physics. *J. Phys.*, G37:075021, 2010.

[46] M. Aharrouche et al. Expected Electron Performance in the ATLAS Experiment. ATLAS-PHYS-INT-2010-126.

[47] M. Mangano et al. Alpgen, a generator for hard multiparton processes in hadronic collisions. *JHEP*, 07:001, 2003.

[48] O. Adriani et al. The LHCf detector at the CERN Large Hadron Collider. *JINST*, 3:S08006, 2008.

[49] P. Aurenche et al. A new critical study of photon production in hadronic collisions. *Phys.Rev.*, D73:094007, 2006.

[50] P. Nadolsky et al. Implications of CTEQ global analysis for collider observables. *Phys.Rev.*, D78:013004, 2008.

[51] R. Adolphi et al. The CMS Experiment at the CERN LHC. *JINST*, 3:S08004, 2008.

[52] S. Agostinelli et al. GEANT4: A Simulation toolkit. *Nucl.Instrum.Meth.*, A506:250–303, 2003.

[53] V.M. Abazov et al. Search for diphoton events with large missing transverse energy in 6.3 fb^{-1} of $p\bar{p}$ collisions at $\sqrt{s} = 1.96$ TeV. *Phys. Rev. Lett.*, 105:221802, 2010.

[54] W. Lampl et al. Calorimeter Clustering Algorithms : Description and Expected Performance. ATLAS-LARG-PUB-2008-002.

[55] X. Anduaga et al. Search for a two photon + ETmiss final state in $\sqrt{s}$ =7 TeV pp collisions at the LHC using the ATLAS detector in the context of the One Universal Extra Dimension model with gravity mediated decays. ATLAS-COM-PHYS-2010-053.

[56] M. Benedikt et al. (eds.). LHC Design Report V.3: The LHC Injector Chain. CERN-2004-003-V-3.

[57] O.S. Brüning et al. (eds.). LHC Design Report V.1: The LHC Main Ring. CERN-2004-003-V-1.

[58] O.S. Brüning et al. (eds.). LHC Design Report V.2: The LHC Infrastructure and General Services. CERN-2004-003-V-2.

[59] C.W. Fabjan and F. Gianotti. Calorimetry for particle physics. *Rev. Mod. Phys.*, 75:1243–1286, 2003.

[60] S. Frixione and B.R. Webber. Matching NLO QCD computations and parton shower simulations. *JHEP*, 06:029, 2002.

[61] S.L. Glashow. Partial Symmetries of Weak Interactions. *Nucl. Phys.*, 22:579–588, 1961.

[62] The LEP Injector Study Group. LEP Design Report Vol. 1, The LEP Injector Chain. CERN-LEP-TH-83-29.

[63] The LEP Injector Study Group. LEP Design Report Vol. 2, The LEP Main Ring. CERN-LEP-84-01.

[64] J.L. Hewett and M. Spiropulu. Particle physics probes of extra space-time dimensions. *Ann.Rev.Nucl.Part.Sci.*, 52:397–424, 2002.

[65] J.R. Forshaw J.M. Butterworth and M.H. Seymour. Multiparton interactions in photoproduction at HERA. *Z.Phys.*, C72:637–646, 1996.

[66] Theodor Kaluza. On the Problem of Unity in Physics. *Sitzungsber. Preuss. Akad. Wiss. Berlin (Math. Phys.)*, 1921:966–972, 1921.

[67] D.J. Kapner, T.S. Cook, E.G. Adelberger, J.H. Gundlach, and et. al. B.R. Heckel. Tests of the gravitational inverse-square law below the dark-energy length scale. *Phys.Rev.Lett.*, 98:021101, 2007.

[68] O. Klein. Quantum theory and five-dimensional theory of relativity. *Z. Phys.*, 37:895–906, 1926.

[69] Chun Lin. A Search for universal extra dimensions in the multi-lepton channel from proton anti-proton collisions at s**(1/2) = 1.8 TeV. FERMILAB-THESIS-2005-69.

[70] C. Macesanu. The Phenomenology of universal extra dimensions at hadron colliders. *Int.J.Mod.Phys.*, A21:2259–2296, 2006.

[71] C. Macesanu, C. McMullen, and S. Nandi. Collider implications of models with extra dimensions. 2002.

[72] C. Macesanu, C. McMullen, and S. Nandi. New signal for universal extra dimensions. *Phys. Lett.*, B546:253–260, 2002.

[73] J. Mansour. Search for Universal Extra Dimensions with the D0 Experiment. 2011.

[74] S. Dimopoulos N. Arkani-Hamed and G.R. Dvali. The hierarchy problem and new dimensions at a millimeter. *Phys. Lett.*, B429:263–272, 1998.

[75] Gunnar Nordstrom. On a possible foundation of a theory of matter. 1914.

[76] Gunnar Nordstrom. Uber die moglichkei, das elektromagnetische feld und das gravitationsfeld zu vereinigen. *Physik. Zeitschr*, 15, 1914.

[77] L. Randall and R. Sundrum. A large mass hierarchy from a small extra dimension. *Phys. Rev. Lett.*, 83:3370–3373, 1999.

[78] T.G. Rizzo. Introduction to Extra Dimensions. *AIP Conf. Proc.*, 1256:27–50, 2010.

[79] C.M. Rujoiu. Phenomenology of extra dimensions. UMI-32-38556.

[80] A. De Rujula, A. Donini, M. Gavela, and S. Rigolin. Fat brane phenomena. *Phys. Lett.*, B482:195–204, 2000.

[81] R.Wigmans. *Calorimetry - Energy Measurements in Particle Physics*. Oxford Science Publications, 2000.

[82] A.O. Sushkov, W.J. Kim, D.A.R. Dalvit, and S.K. Lamoreaux. New Experimental Limits on Non-Newtonian Forces in the Micrometer Range. *Phys.Rev.Lett.*, 107:171101, 2011.